Design and Synthesis of a Black Phosphorus-Based Heterojunction Photocatalyst for Hydrogen Generation from Methanolysis of Ammonia Borane

by

Hüseyin Küçükkeçeci

A Dissertation Submitted to the
Graduate School of Sciences and Engineering
in Partial Fulfillment of the Requirements for
the Degree of

Master of Science

in

Materials Science and Engineering

July 21, 2020

Design and Synthesis of a Black Phosphorus-Based Heterojunction Photocatalyst for Hydrogen Generation from Methanolysis of Ammonia Borane

Koç University

Graduate School of Sciences and Engineering

This is to certify that I have examined this copy of a master's thesis by

Hüseyin Küçükkeçeci

and have found that it is complete and satisfactory in all respects,
and that any and all revisions required by the final
examining committee have been made.

Committee Members:

_____

Assoc. Prof. Dr. Önder Metin

_____

Assoc. Prof. Dr. Uğur Ünal

_____

Prof. Dr. İmren Hatay Patır

Date: _____

In the hopes that this work may in some way contribute to science and help someone or something.

Don't Panic.

ABSTRACT

Design and Synthesis of a Black Phosphorus-Based Heterojunction Photocatalyst for Hydrogen Generation from Methanolysis of Ammonia Borane

Hüseyin Küçükkeçeci

Master of Science in Materials Science and Engineering

July 21, 2020

In recent years, various two-dimensional (2D) materials have attracted great attention due to their unique electrical, thermal, and optical properties. Among them, 2D black phosphorus (BP), thermodynamically the most stable member of phosphorus allotropes, has received great attention in the fields of nanoelectronics, optoelectronics and catalysis owing to its advantageous properties such as having a tuneable optical bandgap and metal-devoid structure in addition to its visible light active characteristics with a high charge carrier mobility. However, there are some limitations that hinder the usage of BP in catalysis applications such as the difficulties in its synthesis and handling along with ambient instability. On the other hand, graphitic carbon nitride (g-CN), another emerging 2D semiconductor material, has attracted attention in catalysis because of its desirable properties such as being metal-free and low-cost but it holds certain drawbacks e.g. relatively large optical band gap and rapid recombination of charge carriers. Construction of heterojunctions between different semiconductors and/or metal nanoparticles (NPs) is a promising strategy to overcome the problems associated with the charge recombination and thus to create more efficient photocatalysts. In this thesis, we aimed to develop a novel heterojunction photocatalyst comprising g-CN and BP semiconductors and AgPd alloy NPs and test their catalytic performance in hydrogen generation from the methanolysis of ammonia borane (AB). To do so, bulk BP crystals were synthesized by using a vapor transport method and then exfoliated in a suitable solvent in order to combine it with mesoporous g-CN (mCN) and as-synthesized AgPd alloy NPs, yielding a ternary composite (mCN/BP/AgPd). The yielded ternary nanocomposite was shown to have a suitable heterojunction between semiconductor BP and mCN with appropriate band gap energies and band positions, which greatly contributes to increased photocatalytic activity of AgPd alloy NPs in the methanolysis of AB. The structure of mCN/BP/AgPd nanocomposites was characterized by using advanced analytical tools. Next, they were employed as catalysts in hydrogen generation from the methanolysis of AB under ambient conditions. Different parameters including mCN/BP ratio in the binary nanocomposite, AgPd alloy nanoparticles composition, surface stripping procedures, and light-source were investigated with detailed kinetic studies to find the optimum conditions to boost the photoactivity of mCN/BP/AgPd ternary nanocomposites in the methanolysis of AB. The highest photocatalytic activity with an turnover frequency (TOF) value of 43.7 mol H_2 mol $AgPd^{-1}$ min^{-1} was achieved by using g-CN/BP ratio of 5/1, applying an acetic acid treatment (AT), and Ag_1Pd_1 alloy composition under blue LED irradiation at room temperature. The reusability of the optimized mCN/BP/AgPd/AT ternary nanocomposites was shown with a five-cycle photocatalytic test, with the photocatalyst retaining 70% of its initial activity at the last cycle.

ÖZETÇE

Amonyak Borandan Metanoliz Yöntemiyle Hidrojen Eldesi İçin Siyah Fosfor Bazlı Fotokatalizör Tasarımı ve Sentezi

Hüseyin Küçükkeçeci

Malzeme Bilimi ve Mühendisliği, Yüksek Lisans

21 Temmuz 2020

Yakın geçmişte, çeşitli iki-boyutlu (2B) malzemeler eşsiz elektronik, optik ve termal özelliklerinden dolayı bilimsel çevrelerden yoğun ilgi çekmektedirler. Bunlar arasından, fosfor ailesinin termodinamik olarak en kararlı allotropu 2B siyah fosfor (BP), ayarlanabilir optik bant aralıklı ve metal içermeyen yapısı dolayısıyla, nanoelektronik, optoelektronik ve kataliz alanlarında çalışılmaya başlanmıştır. Bu özelliklerine ek olarak, BP görünür ışık ile uyarılabilen ve yüksek yük taşıyıcısı mobilitesine sahip bir yarı iletkendir. Ancak, BP'nin yaygın kullanımını engelleyen bir takım istenmeyen özellikleri vardır. Bunlar, sentezindeki zorluklar ve oda koşullarındaki kararsızlığı olarak özetlenebilir. Bir başka 2B yarıiletken olan grafitik karbon nitrür (g-CN), metal içermemesi, kolay ve ucuz sentezi sebebi ile çokça çalışılmaya başlayan diğer bir 2B malzeme olmuştur. Fakat g-CN' ün geniş optik bant aralığı ve yük taşıyıcılarının rekombine olma eğilimi özellikler bu malzemenin kullanılabilirliğini düşürmektedir. Farklı yarıiletkenler ve/veya metal nanopartikülleri (NP) arasında heteroeklemler kurmak, yük taşıyıcılarının rekombine olma eğilimini düşürerek, fotokatalizör etkinliğini arttırmak için geçerli bir strateji olarak görünmektedir. Bu tez kapsamında, g-CN, BP ve gümüş-paladyum (AgPd) alaşım nanopartiküllerinin oluşturduğu bir heteroeklem sistemli katalizörün tasarımı ve sentezi gerçekleştirildi. Sentezlenen heteroeklem katalizörün katalitik performansı, görünür bölge ışık aydınlatmasında amonyak boranın (AB) metanolizinden hidrojen salıverilmesinde kullanıldı. Bunun için, BP kristalleri kimyasal buhar taşıma yöntemi ile sentezlenip, uygun bir çözücü içinde tabaklarına ayrıldıktan sonra mezogözenekli karbon nitrür (mCN) malzeme ile birleştirilerek mCN/BP ikili hibrit malzemesi elde edildi. Başka bir yerde daha önceden sentezlenmiş olan AgPd nanopartikülleri daha sonra bu ikili hibrit malzeme üzerine desteklendi ve tezde heteroeklem katalizör olarak kullanılan son malzeme elde edildi (mCN/BP/AgPd). Elde edilen üçlü nanokompozit malzemenin uygun bant aralıkları ve pozisyonları aracılığıyla başarılı bir heteroeklem yapıya sahip olduğu kanıtlandı ve bu kurulan heteroeklemin AgPd alaşım nanopartiküllerinin metanoliz reaksiyonunda aktiveye olumlu etkisi olduğu görüldü. Gelişmiş analitik cihazlar ve yöntemler kullanılarak, sentezlenen malzemelerin yapısal karakterizasyon çalışmaları gerçekleştirildi. Daha sonrasında, sentezlenen malzemeler AB' dan metanoliz aracılığıyla hidrojen eldesi için oda koşullarında, fotokatalizör olarak denendi. mCN/BP kompozitinin ve AgPd alaşım nanopartiküllerinin kompozisyonu, yüzey temizleme işlemleri, ışık kaynakları gibi çeşitli parametreler değiştirilerek detaylı kinetik çalışmalar yürütüldü. En yüksek fotokatalitik aktivite, yüzeyi asetik asit (AT) ile temizlenen mCN/BP/Ag_1Pd_1/AT heteroeklem yapılı katalizör ile mavi ışık altında oda sıcaklığında 43.7 mol H_2 mol $AgPd^{-1}$ dakika^{-1} çevrim frekansı (TOF) değeriyle elde edildi. Katalizörün tekrar kullanılabilirliği, beş çevrim testi ile gösterildi ve son çevrimde mCN/BP/Ag_1Pd_1/AT üçlü nanokompozit fotokatalizörünün, ilk aktivitesinin %70' ini koruduğu görüldü.

AKNOWLEDGEMENTS

I want to express my gratitude to my supervisor Dr. Önder Metin for giving me a chance to work such a research environment that I felt my ideas and suggestions were taken into consideration very strongly. I understand better now what true and hardworking academics do. He set a great example for me with being both an academically successful and respected person in his private life. In this respect, I would like to share one of my unforgettable memories with Dr. Metin. In the beginning of my thesis studies, it was rather difficult for me to come home and start working or studying again after the tiring lab days. When I complained about this issue with Dr. Metin, he said me without any hesitation or uncertainty that "if you want to be successful in your academic life, you need to get used to sleeping less as soon as possible''. He is the architect of this thesis, and I cannot thank him enough for his hard work on me and being a great example both academically and personally. Thank you Hocam.

I need to thank Dr. Sibel Eken Korkut specially, not just because of her incredible contribution to this thesis but also her contribution on me scientifically and personally. We spend lots of time together in the laboratory at the beginning of my studies and her positivity and knowledge made the laboratory work very easy. I just hope that I can come across people like her in future too.

Dr. Orhan Altan taught me so much that I cannot even begin to describe here. Not only advanced chemistry which I was struggling with in the laboratory, but also I learned that a scientist is not just someone who does experiments in a laboratory but also someone intellectual, someone contributes to society and someone who cares about others and other things around herself.

There are some people who made these two years enjoyable for me. I should thank them for their support because sometimes, you know, you get very stressful and need

some friends. I think they are okay; you should not spoil them. Let's start with my buddy Y. Can Ayra and continue alphabetically because no one wants a drama queen; Merve Ercan, Sena Kulaksız, Sultan Çetin. Thank you, you made this mostly easier.

There is another group of people who I was spending more time with them than my actual home, my lab-mates. I cannot write something about everyone because simply it will take too much time which I do not have at this point, and also, I want to print this thesis without declaring bankruptcy. However, Zafer Eroğlu, I wish we had met earlier, that would be so cool. I believe, you will be someone that I will be proud to be friends with in very near future. Merve Aksoy, thank you for guidance from the very beginning. I don't think things would end up like this without you. Dr. Erbay Kalay, thank you for your never-ending positivity at the lab. You showed us it is possible to work all day with a smile on your face. For the names that I couldn't write here, it was nice to have good people in laboratory and I am very lucky to meet you all.

Hüseyin Tosun should get some credit for being a great flatmate.

Elvin Altıntaş, thank you for being awesome.

Lastly, they made this possible. I would like to thank my family for their unconditional love and support. Gülten Küçükkeçeci, Mithat Küçükkeçeci and Burcu Küçükkeçeci. Thank you for being my family. And thank you for supporting every decision that I make.

TABLE OF CONTENTS

LIST OF TABLES

LIST OF FIGURES

ABBREVIATIONS

AB	Ammonia Borane
AgPd	Silver – Palladium
BP	Black Phosphorus
FT- IR	Fourier Transformation Infrared Spectroscopy
g-CN	Graphitic Carbon Nitride
HR-TEM	High Resolution - Transmission Electron Microscopy
mCN	Mesoporous Graphitic Carbon Nitride
OAc	Oleic Acid
OAm	Oleylamine
ODE	Octadecene
PL	Photoluminescence
SEM	Scanning Electron Microscopy
TEM	Transmission Electron Microscopy
TOF	Turnover Frequency
TMNPs	Transition metal nanoparticles
XRD	X-Ray Diffraction

Chapter 1:
INTRODUCTION

1.1 Hydrogen energy and economy

With the exponential growth of world population and inevitable industrialization, society is facing catastrophic environmental problems related to its surging energy needs [1]. This energy needs can be met by only an efficient, sustainable, and green energy source. Hydrogen is considered as one of the best candidates for a sustainable and green energy carrier, and thus it is being extensively studied by many scientists and researchers [2]. Owing to the great efforts in the field, the use of hydrogen as an energy carrier in daily life has already started. For example, hydrogen powered buses were planned to be deployed in the city of Groningen in Netherlands within the year 2020. Boeing and German Aerospace Centre have already developed hydrogen powered passenger aircrafts. Pictures of these transportation units can be seen in Figure 1.1.

Figure 1.1: Hydrogen powered bus (Ballard Power Systems, Qbuzz) and passenger aircraft (HY4, DLR)

The energy released from the combustion of hydrogen per mass is three times larger than that of a conventional liquid fuel, and when it burns with oxygen the combustion product is only water as opposed to fossil fuels of which the combustion results with the emission of harmful gases including CO_2, CO and NO_x etc. [3]. Hydrogen is environmentally friendly and does not cause any carbon emission. Additionally, hydrogen is a strong reducing agent and thus it is an important reagent in chemical industry as well. An economy system based on usage of hydrogen energy is offered and named as hydrogen economy. Hydrogen economy term, in general includes research and

applications of hydrogen-based energy systems in ever day systems. This term can be explained further as development of more efficient hydrogen production systems from different sources, safe storage, and controllable release procedures in order to effectively utilize hydrogen and lastly advancement of fuel cells which use hydrogen as a primary fuel. However, there are certain limitations that hinder the widely usage of hydrogen. The storage of hydrogen and its release from a safe source are deemed to be the main problems in hydrogen-based economy [4]. This topic is being studied largely to come up with a solution that is going to enable usage and storage of hydrogen safely and efficiently. Hydrogen can be stored physically (high-pressure gas phase or liquid phase) or chemically (chemical hydrides).

The storage of hydrogen in a chemical compound, namely chemical hydrogen storage in which the hydrogen is covalently bonded to another atom, is one of the most effective ways of storing and releasing of hydrogen efficiently when it is needed because physical storage of hydrogen in its gas or liquid phase constitutes certain dangers and it is not possible to utilize hydrogen in portable systems with this form. Moreover, boron, being a light element and having stable hydrides at ambient conditions, is widely used for chemical hydrogen storage purposes. A list of boron hydrogen compounds that can be used as a hydrogen source can be seen in Table1.1. Considering that Turkey holds 72% share of world boron deposits, utilization of boron in hydrogen economy is desired in Turkey in both academic and industrial applications [5].

Table 1.1. shows all possible boron-based hydrogen storage materials. As it can be concluded from Table 1.1, ammonia borane (AB) is one of the most promising materials for boron-based chemical hydrogen storage for the portable systems [6]. AB is a non-toxic chemical with a high hydrogen content (19.6% by weight) and high stability under ambient conditions [7]. AB is a simple adduct that is formed between BH_3 which acts as a Lewis acid (electron pair acceptor) and NH_3 which acts as a Lewis base (electron pair donor). In the compound, three hydrogen atoms in the hydride form are covalently bounded to each boron and nitrogen, separately. The molecular structure of AB can be seen in Figure 1.2.

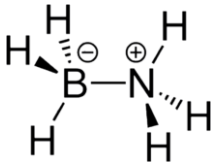

Figure 1.2: Molecular structure of Ammonia Borane.

Table 1.1: Comparison of boron hydrogen compounds that can be used as a hydrogen storage medium.

Compound Name	Structure	Molecular Weight (g/mol)	Hydrogen Content (weight %)
Ammonia borane		30.87	19.6
Sodium cyanoborohydride	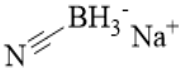	62.84	4.8
Dimethylamine borane	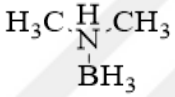	58.92	17.1
Trimethylamine borane	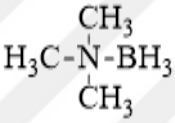	72.95	16.6
Triethylamine borane	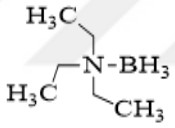	115.02	15.8
tert-butylamine borane	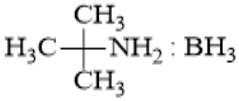	86.97	16.2
Morpholine borane	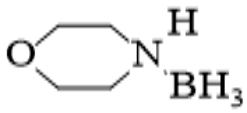	100.96	12
Borane pyridine	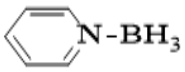	92.93	8.8

The hydrogen stored in AB complex can be generated by three ways, namely thermolysis, dehydrogenation and solvolysis. Among these methods, solvolysis is the most efficient, safest, and controllable method with taking advantage of high solubility of AB in most of polar solvents such as short-chain alcohols and water. However, a suitable catalyst is needed to release hydrogen via solvolysis of AB. For example, in the

presence of a suitable catalyst, 1 mole of AB releases 3 moles of hydrogen in water (hydrolysis) or methanol according to the reaction equations given below (Eq.(1.1) and (1.2)).

$$NH_3BH_3 + 2H_2O \rightarrow NH_4BO_2 + 3H_{2(g)} \quad (1.1)$$

$$NH_3BH_3 + 4CH_3OH \rightarrow NH_4B(OCH_3)_4 + 3H_{2(g)} \quad (1.2)$$

Methanolysis of AB holds some advantages over AB hydrolysis. For instance, the recycling of ammonium metaborate (NH_4BO_2), which is the side product of AB hydrolysis, into AB is a challenge task requiring high hydrogen pressure and temperature [8]. On the other hand, methanolysis side product $NH_4B(OCH_3)_4$ can be converted back to AB at room temperature [9]. Additionally, it was shown that the reaction of methanolysis can be initiated even below 0 °C, which is a very advantageous property for mobile applications [10].

1.2 Heterogenous photocatalysis

In the simplest form, a catalyst is a substance that increases the rate of the reaction. Catalysts are not altered during reaction and they exit the reaction as they entered. Reaction rate is increased by offering a new reaction pathway with a lower activation energy (E_a) (Figure 1.3).

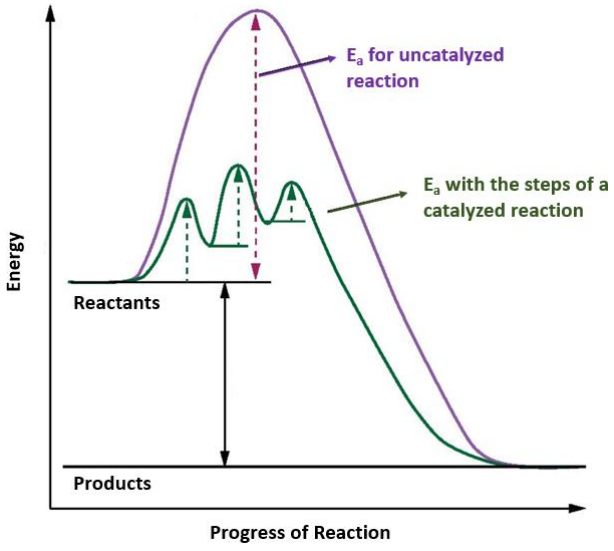

Figure 1.3: Change in the activation energy results with increased rate in the presence of a catalyst.

Catalysts can be classified as homogenous catalysts, heterogeneous catalysts, and biocatalysts. A detailed comparison of catalyst types can be seen in Table 1.2. Homogenous catalysts show strong disadvantages when their separation and thermal stability is considered. Since the reagents and the catalyst are in the same phase, often it is very hard to separate the catalyst, and there is need for a special step for the product and catalyst separation. Biocatalysts are used in living systems to conduct chemical reactions, so they are out of scope for most of the catalytic applications and their use and research are very limited. On the other hand, heterogenous catalysts are mostly preferred in industrial applications because of their high stability and reusability. They can be used in many cycles and they can be simply washed away, and product can be isolated at the end of the reactions. There is no need for any special treatment in order to separate the product. They are widely used in both industrial and academic applications.

Table 1.2: Homogenous catalysts, heterogeneous catalyst, and biocatalyst comparison.

	Homogenous catalysts	**Heterogeneous catalysts**	**Biocatalyst**
Phase	Liquid/Gas	Solid	Solid/Liquid
Selectivity	High	Low	High
Activity	High	Low	High
Product Separation	Difficult	Easy	Easy
Catalyst Regeneration	Difficult	Easy	Optional
Cost	Low	High	High

Even though, heterogeneous catalysts stand out among others, there is still room for improvement in catalysis field. In this respect, a new class of catalysts, heterogenous

photocatalysts, is a new era of catalysts that employ semiconductors and light in order to carry catalytic reactions. The rising potential of this type of catalysts has been shown in recent years by many research and publications in this field.

Procedure of the usage of sun light as a clean energy source to drive chemical reactions is called photocatalysis. A photocatalytic process requires an interaction between light and a semiconductor material so it can be excited by this light. Semiconductors absorb photons having equal or greater energy than their band gap [11]. Band gap defines the minimum energy needed for the generation of photo induced electron – hole pairs. After absorbing light which has larger energy than the band gap of the semiconductor, an electron gets excited and jumps from valance band to conduction band of the semiconductor. At the same time, a positively charged hole is created in the valence band because of absence of electron. After generation of electron – hole pairs, electrons at the conduction band can be used for reduction of species and at the same time, holes at the valance band can be used for oxidation. Band gap values and conduction – valance band positions for some semiconductors can be seen in Figure 1.4. The selection and usage of an appropriate semiconductor in photocatalysis is a crucial task and search for a suitable semiconductor continues to this day.

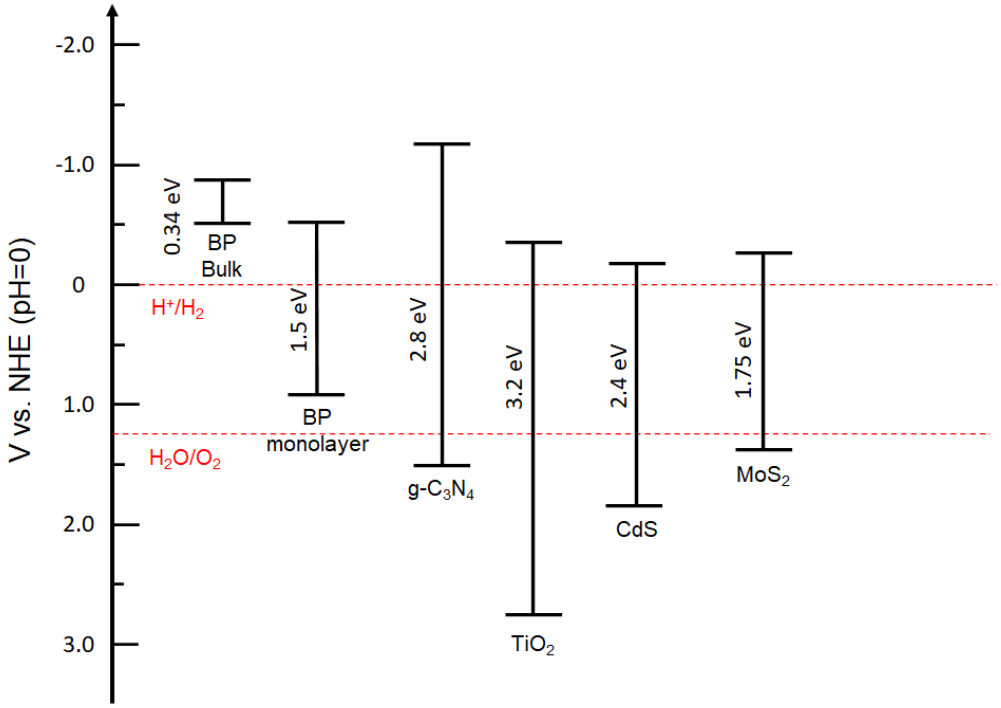

Figure 1.4: Band gap values and valance – conduction band positions of semiconductors; BP, g-CN, TiO_2, CdS and MoS_2.

Photocatalysis idea was first proposed by Fujishima and Honda in 1972 [12]. In this study, a very well-known and common titanium dioxide (TiO_2) semiconductor was used as an anode electrode and following light irradiation with an appropriate light source that exceeds the band gap energy of semiconducting TiO_2, photolysis of water was conducted in an electrochemical cell. A photolysis reaction mechanism was offered as given below. This study showed the great potential of semiconductor heterogenous photocatalysis firstly in hydrogen evolution from water.

$$TiO_2 + 2hv \rightarrow 2e^- + 2p^+$$

(excitation of TiO_2 by light)

$$2p^+ + H_2O \rightarrow \frac{1}{2}O_2 + 2H^+$$

(water oxidation at the TiO_2 electrode)

$$2e^- + 2H^+ \rightarrow H_2$$

(hydrogen reduction at the platinum electrode)

The overall reaction is:

$$H_2O + 2hv \rightarrow \frac{1}{2}O_2 + H_2$$

To this day, research in heterogenous photocatalyst is growing with strong interest because of their reusability, high efficiency and finally their ability to absorb and utilize UV and visible light [13]. Heterogeneous photocatalytic processes can be explained by following steps (Figure 1.5):

I. Absorption of incident light by a semiconductor and creation of electron-hole pairs,
II. Arrival of created electron and hole pair to the semiconductor surface,
III. Adsorption of reactants to the surface of catalyst,
IV. Formation of products at the catalyst surface by redox (reduction and oxidation) reactions,
V. Desorption of the products from the catalyst surface.

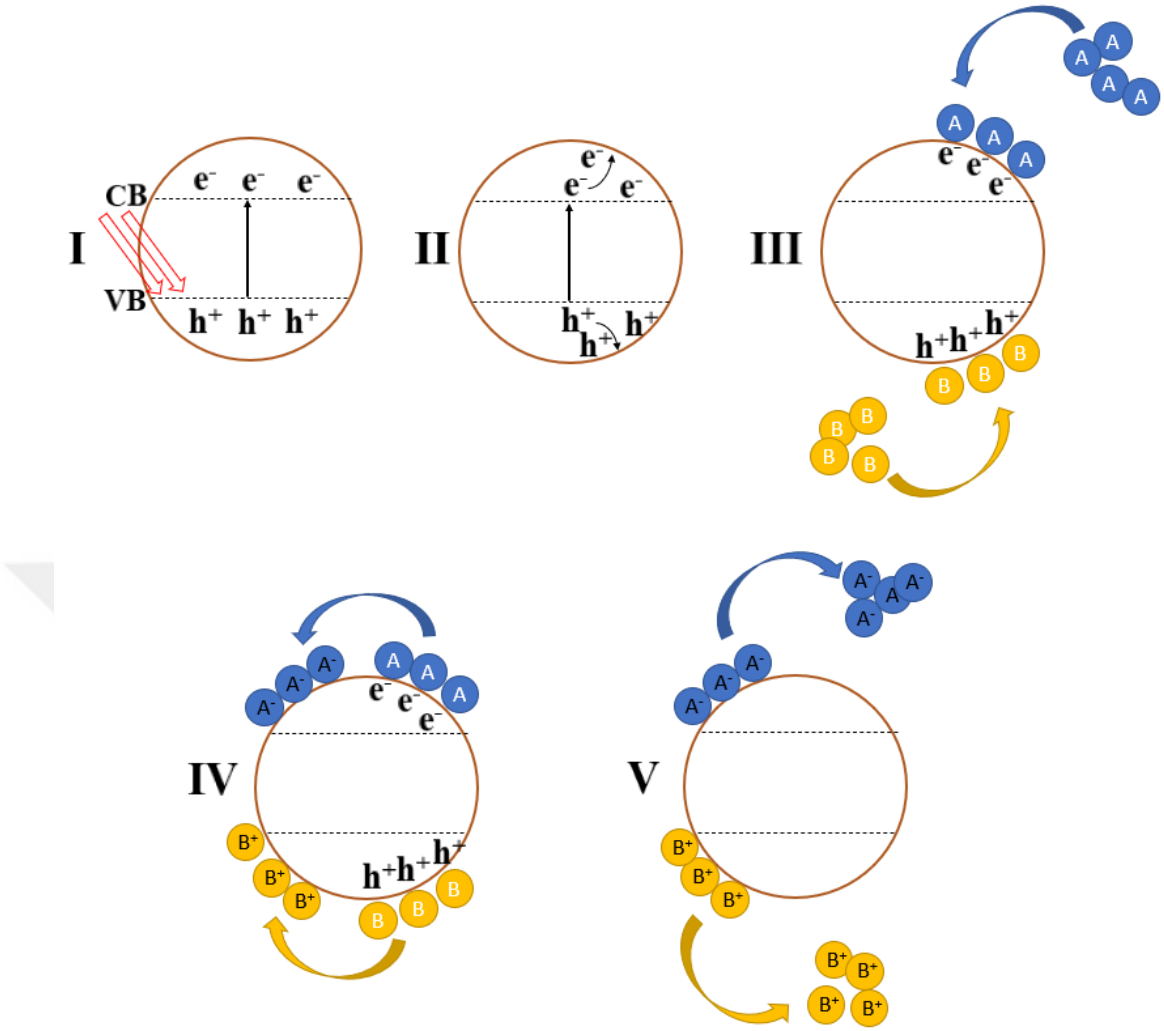

Figure 1.5:Heterogenous photocatalytic process steps (e^- and h^+ represent electrons and holes, respectively).

Using this knowledge, current efforts are being made to maximize the efficiency of these processes, mainly by increasing the absorption ability of semiconductor to use sunlight effectively and preventing recombination of created electrons and holes. The most crucial requirement is the absorption of sunlight which constitutes visible and IR light as the higher portion (95% total) compared to UV light (only 5%) [14], [15]. Traditional photocatalyst semiconductors such as TiO_2 face this problem [13]. It is a non-toxic and stable material but its inherent band gap which is too large for absorption of visible light limits its utilization effectively [16–18].

Compared to the traditional photocatalysts, a new class of materials, namely two-dimensional (2D) semiconductor materials are attracting great attention from researchers

because they offer unique properties additional to their high efficiencies in conversion and better light absorption behaviour than their traditional counterparts.

1.3 2D semiconductor materials

A new era of materials has started with the revolutionary work of Novoselov [19]. It was already known that some of the materials (e.g. graphite) are composed of puckered layers (e.g. graphene) which are bounded by weak Wan der Waals forces holding these layers together [20]. However, there was no attempt on the isolation of these layers until 2004. The first study on the isolation of 2D graphene was done by Novoselov and Geim who received the Nobel Prize in Physics in 2010 [19]. They showed that when these layers are isolated, they start to behave differently from their bulk form and show very unique optical and electronic properties [21]. The main reason behind these unique properties can be explained by the restricted electron movement which is confined to only two dimensions rather than three. Following this revolutionary work, 2D materials research has gained upmost importance and lots of new materials have discovered such as boron nitride (BN), molybdenum disulphide (MoS_2) and tungsten diselenide (WSe_2). Some examples and their representative structure can be seen in Figure 1.6. Among these 2D materials, there are conductors (i.e. graphene) which are mostly not possible to utilize them in photocatalysis and semiconductors (i.e. BN) which are ready to be used in photocatalysis. There are some semiconductor 2D materials showed great potential to be used in photocatalytic applications and reported in literature.

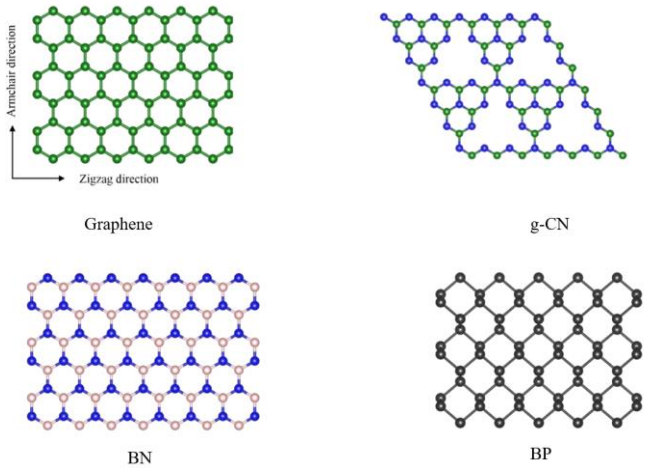

Figure 1.6: Several examples of 2D materials with their unique layered structures (graphene, graphitic carbon nitride, boron nitride and black phosphorus, respectively) [22].

1.4 Heterojunction photocatalysis

Photocatalysis has started to being studied by researchers all around the world as a potential solution to energy problems of the today's world. Historically, the most studied photocatalysts are metal oxides with the most famous one TiO_2. In addition to these traditional photocatalysts, there are many new groups of materials as photocatalyst candidate such as transition metal dichalcogenides, covalent organic frameworks and 2D materials. Other than finding and employing new photocatalysts, different strategies are being employed to improve photocatalytic properties of these materials such as doping, surface functionalization and heterojunction creation with another semiconductors or metals. Among these strategies, forming heterojunctions has attracted great attention because of its high potential in increasing the photocatalytic efficiency. In a very fundamental approach, creating heterojunctions lets one get rid of certain problems of the individual components and take full advantage of them while created heterojunction itself is advantageous for photocatalysis. Overall, there are four categories of heterojunctions in semiconductor photocatalysis presented in literature. These categories are heterojunctions between semiconductors and semiconductors; semiconductors and metals; semiconductors and conductors; and finally, many component systems. In the scope of the current thesis, heterojunctions between semiconductors and semiconductors and between semiconductors and metals are going to be evaluated. Possible heterojunctions between semiconductors and semiconductors are type I, type II and type III junctions (Figure 1.7). In type I heterojunction, photoinduced electrons and holes of one semiconductor flow through the second semiconductor because of the lower energy of valance and conduction bands of the second semiconductor. These new charge carriers coming from the first semiconductor, together with second semiconductor's charge carriers, are spent in the reaction here. In type II heterojunctions, electrons, and holes from participating semiconductors flow to the valance and conduction band of different semiconductors. Therefore, excited electrons are gathered in one semiconductor and holes are gathered in another. Finally, in type III heterojunction, valance and conduction band positions of semiconductors do not coincide and as a result each semiconductor holds its charge carriers thus no flow occurs. Each type of heterojunction is unique and there is not an optimum heterojunction for all reactions. Each specific reaction should be assessed individually, and suitable heterojunction(s) should be determined specially for that

reaction. In this work, a type I semiconductor heterojunction was formed, and its performance were evaluated in detail.

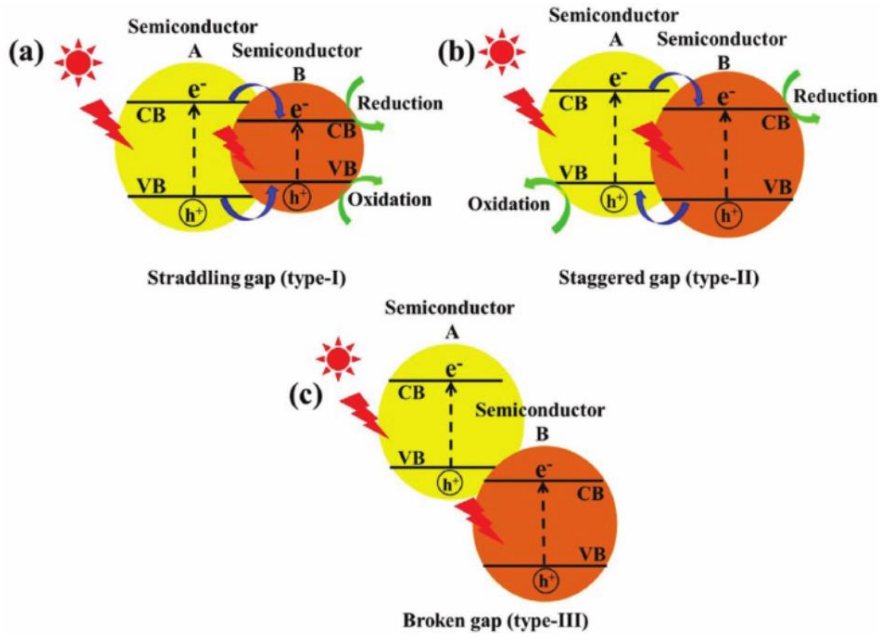

Figure 1.7: Schematic illustration of the three different types of semiconductor - semiconductor heterojunctions in photocatalysts: (a) type-I, (b) type-II, and (c) type-III heterojunctions [23]. (CB defines the conduction band and VB defines the valance band)

When a semiconductor metal heterojunction is formed, it results in the formation of Schottky barrier. Working principle of Schottky barrier can be seen in Figure 1.8. A Schottky barrier which can be formed between metal and semiconductors, fundamentally restricts the backflow of excited electrons which results in an enhanced photocatalytic activity. Formed Schottky barrier inhibits the return of electrons from metal to semiconductor thus metals act as an electron reservoir and these electrons are readily used in the reaction.

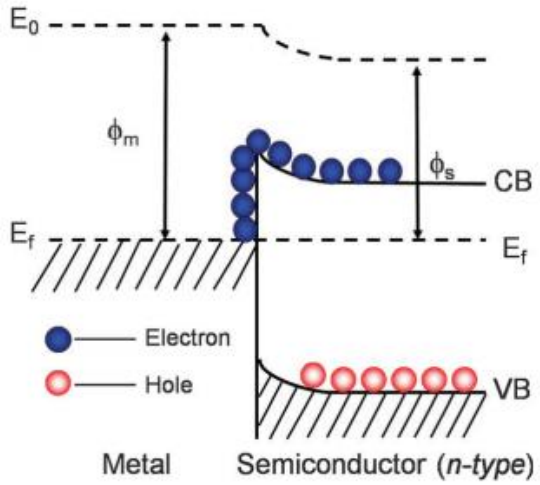

Figure 1.8: Representation of Schottky Junction formed between a metal and semiconductor surface [24].

1.5 Graphitic carbon nitride

Graphitic carbon nitride (g-CN) is a well-studied, non-toxic, metal-free and earth-abundant two dimensional semiconductor which has ability to absorb visible light owing to its suitable band gap (~2.8 eV) [25]. It is an n-type semiconductor material with an indirect band gap. Representative picture of g-CN showing its distinctive yellow colour and band positions with respect to normal hydrogen electrode can be seen in Figure 1.9.

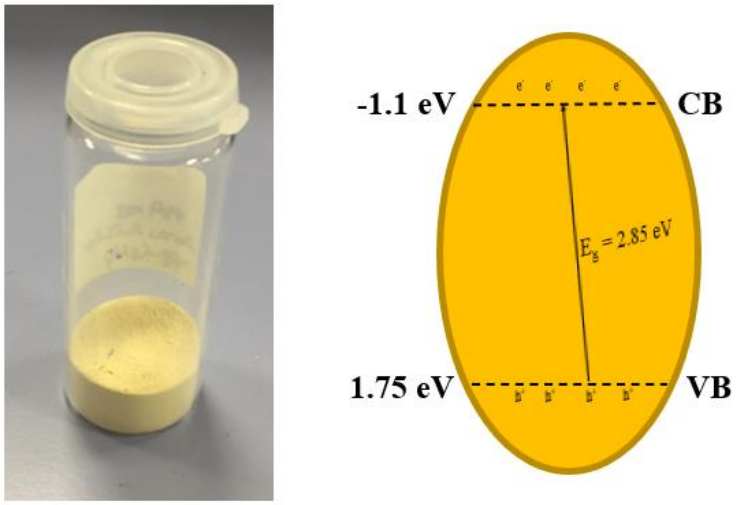

Figure 1.9 Representative picture and band positions of g-CN.

However, the pristine g-CN suffers from certain drawbacks such as photoexcited charge recombination, low visible light utilization and low surface area, which lead to reduced photocatalytic activity [26]. The surface area of g-CN can be enlarged by using different synthesis methods to prepare mesoporous graphitic carbon nitride (mCN). Other drawbacks of g-CN can be eliminated by forming composites of g-CN with suitable semiconductors. Some of these properties that affect its catalytic activity can be seen in Figure 1.10. In this respect, several studies have clearly showed the enhanced photocatalytic activity of g-CN by preparing its composites [27], [28].

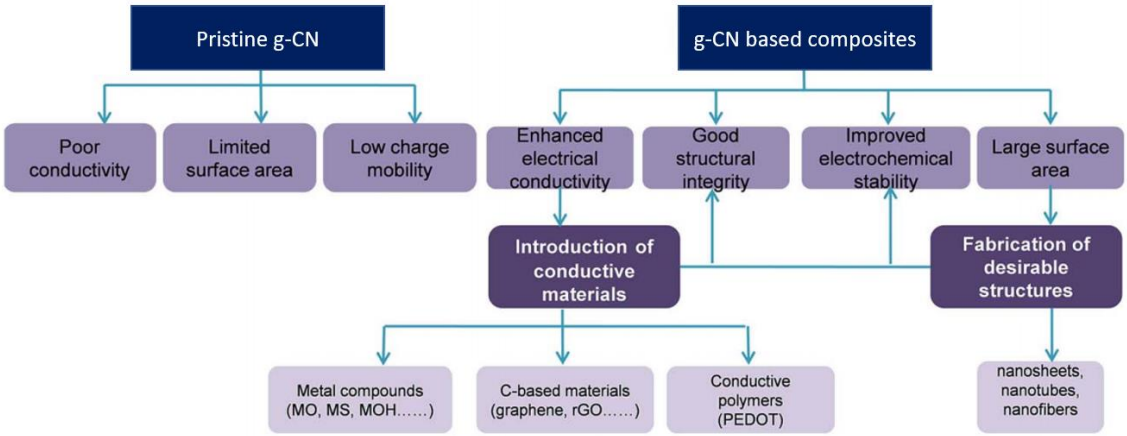

Figure 1.10: g-CN and g-CN based composites with some factors that affect its catalytic properties [29].

1.6 Black phosphorus

Black phosphorus (BP) is a semiconductor material which has unique thickness tuneable direct bandgap (from 0.3 eV to 2.0 eV), wide-range light absorption ability, high charge mobility, large specific surface area and high thermal stability [30], [31]. BP is thermodynamically the most stable allotrope of the phosphorus element. It should be noted that phosphorus is one of the earth abundant elements. These properties make BP a highly promising material for applications in catalysis, especially photocatalysis [32]. Even though the first synthesis of BP dates back to 1914, its utilization in catalysis is a newly emerging area [33]. Crystal structure of BP with frontal and top view and lattice parameters can be seen in Figure 1.11.

BP can crystallize in cubic, rhombohedral or orthorhombic structures or can be amorphous [34]. Highly anisotropic structure orthorhombic crystalline BP with intralayer

strong primary bonding of P and interlayer weak secondary bonding results with unique properties.

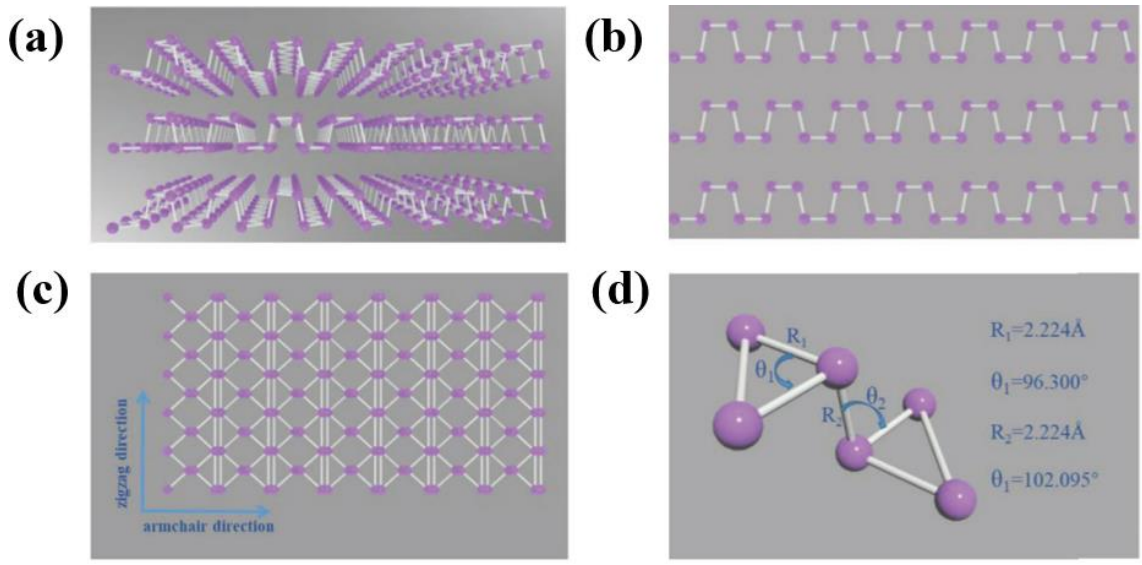

Figure 1.11: (a) The crystal structure of layered BP, (b) the front view of layered BP, (c) the vertical view of layered BP, and (d) the detailed lattice parameters of layered BP [35].

However, until the discovery of the low-pressure route for the synthesis of BP crystals in 2007 [36], the utilization of BP in various research fields was limited because it had been synthesized using a high-temperature and high-pressure method [33]. Following this revolution in BP synthesis, many publications have emerged on the photocatalytic applications of BP [37]. Increase in the number of publications regarding usage of BP in literature can be seen in Figure 1.12. However, it is indicated that pristine BP suffers from instability under ambient conditions, which remains an obstacle for the photocatalytic applications of BP [38], [39]. In order to overcome these stability issues and increase photocatalytic activity of BP, various hybrids of BP with another semiconductor have been designed including BP/Tungsten Disulfide (WS_2) [40], BP/Graphene [41], BP/Red Phosphorus [42] and BP/Graphitic Carbon Nitride [43].

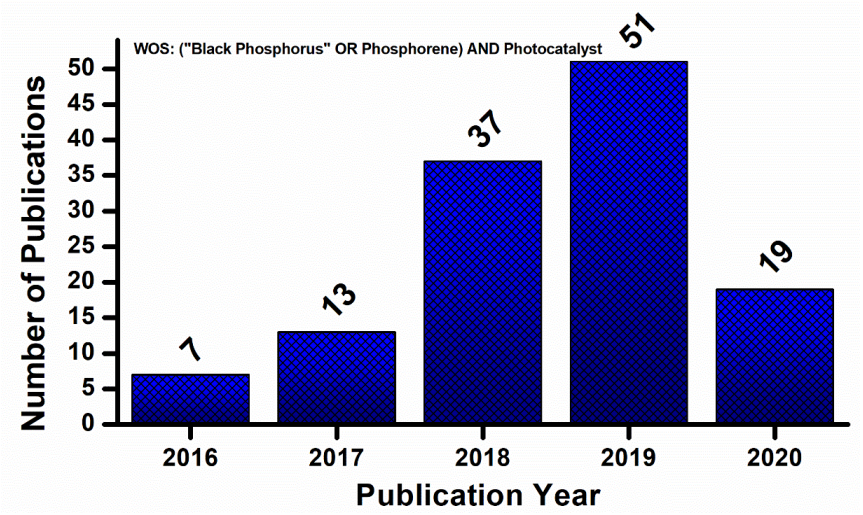

Figure 1.12: Web of Science search results. Inquiry: "Black Phosphorus" or Phosphorene and Photocatalysis.

1.7 Transition metal nanoparticles and support materials

Transition metal nanoparticles (TMNPs) are particles having an average particle size of 1–100 nm and synthesized from the elements whose atoms have a partially filled d sub-shell. They are employed in catalytic applications owing to their numerous advantages over the conventional heterogeneous catalysts. Firstly, TMNPs carry dissimilar and mostly advantageous properties such as surface area, optical and electronical properties, mechanical properties, crystallinity compared to their bulk forms [44]. However, the most important advantage of using TMNPs in catalysis arise from surface atom coverage and it means simply having more surface atoms which are catalytically active phase to take part in the reaction. The relation between surface atom percentage and particle size can be seen in Figure 1.13. For catalytic applications, synthesis of TMNPs should be reproducible. Particle size should be less than 10 nm and

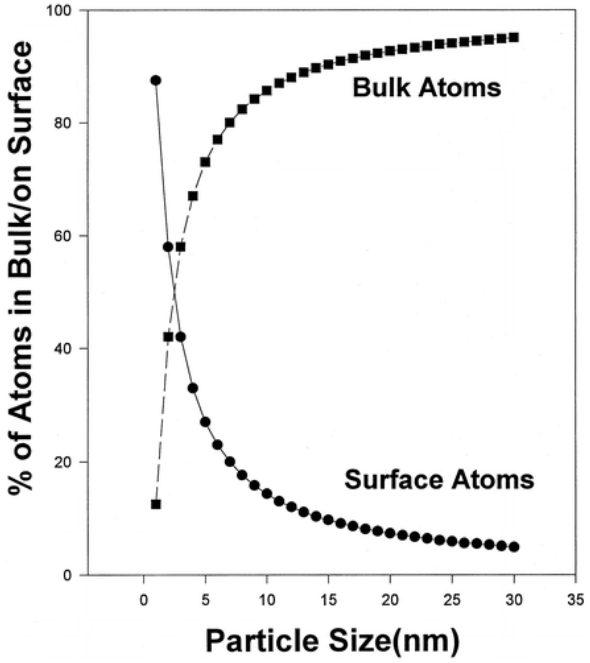

Figure 1.13 Surface and bulk atom percentage as a function of particle size [45] .

particle size deviation should not be more than 15%. Their compositions should be known precisely so that they can be utilized effectively. In the synthesis of TMNPs, physical or chemical methods can be used. Physical methods describe the synthesis of nanoparticles using bulk metal forms (top-down procedures). Mechanical milling can be given as a great example for top-down procedures. In the presence of hydrogen gas, mechanical milling of ingot metals can result with desired metal nanoparticles. However, this method is highly energy intensive and it is hard to gain a precise control over particle size. Chemical methods include reduction and seeded growth of metal cations in a reaction medium (bottom-up procedures). Bottom-up procedures employ wet chemistry methods and a great control over particle size and morphology which is another important factor in TMNPs synthesis can be achieved. During and after the synthesis, nanoparticles tend to come together and minimize their surface area because of their high surface energies. Since the nanoparticles are kinetically not stable, they must be stabilized against agglomeration into the bulk form, and this is another important criterion in the synthesis of TMNPs. The stabilization can be achieved intrinsically when nanoparticles are synthesized in-situ on support materials and support materials can inhibit their movement. In the case of colloidal TMPNs which means that nanoparticles are being stored in an appropriate solvent, there needs to be an external stabilization agent. In colloidal TMNPs,

stabilization can be achieved in two ways, sterically and electrostatically. Usually surfactants which are added to reaction medium, are used to facilitate these stabilizations. Steric stabilization can be explained as the stabilization gained through adsorption of large molecules onto nanoparticle surface and these large molecules apply a repulsive force [46]. Mostly long carbon chain containing bulky compounds (i.e. oleylamine, trioctylphosphine) are being used for this type of stabilization. Electrostatic stabilization is gained through the repulsion of surface adhered anionic species. These anionic species apply a repulsive electrostatic force and colloidal stability is achieved [47]. Salts of organic acids can be used for this purpose. Schematic representation of stabilization types can be seen in Figure 1.14.

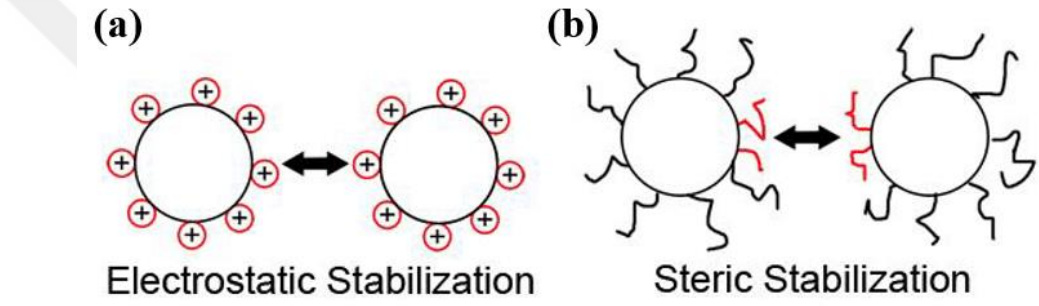

Figure 1.14: Graphical representation of (a) electrostatic and (b) steric stabilization.

In order to utilize TMNPs better in catalytic applications, a synergistic affect between two distinct metals can be used in addition to other advantages such as decreasing the amount of metal that are expensive or toxic. There are different strategies to establish a mixture of the metals that results with varying structures presenting desired outcomes [48]. These structures can be classified as core-sell, phase separated, and alloy (solid solution). Representative structures can be seen in Figure 1.15. It is widely known that alloying is a clever strategy to boost physical, chemical, and mechanical properties of metals in a classical sense and it is frequently employed in macro scales. With the uprising nanotechnology, it was shown that alloying is a concept that can be well adapted into metal nanoparticles as well [49]. Many different alloy nanoparticles with different metal contents were synthesized and the research continues (e.g. Nickel – Cobalt , Nickel – Palladium , Copper – Silver) [50]. These new alloys show unique and superb properties compared to their bare constituents most of the time. In addition, alloying is used frequently to decrease noble metal content in a lot of transition metal catalysts because simply using only noble metals is expensive and noble metals are not easy to access and

they are scarce [51]. In order to establish intermixing of metals, there are some conditions that need to be addressed [52]. These conditions are summarized by Hume–Rothery rules which states metals form alloys if these conditions are met:

- ✓ The atomic ratios of participating metals should not differ more than 10%.
- ✓ The crystal structure of the metals should be similar.
- ✓ Valence number of the metals should be similar.
- ✓ The metals should not have a big difference in electronegativity.

Alloy nanoparticles can be synthesized by using physical and chemical methods. Physical methods include the synthesis of alloy nanoparticles starting from their bulk alloy forms while chemical methods generally employ solution-based metal ion co-reduction methods. In this thesis, a colloidal synthesis method that allows the control of particle size, size distribution and alloy composition was used for the synthesis of AgPd alloy nanoparticles,

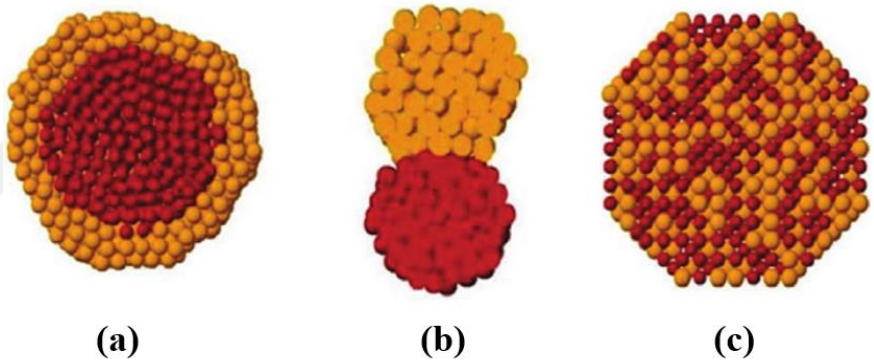

Figure 1.15: (a) Core-shell structure, (b) phase separated structure and (c) alloy structure that two distinct metal can form [53].

Support materials are needed in order to immobilize and stabilize transition metal nanoparticles to use them in heterogenous catalysis applications. Supports might be a simple high surface area material such as carbon. On the other hand, in electrocatalysis and photocatalysis applications that establish a strong electronic and optical interaction between support and nanoparticle, support choice is very important. In this type applications, more advanced support materials such as transition metal oxides or 2D materials can be used. Especially in photocatalysis, semiconducting supports hold an upmost significance because they needed to be excited with appropriate irradiation to run the photocatalytic reaction meanwhile offering a suitable environment for the stabilization of catalytically active sites.

Chapter 2:
LITERATURE REVIEW

2.1 Hydrogen production from AB

When mobile systems are considered, it is seen that there is a need for a safe, portable, and reliable hydrogen carrier [54]. Additionally, this material needs to release its hydrogen with ease whenever its needed. Traditional hydrogen sources fail to satisfy all these conditions. As a solution to this problem, storing hydrogen in chemical compound, called as chemical hydrogen storage was offered. Boron-hydride compounds contain large amount of hydrogen atoms and they can release their hydrogen via solvolysis in the presence of suitable catalyst on demand [55]. Side products are mostly harmless, and, in some cases, these side products can be recycled [9]. Within this scope, AB has started to be used as a chemical storage material because of its hydrogen content by weight (19.6%) and non-toxic side products [56].

In 2006, Xu and Chandra reported for the first time that 3 moles of hydrogen can be released from 1 mole of AB via hydrolysis reaction [57]. This study included usage of noble metal catalyst, but later it was shown that this reaction can be carried out with high efficiency in the presence of non-noble transition metals as well [58], [59]. Starting from these publications, usage of AB as hydrogen source and its catalysis has gained tremendous attention and many different catalysts, mainly employing metal(0) nanoparticles as active sites, were developed and tried in this reaction [59]. Besides the hydrolysis of AB, Ramachandran and Gagare showed that methanolysis of AB in the presence of transition metal salts as catalysts can also be used in hydrogen generation from AB with its advantageous properties [60]. In 2008, it was shown that non-noble transition metals can catalyse methanolysis of AB as well but with a far less catalytic activity [61]. Later, Metin et al. reported that polymer stabilized Palladium(0) (Pd) nanoclusters were shown to be active in the methanolysis reaction [62]. In another study, supported Ruthenium(0) (Ru) and Rhodium(0) (Rh) nanoclusters were employed as catalysts for the methanolysis of AB [63], [64]. Taking the advantage of heterogeneous catalysis, these catalysts were shown to be reusable, but rarity and cost of these noble metals inhibited their practical use. In 2012, it was shown that alloyed nano structure of Cobalt (Co) and Pd has the ability to catalyse the methanolysis reaction with great

efficiency [65]. It was already known that Pd was an active catalyst in this reaction and this study showed that alloying can be used as an effective strategy in order to boost catalytic activity and at the same time reduce the usage of precocious noble metals in the methanolysis of AB. Finally, in 2016, AgPd alloy nanoparticles synthesized by wet chemical method and supported on carbon were shown to be highly active catalyst thus they were selected as active sites in this thesis [66].

The idea of photocatalytic solvolysis of AB is rather new and it is not studied very well. There is only limited amount of publications on the photocatalytic solvolysis of AB. In 2015, two papers were published. First publication reports the usage of semiconducting plasmonic tungsten oxide nanowires that were synthesized by simple solvothermal method [67]. There was a notable activity increase in hydrolysis with five times enhancement. This was a single component system; thus, it did not take advantages offered by heterojunction systems in photocatalysis. Second publication employed a heterojunction photocatalyst. Nanoparticles of Gold (Au) and Co were supported on carbon nitride material and as a consequence Schottky barrier was formed at the interface between semiconducting carbon nitride and conductor Au – Co nanoparticles [68]. This photocatalyst showed activity in the hydrolysis of AB. Lastly, in 2017, photocatalytic hydrolysis of AB was achieved by Ag-based plasmonic photocatalysts. With light irradiation, enhancement in charge transfer was observed at the heterojunction between Silver (Ag) NPs and TiO_2 [69].

Photocatalytic methanolysis of AB was not reported in literature and keeping in mind that methanolysis holds certain advantages over hydrolysis of AB, this topic needed to be addressed. Moreover, this thesis employs a multi component system (semiconductor – semiconductor heterojunction and semiconductor – metal heterojunction at the same time) which was not reported in the photocatalytic solvolysis of AB to this day.

2.2 The synthesis and catalytic applications of monodisperse AgPd alloy nanoparticles

AgPd alloy nanoparticles are reported as highly active catalysts in the solvolysis of AB [70] . They have alloy structure in nanometre scale and composed of silver and palladium in metallic state. Because of their high activity, they are selected as active sites in this study. In general, TMNPs can be synthesized with physical or chemical methods.

Physical methods include the synthesis of nanoparticles starting from their bulk form while chemical methods generally employ solution-based metal ion reduction methods. For this project, in the synthesis of AgPd alloy nanoparticles, a chemical method, colloidal synthesis was used because in this way a great control can be obtained over particle size, size distribution and alloy composition.

First synthesis of AgPd alloy nanoparticles was done by Zhou et al. to be used in catalytic decomposition of formic acid in 2008 [71]. Firstly, some amount of carbon support was dispersed in a mixture of ethanol and water. Then, necessary metal salts are added into this solution and after impregnation, the suspension was reduced by sodium borohydride in aqueous environment. After filtration and cleaning steps, final catalyst was obtained. Average particle size was determined as 8 nm and the catalyst show good activity in hydrogen generation reaction from formic acid.

After this study, in 2013, AgPd alloy nanoparticles were synthesized by using a colloidal approach to use them in again dehydrogenation of formic acid [72]. In addition to metal precursors, octadecene (ODE) was used as a high temperature resistant solvent. Oleylamine (OAm) was used as a surfactant and reducing agent and finally oleic acid was added as a co-surfactant. and the synthesis was conducted in inert conditions and at relatively mild temperatures (453 K). Obtained particle size with this recipe was 2.2 nm which was a remarkable size.

AgPd alloy nanoparticles had started to be used for other catalytic applications such as solvolysis of AB additional to formic acid decomposition. In 2016, it was shown that AgPd alloy nanoparticles are highly active in the methanolysis of AB too [70]. In this study, AgPd alloy nanoparticles were synthesized via colloidal method. Other than metal precursors, only OAm was used as a solvent, surfactant and reducing agent at the same time. Average particle size was succeeded as 6 nm. Reaction was conducted under inert conditions and temperature was raised to 483 K.

2.3 Graphitic carbon nitride

g-CN synthesis dates back to the year 1834, when interconnection of tri-s-triazine units resulted with the formation of a polymer. This structure was named as “melon” later [73]. Synthesis route for g-CN starting from tri-s-triazine units can be seen in Figure 2.1.

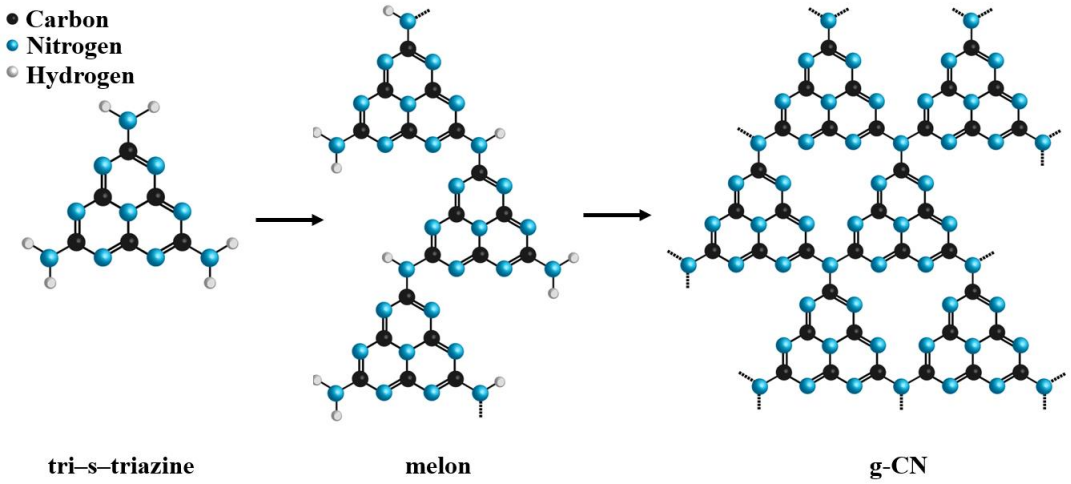

Figure 2.1: Synthesis pathway for g-CN starting from tri-s-triazine units.

In 1989, a new covalent compound namely g-C_3N_4 was predicted and synthesized in 1993 [74]. In 1996, it was demonstrated that this CN structure can have five different possible phases through theoretical studies; a-C_3N_4, b-C_3N_4, g-C_3N_4, cubic-C_3N_4 and pseudocubic-C_3N_4. When it is compared to other phases, g-CN possesses higher stability [75].

In the of synthesis of g-CN, usually precursors that are carbon and nitrogen rich with preformed C-N structures are used. Some examples are cyanamide, melamine, urea, and guanidine. These precursors are treated at high temperatures so polycondensation reaction takes place and a new polymer, g-CN forms. Reaction can be conducted under inert atmospheres (Argon, Nitrogen) or air, depending on the expected structure. This affects final g-CN's yield, surface properties, degree of condensation and etc [76] .

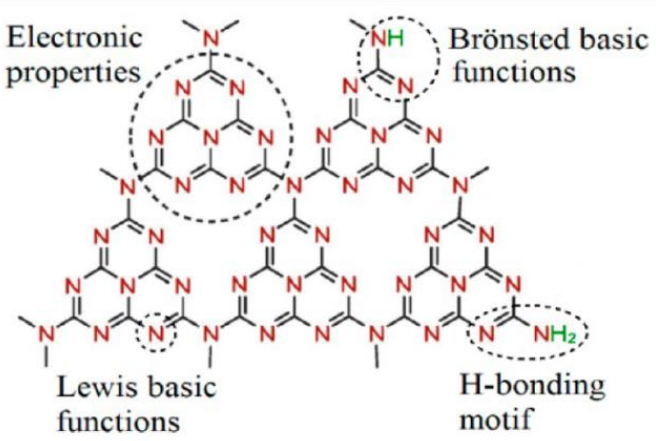

Figure 2.2: Representation of surface functionalities of g-CN [77].

g-CN has a π backbone and many unique surface properties which make it a suitable catalyst. Some of the surface functionalities can be seen in Figure 2.3. In addition to these properties, it holds thermal stability and chemical inertness which means it can be used in a variety of mediums at different temperature conditions.

The utilization of g-CN in catalytic studies started with organic reaction catalysis. Early applications include usage of g-CN as a metal-free, heterogenous catalyst for the cyclotrimerization reaction [78]. In 2008, it was shown that g-CN can be used as a photocatalyst in hydrogen production from water with visible light irradiation [79]. It was a breakthrough because high potential of g-CN in photocatalysis was shown for the first time. Later, g-CN was employed in NO decomposition [80], water splitting reaction [81], environmental remediation [82], CO_2 reduction reaction [83] and many more application. It should be also noted that g-CN offers a perfect environment for nanoparticle stabilization. A good support material should not only have large surface area but also have suitable chemical environment to stabilize nanoparticles and inhibit their movement or leaching during the catalytic reaction. It is possible to see g-CN in this role within the literature frequently [84], [85].

2.4 Black phosphorus

First synthesis of BP dates back to 1914. White phosphorus (WP) was tried to be converted into red phosphorus (RP) by the aid of pressure and temperature (1.3 GPa, 473 K). Accidently a new allotrope of phosphorus was discovered and named as BP [33]. Transformation was accompanied by a significant volume change and the density of BP was measured as 2.69 g/cm^3 which is higher than WP and RP. It was noted that this allotrope of phosphorus showed semiconductor behaviour with a band-gap value of 0.33 eV and high crystallinity with remarkable stability under air compared to WP and RP [86]. Later, with the same method the transformation of WP to BP was achieved more rapidly [87]. Bridgman came up with another synthesis method without the need of temperature and this time direct conversion of RP to BP, but this method required much higher pressures (8.0 GPa) [88]. Thus, all these methods suffered from low yields and it was not possible to conduct these types of syntheses with ordinary laboratory conditions. Additionally, the structure and crystallinity of BP obtained with these methods, strongly depended on temperature and pressure applied in the synthesis.

BP can be synthesized via using reflux methods with liquid Mercury (Hg) or Bismuth (Bi) [89]. Brown and Rundqvist (1965) used WP as a phosphorus source and kept it in a Bi reflux. Needle shaped BP was obtained, and it was reported that synthesized BP had bismuth impurity of 0.055% by weight [90]. Crystal structure of BP was investigated first time in this study and infinite puckered layer structure of BP was offered. Later, Maruyama et al., purified WP using nitric acid (HNO_3) and then transferred it into liquid Bi [91]. After keeping liquid Bi solution at 673 K for 20 hours and slowly cooling down to room temperature (0.3 K /min), need or thin rod like BP single crystals were obtained. Main drawbacks of these methods were elongated synthesis times and toxicity of used solvents and/or phosphorus source. Considering all methods mentioned above, synthesis of BP stayed as a challenging task for a long time due to hardness of processing, toxicity of used chemicals and low yields.

In 2007, Lange et al., showed BP could be synthesized using certain mineralizers without the aid of high pressure [36]. RP which is a non-toxic phosphorus allotrope was used as a phosphorus source. Gold, tin (Sn), tin(IV) iodide (SnI_4)were transferred into a silica ampoule with the phosphorus source and then the silica ampoule was evacuated and sealed. The temperature controllably increased to the range of 823 – 923 K and gradually slowed down to room temperature. This method yielded high quality BP crystals as it can be seen in Figure 2.3. Later, it was showed that mineralizers Sn and SnI4 are in fact sufficient for synthesis of BP thus there was no need to use rare and expensive Au in the synthesis of BP [92]. Role of mineralizers, nature of transformation and photocatalytic activity of BP synthesized from this method were studied in literature [93].

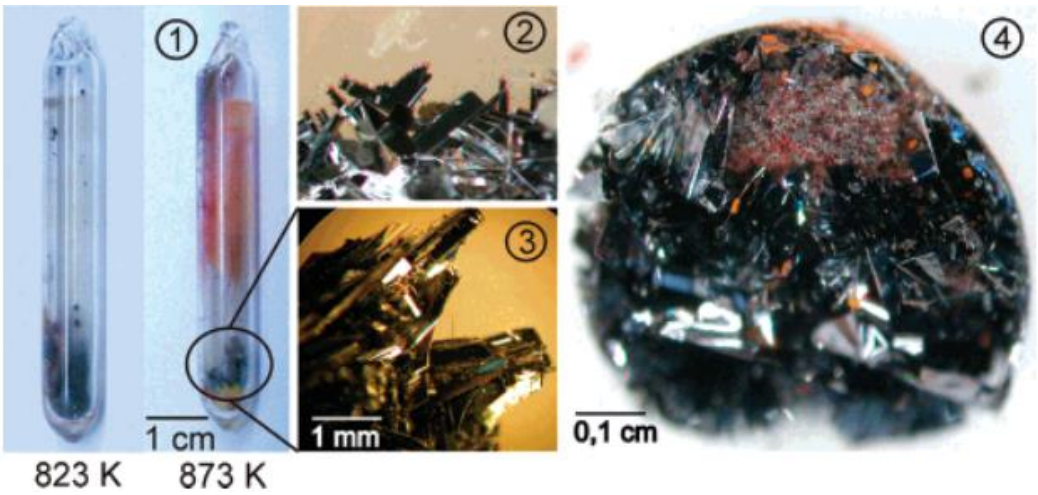

Figure 2.3: Picture 1 shows the Silica ampules used for the preparation synthesis of BP (picture 3). Picture 2 shows SnI_4 condensed on top of BP after thermal decomposition of Au_3SnP_7 at 1073 K reaction intermediate. BP grown on top of Au_3SnP_7/AuSn bulk can be seen at (picture 4). The mineralization agent SnI_4 (orange dots) is well separated from the bulk materials and BP and can be seen at pictures 2 and 4 [36].

It is possible to synthesise BP using various solvothermal methods. Firstly, BP nanosheets were synthesized by dissolving ammonium fluoride (NH_4F) and dispersing RP in distilled water and maintaining this mixture at 473 K for 16 hours after transferring it into a Teflon lined stainless steel autoclave [94]. After cleaning, polycrystalline BP nanosheets were obtained. Then, partially oxidized BP nanosheets were synthesized by Tian et al., in 2018 [95]. WP was used as a phosphorus source and it was mixed with ethylenediamine. Solution mixture transferred into Teflon lined autoclave and further into a furnace. Heating this mixture to the range of 333 - 413 K resulted with partially oxidized BP nanosheets. Further, more recent studies showed that it is possible to use this route with RP being the phosphorus source [96]–[98] . Commonly ethylenediamine was used as a solvent and mechanistic insights showed the importance of chosen solvent in these methods. Higher yields, ease of production and usage of RP instead of toxic and unstable WP makes these methods highly viable. However, these methods suffer from poor crystallinity.

There is one unclassified patented method worth to mention by Baillergeon at al. In this patented method, RP was thermally cycled in vacuum between 473 K and 673 K.

After cycling at least three times under constant vacuum, BP was removed from the vacuum chamber. There is no morphological and characterization data presented.

In order to effectively utilize BP and take advantage of its 2D properties such as confinement effect, BP needs to be exfoliated and namely phosphorene which are composed of single or few layer BP layers should be isolated [99]. These methods are called top-down procedures because bulk BP is being used to yield phosphorene. Firstly, analogous to graphene study by Novoselov et al., scotch-tape method was used for mechanical exfoliation of BP [100]. It revealed how electrical and optical properties change significantly when we go from crystal BP to 2D phosphorene However, in order to utilize phosphorene in photocatalysis, solvent assisted liquid phase exfoliation method is more suitable because simply it results with a higher yield using wet chemistry [101]. Type of exfoliation (shear or ultra-sonication) and solvent (mostly N-Methyl-2-pyrrolidone or N,N-Dimethylformamide) , time, temperature (usually ice-bath conditions) and isolation method (centrifugation with different rpm values) are important parameters of this procedure and extensively reported in literature [102]. One can design an exfoliation procedure according to needs of experiment and application and obtain isolated phosphorene with desired layer thickness. Other than liquid exfoliation methods, different methods to prepare phosphorene (electrochemical, laser assisted and etc.) can be found in literature [103].

In addition to top-down procedures described above, in limited numbers, there are bottom-up procedures which yield phosphorane while synthesising BP from a phosphorus precursor such as RP [94], [104].

BP and BP-based materials has found a place in catalysis applications in the field of mostly photocatalysis and electrocatalysis. In 2017, for the first time, it was shown that exfoliated BP is suitable for hydrogen evolution reaction (HER) with visible light irradiation by two different groups [105], [106]. Following that, new studies were conducted with construction of different BP-based materials for HER applications. In 2018, a 2D hybrid material, BP/WS_2 was synthesized for hydrogen production from water and this catalyst was shown to be able to be irradiated by near-infrared light [107]. Apart from hydrogen energy applications, BP and BP-based materials were employed as a photocatalyst in degradation reaction of organic molecules [108], CO_2 conversion reactions [109], organic molecule synthesis reactions [110] as well. In electrocatalytic applications, BP and BP-base materials were employed in HER [111], oxygen evolution

reaction (OER) [112], oxygen reduction reaction (ORR) and ethanol oxidation reaction (EOR) [113]. BP was also used as a functional material in sensor applications [114], battery applications [115] and etc. These reports overall show the high applicability and potential of 2D BP material in variety of fields.

2.5 g-CN/BP heterojunctions

It is possible to find a few studies which a heterojunction between g-CN and BP was formed. Without modifications such as doping or sizing down to quantum dots (QD) which is denoted as 0D materials, heterojunctions between these two materials (2D-2D) result with a type I interaction. Possible band structures when these two materials are contacted can be seen in Figure 2.4. As it can be said from this Figure, as long as BP conserves its 2D structure, type I heterojunction will be formed. Special case for BP QD will be discussed later.

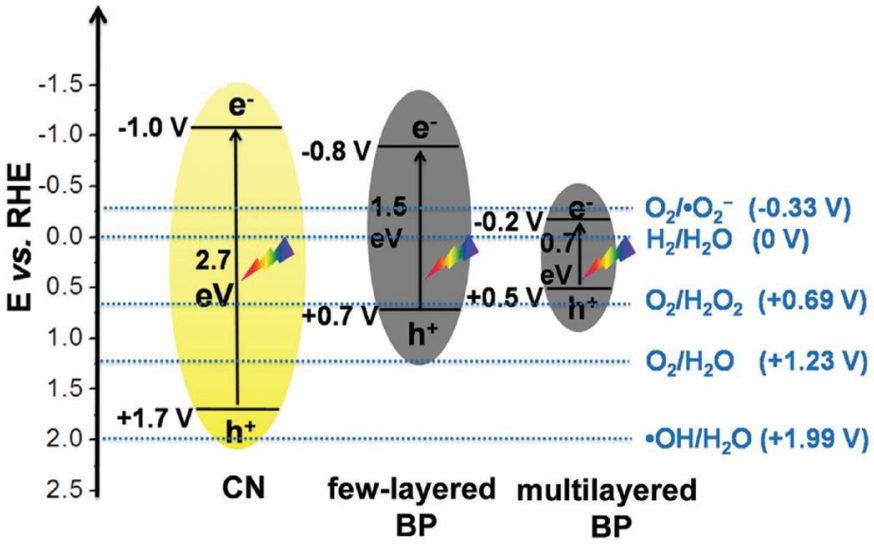

Figure 2.4: Schematic representation of band diagrams of g-CN and 2D BP [116].

In 2017, for the first time, a heterojunction of g-CN and BP was formed and this material was used in hydrogen production from water, using methanol as a sacrificing agent [43]. This new material showed hydrogen production ability both under visible light and near-infrared irradiation. Another study in 2018, showed the importance of morphology adjustment and claimed to set a 2D–2D van der Waals heterojunction between BP and g-CN [117]. Created heterojunction material was employed in hydrogen production. Moreover, in 2018, another group constructed covalent bonding between

phosphorus atoms from BP and carbon atoms from g-CN [27]. This material was tested in photocatalytic nitrogen fixation and showed great results. It was concluded that the C – P bond formed at the interface, greatly improved the charge transfer and additionally, stability of BP. In 2019, it was shown that, it is possible to synthesise a g-CN - BP heterostructure material directly from their precursors, urea and red phosphorus using a mechanical ball-milling technique [118]. This study offered a low-cost pathway with a great light absorption spanning from visible region to near infrared. Also, the catalyst showed high photocatalytic activity in hydrogen generation via water splitting and Rhodamine B (RhB) decomposition.

It is possible to form a type II heterojunction between g-CN and BP QD and it was presented in literature in limited numbers. In 2018, it was shown that it is possible to form a type II heterojunction between g-CN and BP QD [119]. In order to boost photocatalytic water splitting performance, BP QD were used as a cocatalyst and with visible light irradiation, hydrogen production from water was achieved. Other than this 0D-2D heterojunctions, a 0D-3D heterojunction photocatalyst was synthesized by placing BP QD (0D) under surface of g-CN material [120]. This photocatalyst took advantage of improved visible and near infrared light absorption and showed superior hydrogen evolution from water via water splitting.

2.6 g-CN/Metal and BP/Metal heterojunctions

g-CN/Metal heterojunctions are being widely used as photocatalysts in variety of reactions. Unique structure of g-CN makes it as a versatile platform for metal loading mostly in the form of NPs and thus it allows a very feasible approach to synthesise g-CN based photocatalysts. Metal nanoparticles can be synthesized in-situ on g-CN or they can be synthesized ex-situ and then supported on g-CN by other means. In 2009, for the first time, it was shown that ordered g-CN can be used as a host material for Platinum (Pt) [121]. This photocatalyst showed very promising results in hydrogen evolution from water and as a result metal decoration on g-CN both in-situ and ex-situ was revisited by many researchers [122]. In terms of decorated metal nanoparticles, g-CN/metal heterojunctions can be investigated in two subheadings. Firstly, supporting metal nanoparticles that have surface plasmon resonance (SPR) on g-CN was seen as a very beneficial strategy. Mainly, SPR inhibits the recombination of photoinduced charge

carriers on metal nanoparticle and in return photocatalytic activity is enhanced because these charges can be utilized effectively in the reactions. In 2013, Ag supported g-CN photocatalyst was reported as highly active in the degradation of organic contaminants [123]. Based on this idea, new photocatalysts based on g-CN that takes advantage of SPR properties of Ag, Au, Bi and etc. were synthesized and tried in different reactions such as hydrogen evolution and NOx removal [124], [125]. Second, metals that do not have SPR can be supported on g-CN and due to formation of Schottky barrier, photocatalytic activity is improved. Pt supported g-CN photocatalysts fall into this category. A very recent study for hydrolysis of AB by our group can be given as an example [126]. Another example to this case is Nickel (Ni) loaded g-CN photocatalyst for photocatalytic hydrogen evolution from water which was reported in 2015 [127]. The photocatalyst was synthesized via simple solvothermal method and showed enhanced hydrogen production activity. Lastly, AgPd NPs supported on g-CN which was reported by our group can be a great model for this kind of heterojunction [128]. Synthesized material was used in the photocatalytic hydrolysis of AB and showed a high photocatalytic dehydrogenation activity.

BP/Metal heterojunctions are a newly emerging topic. In 2017, reducing capacity of BP nanosheets for in-situ nanoparticle synthesis was reported [129]. Au nanoparticles were synthesized in-situ on BP nanosheets and characterized very well. This study showed that there is no need to use an external reducing agent when nanoparticles are wanted to be synthesized in-situ on BP. There is another study showing electrocatalytic oxygen reduction reaction activity of metal nanoparticles (Pt, Ag, Au) supported on BP [130]. Interfacial charge transfer properties of these heterojunction systems were investigated. For photocatalytic applications, there are not many articles that use BP/Metal heterojunctions. In 2016, it was reported that plasmonic Ag nanoparticles were synthesized on BP nanosheets and this nanohybrid was tested in photocatalytic contaminant degradation reaction [131]. The relation between BP layer thickness, Ag nanoparticle size and photocatalytic activity was evaluated. There is not any published article presenting metal loaded BP in the application of photocatalytic AB solvolysis yet (hydrolysis or methanolysis).

Chapter 3:
EXPERIMENTAL METHODS AND CHARACTERIZATION STUDIES

3.1 Used chemicals and reagents

For the synthesis of AgPd alloy nanoparticles, silver acetate (Ag(ac), 99.0%) was purchased from Alfa Aesar. Palladium(II) acetylacetonate ($Pd(acac)_2$, 99%), OAm (technical 70%), oleic acid (OAc, 90%) and ODE (90%) were obtained from Sigma Aldrich.

In the synthesis of mCN, guanidine hydrochloride (98%) was brought from Alfa Easer. Ammonium hydrogen difluoride (NH_4HF_2, 95%) was purchased from Roth. LUDOX HS-40 was obtained from Sigma Aldrich.

For the synthesis of BP, red phosphorus (98.9%) as phosphorus source was purchased from Alfa Aesar. Mineralizers tin (99.5%) and tin(IV) iodide were obtained from Alfa Aesar.

To be used in photocatalytic activity tests, AB (90%) and methanol were bought from Sigma Aldrich.

Remaining solvents (N-methyl-2-pyrrolidone, hexane, isopropanol, and ethanol) were purchased from Isolab in analytical quality. All chemicals used without further purification.

3.2 Synthesis of mesoporous graphitic carbon nitride

Synthesis of mCN was conducted by polycondensation of guanidine hydrochloride at high temperature using a hard-templating method. In a typical synthesis, 4.0 g of Guanidine Hydrochloride (GndHCl) was dissolved in 4 mL water in a beaker and added into 10 g of colloidal silica solution (Ludox HS40) with vigorous stirring. Colloidal silica particles act as a template here. The obtained mixture was continuously stirred overnight in an oil bath which the temperature was arranged to 323 K.

Following day, the mixture was allowed to cool down to room temperature. Collected solid material was crushed and grinded into powder in a mortar and then transferred into a tubular furnace with a quartz crucible with lid. The temperature was raised to 823 K in 2 hours and after keeping the material at 823 K for 2 more hours, it was naturally cooled

down to room temperature. All synthesis was conducted under inert Argon atmosphere. In a different container a solution of 4 M, 200 mL of NH_4HF_2 was prepared. Then, yellow powder obtained from tubular furnace was transferred into this solution and it was mixed for 2 days to etch the silica template from the material. After etching process, the product was washed with water and ethanol repeatedly with the help of centrifugation. Finally, it was dried and stored for future use.

3.3 Synthesis of black phosphorus

BP was synthesized using modified chemical vapor transport method presented in the literature [132], [133] . It is stated that mineralizers such as Sn and I that are being added to ampoule with phosphorus source are crucial for the high-yield synthesis of BP and it is being studied in literature [134]. Mineralizers act as a starting point for crystal growth and nucleation starts with intermediate phases of these mineralizers with phosphorus [135]. 500 mg RP, 20 mg Sn and 10 mg SnI_4 were transferred into a quartz ampoule with 20 cm length and 1.5 cm diameter. Specially designed quartz ampoules can be seen in Figure 3.1.

The ampoule was sealed under high vacuum and it was placed horizontally into a muffle furnace. Firstly, temperature was slowly increased to 893 K and kept there for 5 hours. At that stage, all reactants except Sn were in gaseous phase. Then, the temperature was slowly decreased to 758 K and it was revealed by in-situ imaging that solidification and crystallization of BP develops at this stage of synthesis [135] . After 2 hours at 758 K, to avoid a sharp temperature drop the temperature was controllably decreased to 393 K and then cooled down naturally to room temperature. The ampoule was opened under toluene at room temperature and single crystalline BP was obtained. BP was sonicated in absolute ethanol for 30 minutes to remove impurities such as mineralizers and untransformed Red Phosphorus. Purified BP crystal was put into a Schlenk tube which is vacuumed and filled with Argon gas and kept at container for further use.

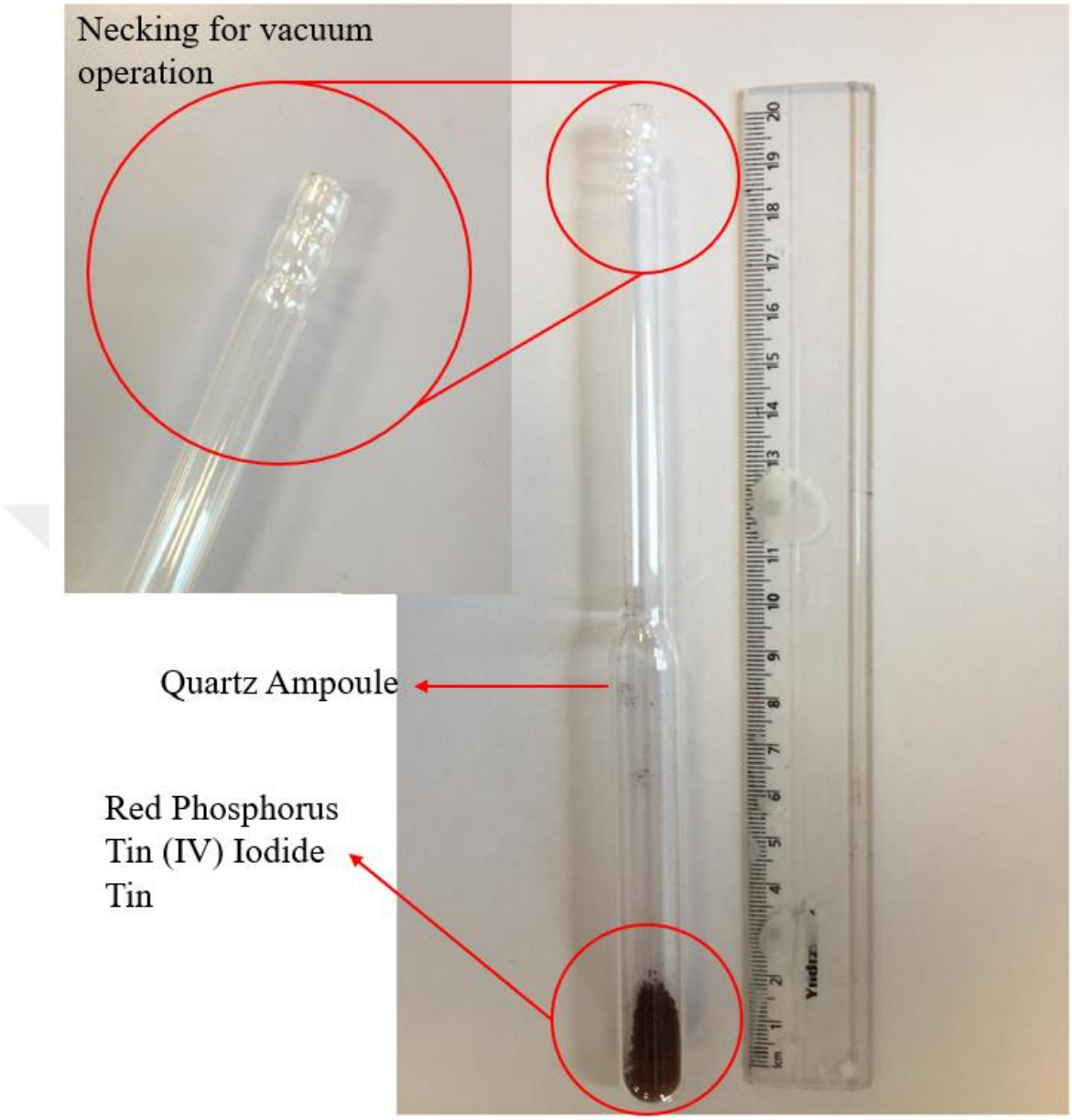

Figure 3.1: Designed quartz ampoule for the synthesis of BP.

3.4 Synthesis of Silver, Palladium and Silver-Palladium alloy nanoparticles

Monodisperse AgPd alloy nanoparticles were synthesized by using a colloidal wet-chemistry approach. For synthesis of Ag_1Pd_1 alloy nanoparticles, 0.5 mmol of $Pd(acac)_2$ and 0.5 mmol of Ag(ac) were transferred into a mixture of 4.5 ml OAc, 0.5 ml OAm and 10.0 ml ODE. This synthesis was conducted in a four-necked glass reactor under inert Argon gas atmosphere. Used synthesis setup with its components can be seen in Figure 3.2 in details.

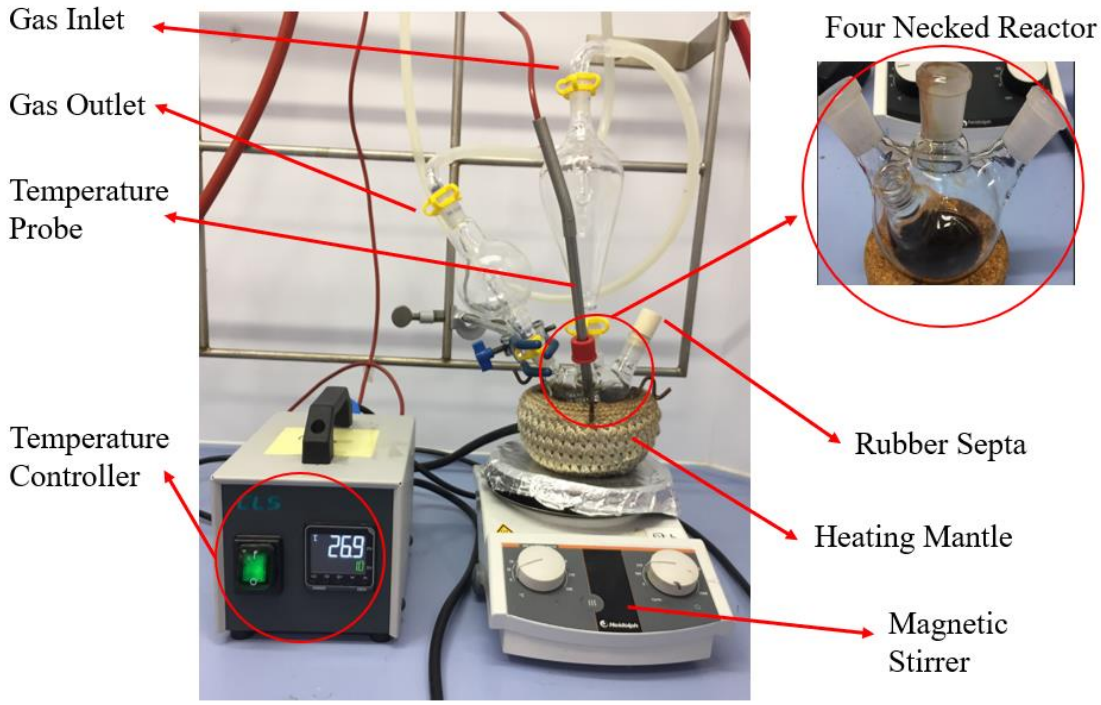

Figure 3.2: Synthesis setup with designed four-necked glass reactor for the colloidal synthesis of AgPd nanoparticles.

Firstly, temperature was raised to 333 K to completely dissolve precursors in the solvent. Then, the temperature was increased to 453 K. Resulting solution was kept at 453 K for 20 minutes. After cooling down to room temperature naturally, nanoparticles were isolated from the solution by addition of isopropanol and centrifugation (9000 rpm, 12 min). The centrifugation was repeated with ethanol and separated nanoparticles were taken into hexane dispersion. Nanoparticles were kept in dark conditions. ICP-MS analysis was used to determine the elemental composition of synthesized nanoparticles. Additionally, three AgPd alloy nanoparticles with different compositions were synthesized using same experimental setup and different metal precursor amount.

Monodisperse Pd nanoparticles were synthesized by OAm mediated reduction of $Pd(acac)_2$ with morpholine borane at 343 K. After reduction of the mixture, nanoparticles were collected by addition of ethanol and centrifugation. Nanoparticles were taken into hexane dispersion and kept for further use.

Monodisperse Ag nanoparticles were synthesized by thermal decomposition and reduction of Ag(ac) in OAm and OAc at 453 K. In a typical synthesis, 1.0 mmol Ag(ac),

10.0 ml ODE, 1.0 ml OAc and 1.0 ml OAm were mixed and continuously stirred under Nitrogen flow in our four-neck glass reactor. Temperature was firstly increased to 333 K and then 453 K. After staying there for 20 minutes, the mixture was cooled down to 4313 K and centrifuged with addition of isopropanol (9000 rpm, 12 min). Centrifugation repeated with ethanol and final nanoparticles were taken into hexane dispersion. Ag nanoparticles were stored in hexane in dark conditions.

3.5 Preparation of mCN/BP and mCN/BP/AgPd nanocomposites

Before addition of AgPd alloy nanoparticles, firstly mCN/BP binary nanocomposite was prepared. Overall scheme for the preparation of mCN/BP/AgPd nanocomposites can be seen in Figure 3.3. Firstly, 20 mg BP was sonicated in 10 ml N-methyl-2-pyrrolidone (NMP) for 8 hours in a sonicator bath which the temperature was arranged to 288 K under dark conditions in order to inhibit degradation of BP through oxidation. In a different container, synthesized mCN (100mg) was dispersed in NMP with the help of sonication for 2 hours. Next, mCN dispersion solution was slowly added to BP solution under sonication. This mixture was continued to sonication for 4 more hours to ensure assembly of BP on mCN. To separate mCN/BP binary nanocomposite from the mixture, the solution was centrifuged and washed with ethanol two times (9000 rpm, 20 min). Obtained solid mCN/BP binary nanocomposite was dried and stored for further use. Optimum weight ratio was detected as 5:1 (mCN to BP). Different samples with varying ratios were prepared by addition of BP to mCN.

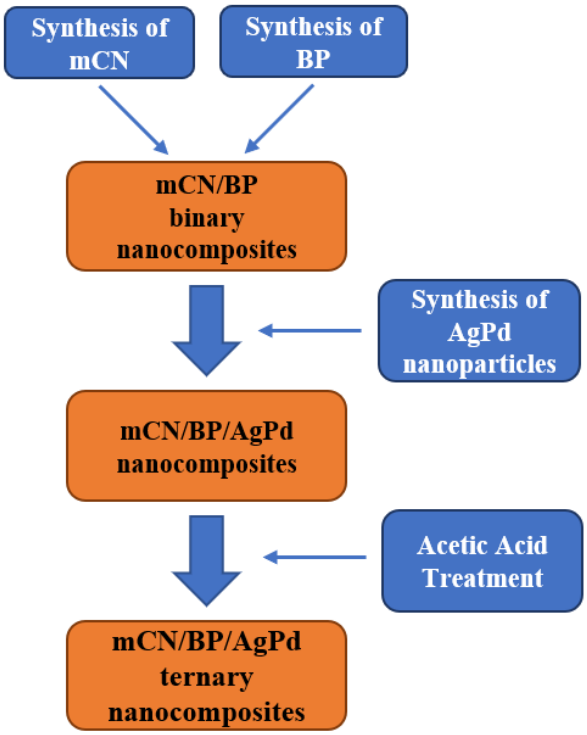

Figure 3.3: Pathway for the synthesis of mCN/BP/AgPd and mCN/BP/AgPd/AT ternary nanocomposites.

mCN/BP/AgPd ternary nanocomposites were prepared through decoration of synthesized AgPd alloy nanoparticles on mCN/BP binary nanocomposite. Firstly, density of hexane dispersion of AgPd alloy nanoparticles was determined with a simple gravimetric method. Then, 96 mg mCN/BP was weighed and dispersed in a mixture of hexane and ethanol (10 ml hexane and 20 ml ethanol) in the sonicator bath. Next, 32 mg of alloy nanoparticles taken from their hexane dispersion was slowly added to mCN/BP binary nanocomposite dispersion under sonication. After addition, mixture was continued to sonication for 2 more hours to establish a well assembly. After sonication, final mCN/BP/AgPd material was isolated by removing the ethanol and hexane from solution and powder material was obtained.

3.6 Surface cleaning of mCN/BP/AgPd ternary nanocomposites

In order to make surface more available for the reaction and increase catalytic activity, surface organic groups of AgPd alloy nanoparticles were removed by two different methods. Firstly, samples were treated under Argon flow at 573 K for 2 hours. 100 mg mCN/BP/AgPd ternary nanocomposites transferred into a quartz crucible and

then to tubular furnace. After heat treatment, the furnace was cooled down to room temperature and material taken out from furnace (mCN/BP/AgPd/HT). Second, an acetic acid treatment was applied to materials. 100 mg mCN/BP/AgPd ternary nanocomposite was added to a round bottom flask with acetic acid (100 ml). Flask was placed in an oil bath which the temperature was arranged to 343 K. Under reflux conditions, mixture was stirred overnight at this temperature. Next, mCN/BP/AgPd ternary nanocomposite were isolated with centrifugation (8500 rpm, 12 min) and washing was done three times with ethanol. The final ternary nanocomposite, mCN/BP/AgPd/AT was dried and kept for further use.

3.7 Instrumentation

X-Ray Diffraction (XRD) is a technique used for phase identification and structures of crystalline and semi-crystalline materials. With this technique, valuable information such as lattice parameters, crystallinity of sample and etc. can be gained. An XRD instrument consists of an X-Ray Source which is the incident X-Ray is created, sample holder which is the desired sample is placed and finally an X-Ray detector which detects diffracted X-Rays coming from the sample. Main purpose is to detect waves that interference constructively at certain degrees. By changing the angle between source and sample, the waves that obey the Brag's Law are detected thus these waves result with constructive interference and give a distinct diffraction pattern. Schematic representation of X-Ray Diffraction mechanism and Bragg's Law can be seen in Figure 3.4.

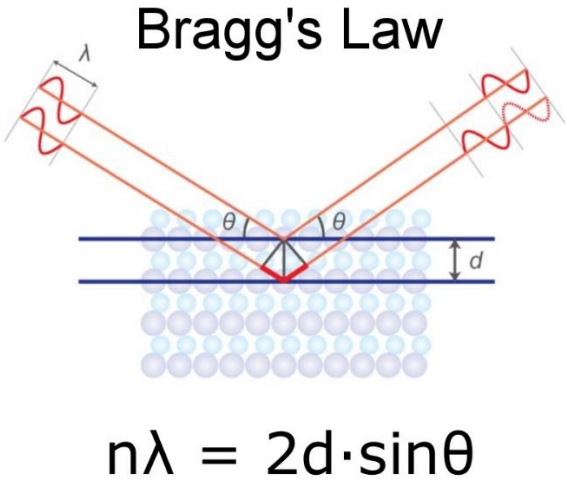

Figure 3.4: Schematic representation of X-Ray Diffraction mechanism and Bragg's Law.

In order to evaluate crystal structures of materials XRD studies were conducted using Bruker D8 instrument. Cu Kα radiation (λ = 1.5406 Å) was used as X-Ray source (30kV, 10 mA) and 2θ range of 10 – 80 was scanned.

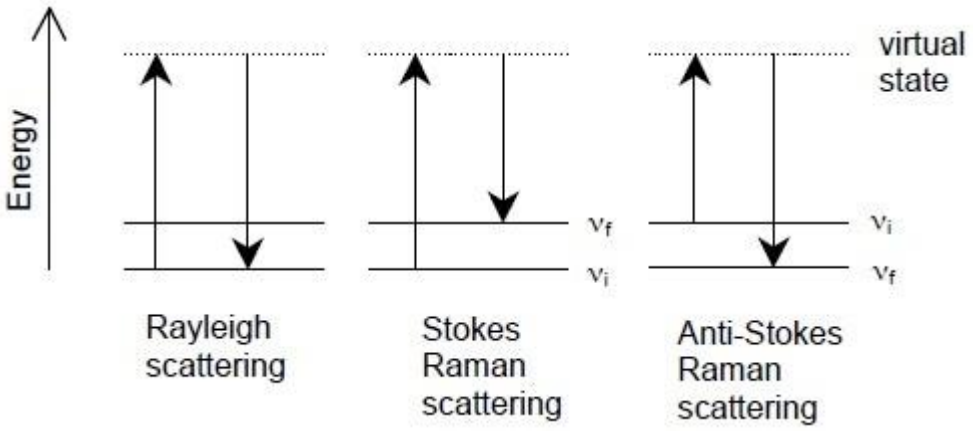

Figure 3.5: Representative energy level diagram of Rayleigh and Raman Scattering.

Raman spectroscopy is a common method to analyse optical properties of layered materials and frequently used for BP characterization [136]. Raman spectroscopy is based on inelastic scattering of incident photons, which is called Raman scattering [137]. A monochromatic light source in the form of mostly laser is used to excite the material. This light can interact with molecular vibrations, phonons, or other excited properties of the material and in return a change in the incident photons' energy is observed. Measuring this shift in the energy, called Raman Shift, gives deep information about the material. Representative energy level diagram of Rayleigh Scattering which is the elastic scattering next to Stokes and Anti-Stokes Raman scattering can be seen in Figure 3.5. Raman spectroscopy was applied to synthesized BP crystal using excitation source of 532 nm laser with a Renishaw inVia Raman microscope.

For the analysis of surface area (BET) and pore size, Micromeritics ASAP 2020 accelerated surface area and porosimetry system was used. The Brunauer, Emmett and Teller (BET) theory is frequently used to evaluate the gas adsorption data and generate a specific surface area result. The theory relies on the adsorption of gas molecules on solid surfaces and the pressure difference. Samples are needed to be degassed prior to measurement in order to have a clean and ready surface for the adsorption of probe gas molecules.

Scanning electron microscopy (SEM) was used to for the investigation of the morphology of the materials. SEM works on the principle of generating an electron beam and scanning a sample surface with this generated electron beam. With different detector configurations, varying signals in the form of electrons or energy that arise from interactions between sample and incident electrons can be captured. This operation needs to be conducted in a high vacuum chamber because incident electrons are only wanted to interact with sample atoms. For SEM analysis of the samples, Zeiss Evo LS15 Scanning Electron Microscope was used. In order to analyse particle size and distribution, Transmission electron microscopy (TEM) was performed. In terms of electron generation TEM is similar to SEM, however, in TEM electrons are transmitted through the sample and captured electrons give rise to an image. TEM offers greater resolutions and smaller particles which cannot be detected in traditional SEM can be observed. The fundamental difference between SEM and TEM technics can be seen schematically in Figure 3.6. TEM images were recorded on a Hitachi HT7700 with EXALENS (120 kV) working at a high-resolution (HR) mode. Samples were prepared on carbon film coated copper grids in laboratory.

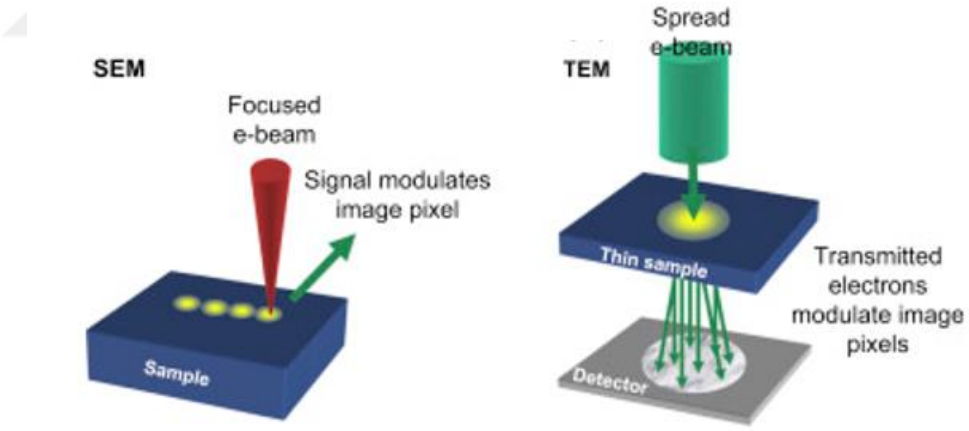

Figure 3.6: Schematic difference in SEM and TEM working principles [138].

Ultraviolet−visible−near-infrared (UV−vis− NIR) spectroscopy lets one to investigate important optical properties of materials such as absorption, transmission, and reflectance behaviour. In a very basic configuration, a sample is irradiated with an UV, visible or infrared light and a detector observes the light after its interaction with the sample. When dealing with photocatalysts, these optical properties, especially absorption behaviour, hold upmost importance. Within this equipment, there are different modes

used for detection of different properties. Diffuse reflectance spectroscopy (DRS), makes possible the detection of absorption behaviour of solid materials through reflectance measurement. For DRS measurements, Shimadzu UV-3600 UV−vis−NIR spectrophotometer was used with integrated sphere attachment. Measurement configuration can be seen in Figure 3.7.

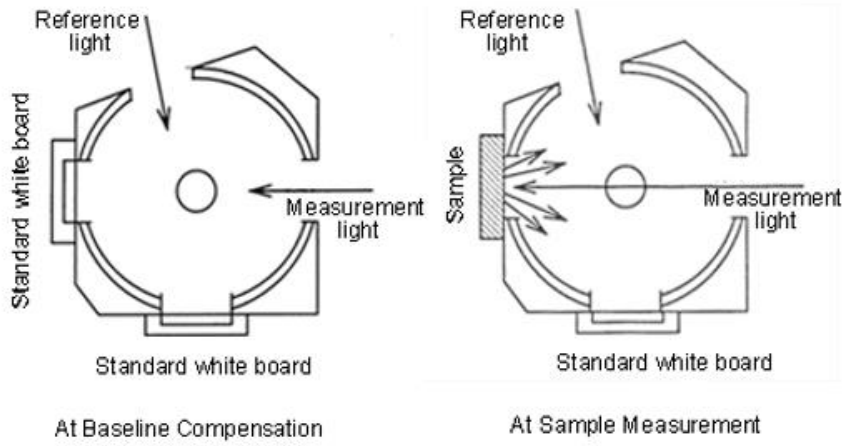

Figure 3.7: Measurement configuration of DRS with an integrating sphere attachment.

Elemental composition analysis of samples was done through Inductively coupled plasma-mass spectroscopy (ICP-MS). Mass spectroscopy measures the amount of ionized species in a solution using mass to charge ratios. In ICP-MS, a plasma is used for the ionization of the species [139]. Detection limit can be arranged to parts per million (ppm) or parts per billion (ppb) units using appropriate standard solutions. Measurements were performed on an Agilent 7700 ICP mass spectrometer equipped with an ASX-500 autosampler. Measurement's main six processes can be seen schematically in Figure 3.8. The method's reliability strongly depends on the complete dissolution of the solutes in the used media. For the species that are hard to solve in traditional methods, a microwave assisted approach is used. The ICP-MS samples were prepared in laboratory using StartD Milestone Microwave Digestion.

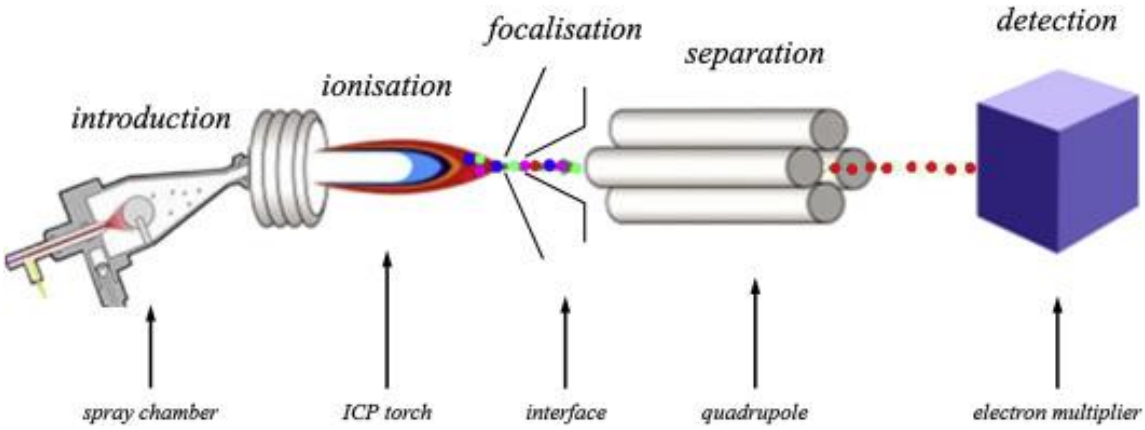

Figure 3.8: Schematic representation of ICP-MS detection process [140].

3.8 Photochemical characterization studies

When a semiconductor material is irradiated with a light source having greater energy than its band gap, absorption, and emission processes in different electronic energy levels of material takes place. These emission processes are called photoluminescence (PL) in a general sense. PL can be in the form of phosphorescence or fluorescence. PL Spectroscopy offers very valuable information about charge carrier recombination behaviour which is one of the most important aspects that one must consider when dealing with semiconductor based photocatalysis. Upon creation of light induced charge carriers, these charges tend to recombine. Recombination results with PL behaviour. Representative energy diagrams and PL processes related to absorption and emission can be seen in Figure 3.9. On this aspect, both steady state and time resolved PL studies were conducted. Steady state PL spectroscopy data was evaluated with Agilent Cary Eclipse PL with a 320 nm excitation from a Xenon lamp. Time resolved PL spectroscopy data was recorded with an Edinburgh Instruments FLS1000 spectrometer using a 377 nm laser excitation and the data was fitted with Fluoracle software package.

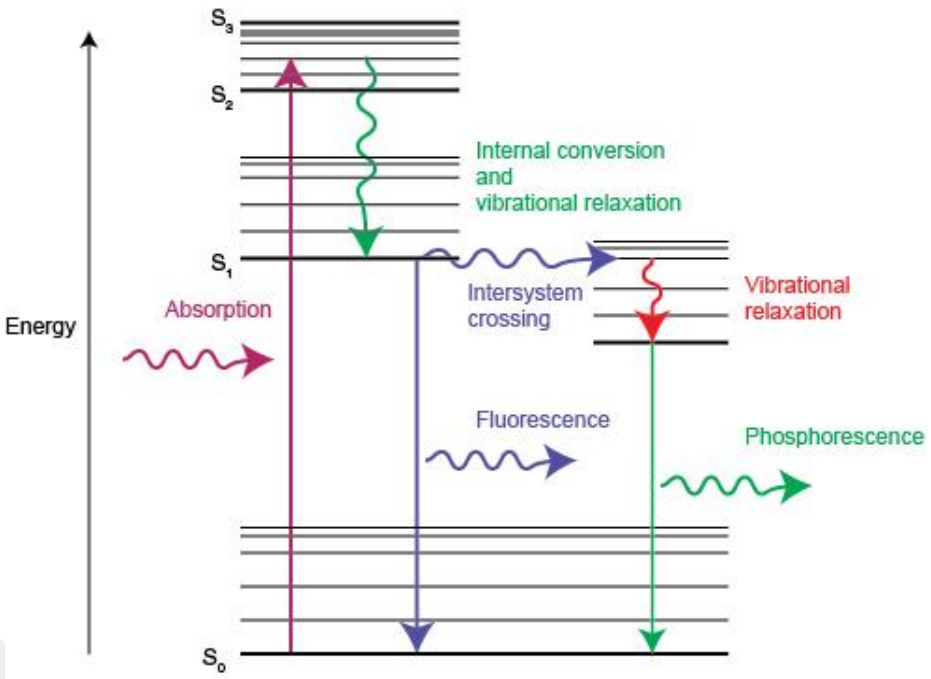

Figure 3.9: Representative energy diagram shows irradiation of material with a light source and the resulting PL processes.

To understand photoinduced charge movements better, band positions of the semiconductors were investigated. Valence-band X-ray photoelectron spectroscopy (VXPS) is a method based on X-Ray photoelectron spectroscopy (XPS). The sample is radiated with X-rays and as a result, electrons are ripped from the material. This can be applied to core electrons or valance electron of the material. When the process is focused on the valance energy region of the material, it is called VXPS. A detector measures the energies of ripped electrons from valance region and it enables the observation of valance energy level of the material. VXPS measurements was done with a Thermo Scientific Kα X-ray photoelectron spectrometer equipped with an aluminium anode (Al Kα, 1468.3 eV).

3.9 Photocatalytic hydrogen generation studies

The photocatalytic activity of mCN/BP/AgPd ternary nanocomposites was assessed in the methanolysis of AB with quantifying the evolved hydrogen gas amount by traditional reverse burette system that uses water displacement principle. Experimental setup can be seen in Figure 3.10 (a). Setup consists of reverse burette system for

quantification of gas and mirror system for photocatalytic reaction housing. Mirrors were used in the system to minimize the amount of light escape.

In a typical catalytic test, 10 mg mCN/BP/AgPd ternary nanocomposite or other photocatalyst was transferred into 7 ml of methanol (deaerated with Argon) and the mixture was sonicated 30 min. After sonication, dispersion was added to a jacketed glass dehydrogenation reactor (20 mL). Designed glass reactor can be seen in Figure 3.10 (b). The reactor has a neck that enables the addition of AB to start the reaction and also a valve which is connected to reverse burette system so evolved hydrogen volume can be tracked. After transfer of photocatalyst to reactor, the neck was closed via rubber septum. The reactor was placed on a stirrer and continuously stirred throughout the reaction with a Teflon-coated inert stirring bar. In order to control the temperature of the reaction environment precisely, a water circulator was used and arranged to 25 °C.

In a separate vial, 1 mmol AB was mixed with 3 ml of methanol and completely dissolved. To start the catalytic test, this AB solution was rapidly injected to the reactor using a syringe through rubber septum. With continuous stirring, evolved hydrogen gas volume was tracked by following the water level change. Other than no light and white light catalytic tests, all photocatalytic activity was evaluated with blue light illumination.

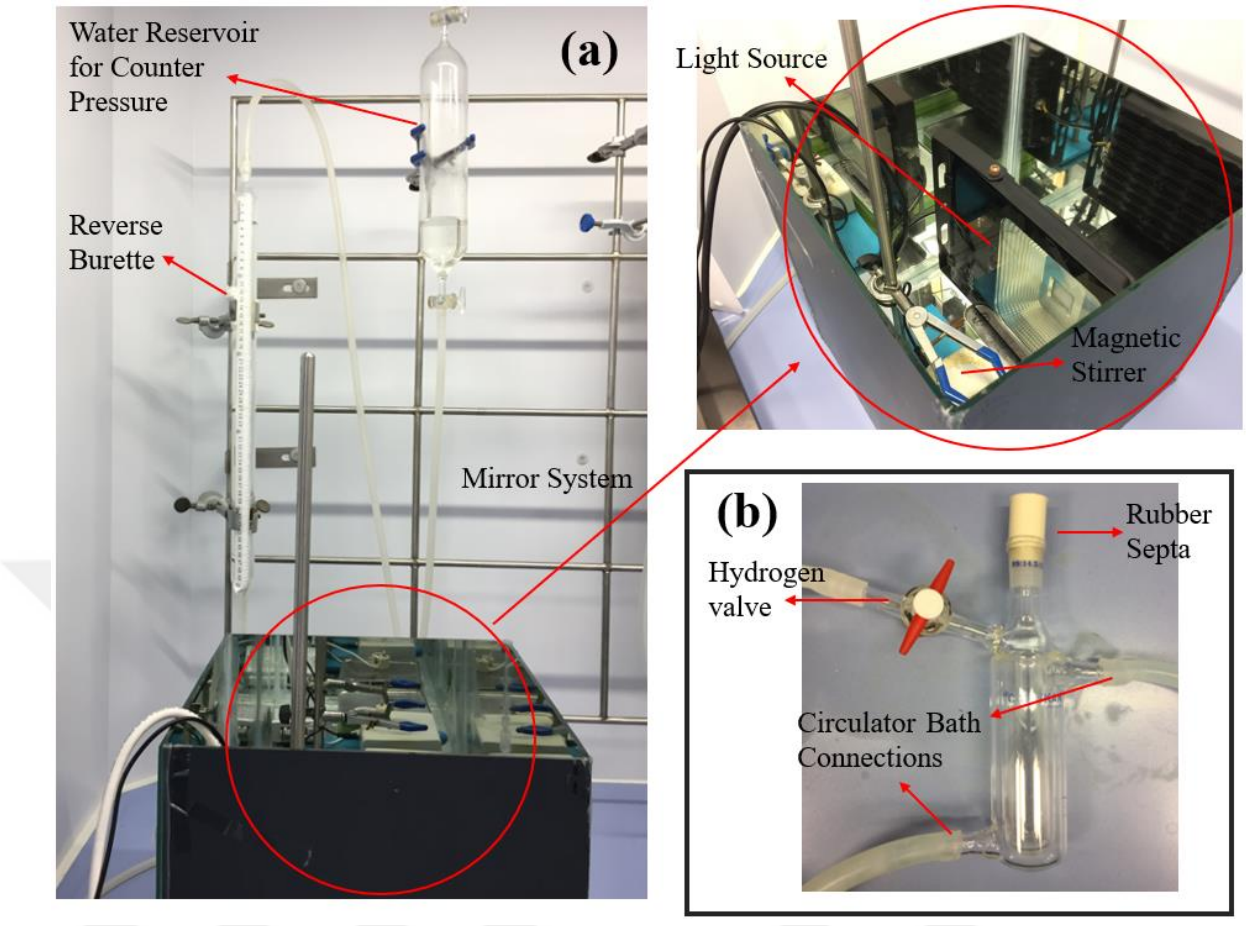

Figure 3.10: (a) Photocatalytic test setup and b) designed dehydrogenation reactor.

3.10 Assessment of photocatalytic activity

For the comparison and assessment of photocatalytic activity, a very common unit, turnover frequency (TOF) was used from the initial linear portion of each dataset. TOF is calculated with the formula below:

$$TOF = \frac{mol\ H_2\ evolved}{mol\ catalyst\ \times time}$$

Evolved hydrogen mol was calculated through volume of the hydrogen gas that was followed via reverse burette system. Catalyst mol was determined through ICP – MS measurements. Firstly, weight ratio of the catalyst (AgPd alloy nanoparticles) was detected and then it was transferred into molar quantities. Here, loaded total metal nanoparticle amount was used for the calculation of TOF. Other methods including only counting surface atoms can be applied. For time unit, minutes were used.

Chapter 4:
RESULTS AND DISCUSSION

4.1 Materials characterization

Figure 4.1 (a) and Figure A.1 show the TEM images of as-synthesized Ag_1Pd_1 alloy nanoparticles along with their associated particle size histograms. Representative TEM images were recorded from the hexane dispersions of nanoparticles at varying magnifications. It can be seen clearly from the TEM images that Ag_1Pd_1 nanoparticles hold high monodispersity and have average particle size as 2.6 nm. In Figure 4.1 (b), high-resolution transmission electron microscopy (HR-TEM) image of several distinctive Ag_1Pd_1 alloy nanoparticles can be seen. This image clearly presents the polycrystalline structure of the nanoparticles. Additionally, the lattice distance of an Ag_1Pd_1 alloy nanoparticle was calculated as 0.231 nm which evidently confirms the alloy (solid solution) formation between Pd and Ag because it is larger than that of Pd (0.223 nm) and narrower than Ag (0.234 nm). Additionally, TEM images of synthesized AgPd alloy nanoparticles with different compositions ($Ag_{25}Pd_{75}$, $Ag_{60}Pd_{40}$ and $Ag_{80}Pd_{20}$) can be seen in Figure A.2. As it can be concluded from Figure A.2, all the alloy nanoparticles showed high monodispersity with a narrow distribution of particle size. This information makes the composition related catalytic activity investigation of these nanoparticles highly feasible.

Next, as-synthesized colloidal nanoparticles were decorated on mCN/BP binary nanocomposites via liquid-phase self-assembly method. As it can be concluded from TEM images of mCN/BP/AgPd ternary nanocomposites presented in Figure 4.1 (c), as-synthesized colloidal Ag_1Pd_1 alloy nanoparticles successfully decorated on the binary mCN/BP nanocomposites. No clumped or agglomerated particles are observable. In addition, the nanoparticles preserve their initial morphology and particle size of after their assembly on mCN/BP nanocomposites. This is attributed to the stabilization effect of nitrogen sites of mCN (C=N and $-NH_2$) and phosphorus sites of BP. To make surface more available for catalysis and increase catalytic activity, surfactants on the surface of AgPd alloy nanoparticles were removed by acetic acid treatment. As it can be seen from Figure 4.1 (d), morphology and particle size were retained and there was no significant change in the structure after the acetic acid treatment.

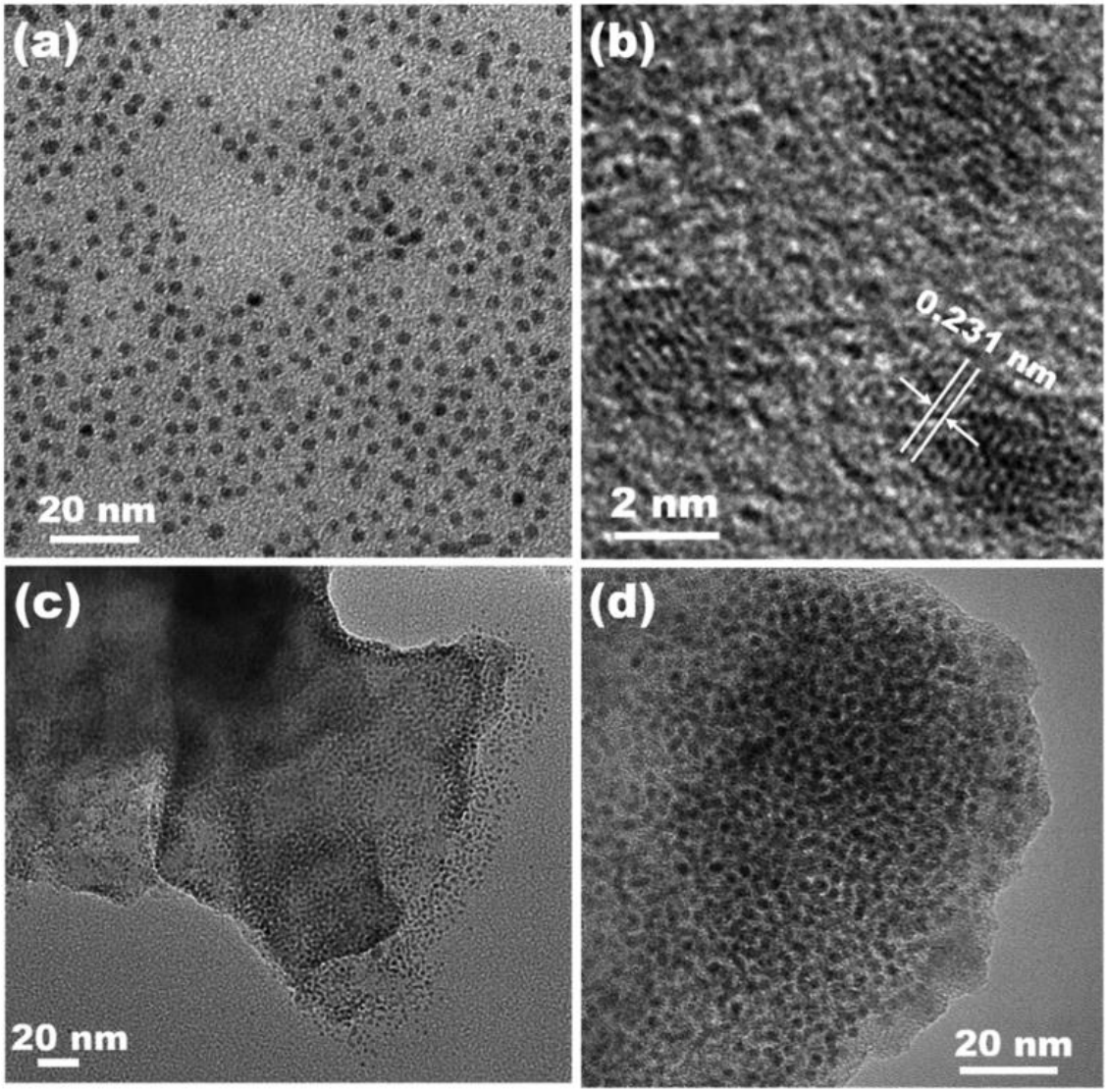

Figure 4.1: 1 TEM and HR-TEM images of colloidal Ag_1Pd_1 alloy nanoparticles (a, b) and TEM images of binary nanocomposite mCN/BP/AgPd (c) and ternary nanocomposite mCN/BP/AgPd/AT (d).

Representative TEM images of bare mCN along with bare BP are depicted in Figure A.3. Additionally, 2D nature of crystalline BP can be clearly observed from SEM images of BP nanoflakes, presented in Figure A.4.

The crystal structures of all synthesized materials including bare mCN and BP, mCN/BP binary nanocomposites and mCN/BP/AgPd/AT ternary nanocomposites were studied by XRD patterns. XRD patterns of these materials can be seen in Figure 4.2. The XRD spectrum of bare BP shows three distinctive and sharp diffraction peaks at 2θ= 17°, 34.5°, and 52.5°. These peaks are readily assigned to (020), (040), and (060) planes of orthorhombic BP, respectively. When XRD spectrum of bare mCN is evaluated, an

intense and broad diffraction peak can be spotted at 2θ= 28°. This diffraction peak is resulted from interplanar stacking of conjugated aromatic system and attributed to (002) plane of mCN. Second peak around 13° resembles the in-plane structural packing motif of mCN and assigned to (100) plane. When the XRD spectra of mCN/BP binary nanocomposites were evaluated, it was seen that characteristic peaks of bare BP and mCN were well preserved as expected and no alteration is observed in their crystal structure. The XRD pattern of mCN/BP/AgPd/AT nanocomposites shows three dominant peaks at 2θ= 17°, 28°, and 38.8°. These peaks are attributed to (020) plane of orthorhombic BP, (002) plane of mCN and (111) plane of face-centred (fcc) cubic AgPd alloy nanoparticles, respectively. This clearly indicates successful formation of ternary nanocomposites. However, it should be noted that intense and sharp peaks of crystalline BP were disappeared, and weak shoulder peaks have appeared. This can be explained by partial oxidation of BP due to acetic acid treatment and loss of crystallinity partially because of the creation of BP nanosheets.

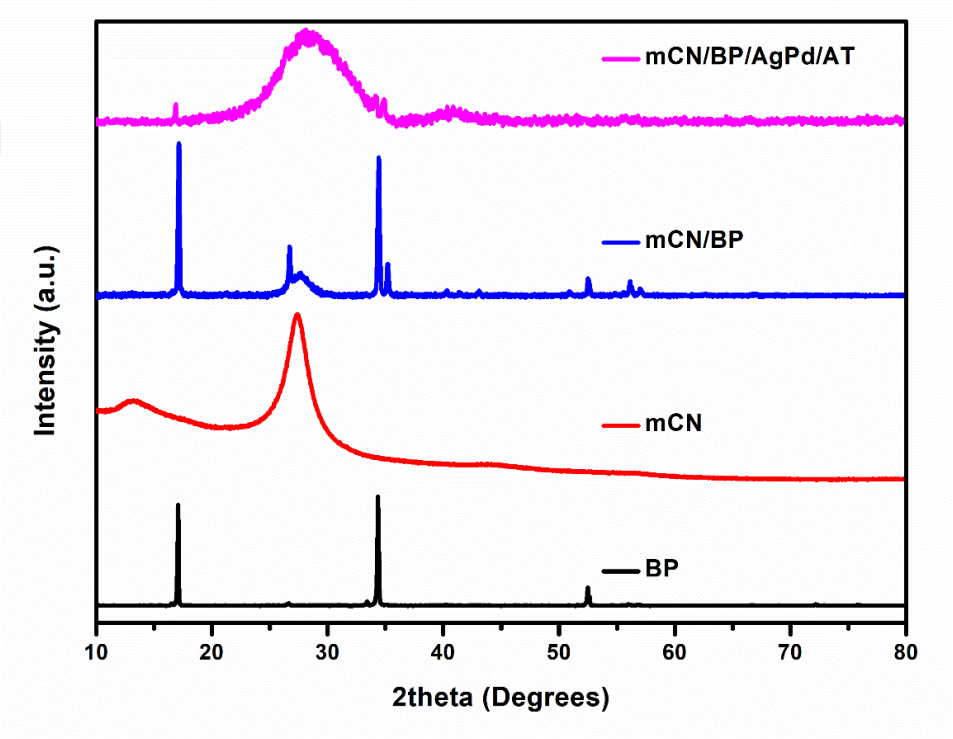

Figure 4.2: Powder XRD Spectrum of synthesized and prepared materials.

Additionally, XRD spectrum of ex-situ synthesized AgPd alloy nanoparticles ($Ag_{80}Pd_{20}$, $Ag_{60}Pd_{40}$, Ag_1Pd_1, $Ag_{25}Pd_{75}$) can be seen in Figure A.5. These XRD spectrums confirm the formation of alloy structures by giving a signal between (111) planes of fcc-Ag and (111) planes of fcc-Pd.

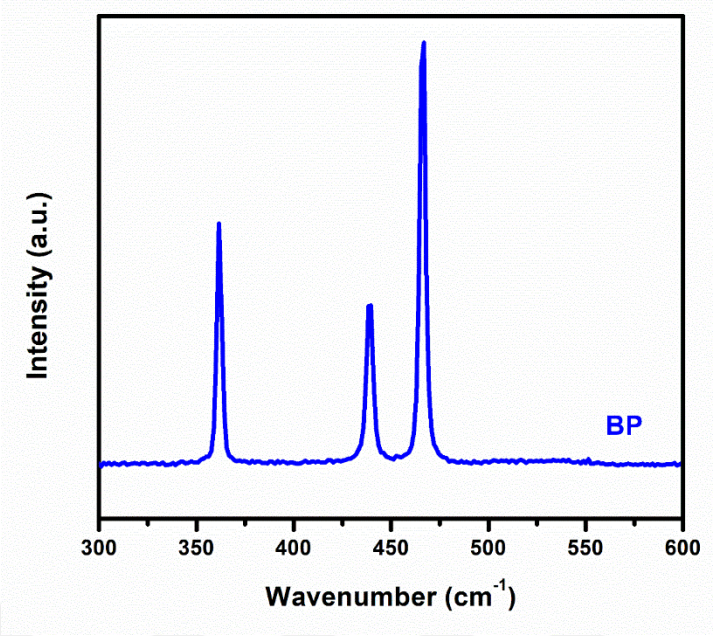

Figure 4.3: Raman spectra of synthesized BP showing characteristic peaks at 362 cm^{-1}, 438 cm^{-1} and 467 cm^{-1}.

Raman spectrum of synthesized BP can be seen in Figure 4.6. In the spectrum, three characteristic peaks of BP were observed at 362 cm^{-1}, 438 cm^{-1} and 467 cm^{-1} representing Ag_1, B_{2g} and A_g^2 phonon modes, respectively. Graphical representation of these phonon modes can be seen in Figure A.6. Positions of these characteristic peaks can have slight shifts depending on some conditions such as layer thickness and applied strain [136].

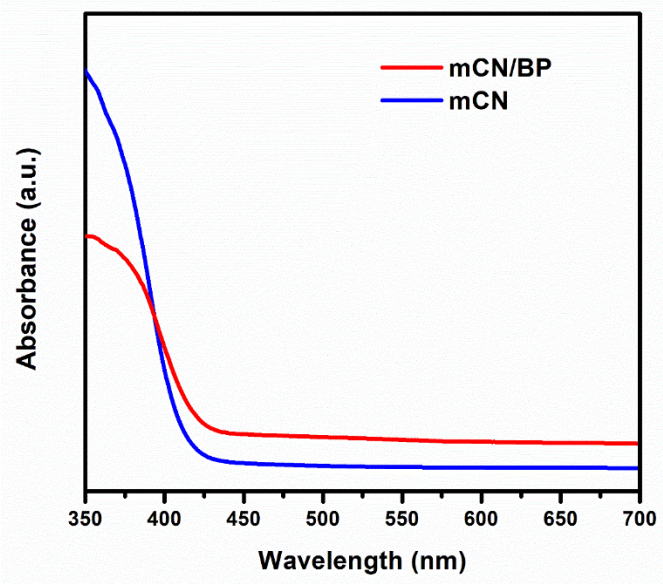

Figure 4.4: Absorption data of mCN and mCN/BP gained from UV−vis−NIR diffuse reflectance spectrum.

The absorption behaviour of mCN and mCN/BP nanocomposites was analysed by UV−vis− NIR diffuse reflectance spectroscopy (DRS) and the results can be seen at Figure 4.4. After addition of BP to mCN, it can be seen that absorption behaviour has been enhanced and the new material mCN/BP binary nanocomposites show higher absorption in visible region. This enhancement satisfies one of the most important criteria in photocatalysis which is the absorption ability in visible region. From absorption data, corresponding Tauc plots were formed to evaluate band gap values and they can be seen in Figure 4.5. According to these plots, indirect band gap of the binary nanocomposite mCN/BP has a lower value (2.76 eV) then bare mCN (2.87 eV). This is another indicator showing that efficiency of absorption has increased. This increased absorption ability in visible region of the spectrum can result in the generation of increased number of photoinduced electron and hole pairs which is very beneficial for photocatalytic applications that desired to be conducted in visible region.

The pore size and surface area analysis of bare mCN and mCN/BP binary nanocomposites were performed with Brunauer – Emmett − Teller (BET) and Barrett – Joyner – Halenda (BJH) methods, respectively. N_2 adsorption/desorption isotherms of bare mCN and binary nanocomposite mCN/BP can be seen in Figure A.7. A classic type IV adsorption/desorption isotherm was observed for both materials, which shows the mesoporous nature of materials. BET surface area for mCN was found as 180 $m^2\ g^{-1}$ which is a very typical value for mesoporous graphitic carbon nitrides. However, after addition of BP, mCN/BP binary nanocomposites showed a surface area of 162 $m^2\ g^{-1}$ which in fact reveals the successful incorporation of BP into the mCN. BJH pore analysis showed that there was no observable change in the pore size of the materials following addition (bare mCN 17.2 nm, binary nanocomposite mCN/BP 17.1 nm). However, pore volume of mCN decreased from 0.70 $cm^3g^{-1}$to 0.62 cm^3g^{-1}after the incorporation of BP into mCN. This is related to the decreases in surface area after addition of BP which tells us pores of mCN were partially covered with BP.

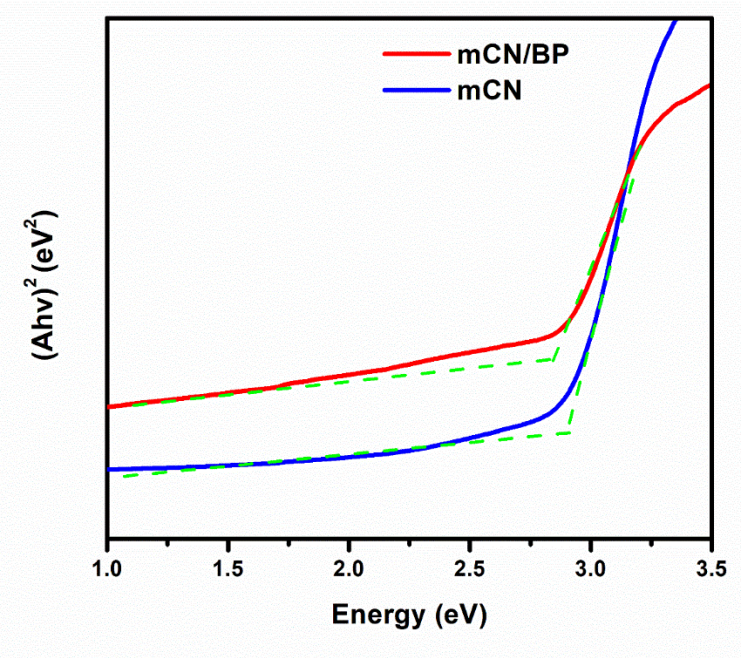

Figure 4.5: Created Tauc plots to determine band gaps from absorption data.

Charge kinetics of the synthesized materials was investigated with both steady state and time resolved PL spectroscopy. The results can be seen in Figure 4.6. As it can be seen from steady state PL spectrum, after addition of BP to mCN, there is an increase in the PL signal intensity (Figure 4.6 (a)). Even though this is not something desired, this was expected due to two reasons. First, BP and mCN forms a type I semiconductor heterojunction. This type of heterojunction is known to increase charge carrier recombination because holes and electrons are collected at one of the semiconductors thus efficient separation cannot be achieved. But this problem was handled with addition of AgPd alloy nanoparticles and it will be explained later. Second, mCN holds a relatively amorphous structure. Addition of BP which is a highly crystalline material most probably has eased the charge carrier recombination by offering an ordered recombination pathway. However, after addition of AgPd alloy nanoparticles, signal has decreased considerably. This clearly shows the suppression of charge carrier recombination. This is a result of Schottky Barrier which was formed between semiconductors (BP and mCN) and metal nanoparticles (AgPd alloy). Moreover, this barrier acts as an obstacle for the electron backflow; therefore, recombination is restricted, and PL intensities has decreased. In this case, AgPd alloy nanoparticles behave as a photoinduced electron sink that traps photoinduced electrons supplied from the irradiated mCN and BP and thus preventing the recombination with positively charged holes.

From time resolved PL spectroscopy, an estimation regarding lifetimes of photoinduced electron and hole pair can be made. Obtained lifetime plot can be seen in Figure 4.6 (b) and fitted data with both slow and fast component values can be seen in Table A.1. When data is fitted, it was seen that lifetimes of bare BP (5.1 ns) and bare mCN (7.1 ns) have dramatically improved upon hybridization to mCN/BP (7.8 ns). This is an indicator showing that even though radiative recombination is increased, lifetime of the carriers has improved. Finally, after decoration of AgPd alloy nanoparticles, there was not any significant change observed in the recombination lifetime.

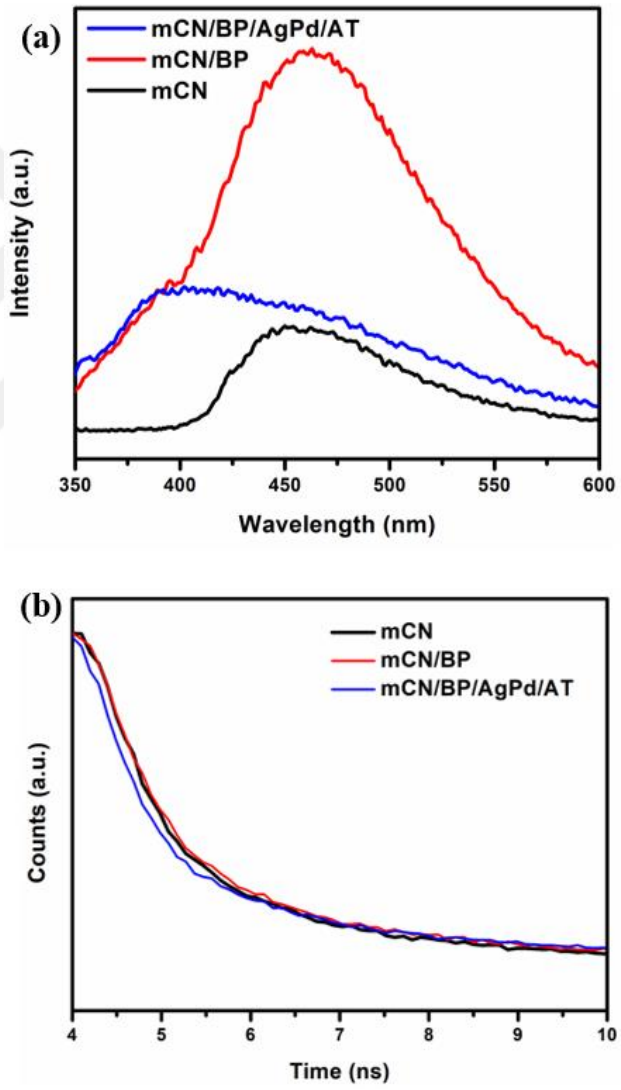

Figure 4.6: (a) Steady state and (b) time resolved photoluminescence spectroscopy data.

Fourier-transform infrared spectroscopy (FTIR) analysis was conducted on mCN/BP/AgPd and mCN/BP/AgPd/AT ternary nanocomposites to see the effect of acetic acid treatment. Obtained FTIR spectrum can be seen in Figure A.8. When spectrum is analysed, the changes on the intensities of C-H stretching bands of OAm molecules can be seen in the region from 2800 to 3000 cm^{-1}. Since there is not any other C-H functional group in the structure of ternary nanocomposite, this method is highly viable. It can be concluded by the comparison of two spectra that the intensities of C-H stretching band at 2920 cm^{-1} decreased after the acetic acid treatment. This can be considered an evidence for the stripping of most of the surfactants from the nanoparticle surface. But it should be noted that there was still some OAm presented in the structure, so it was not possible to strip all surfactants from the structure with this method.

Elemental composition analysis of AgPd alloy nanoparticles and mCN/BP/AgPd ternary nanocomposites was done through ICP-MS. In total, four AgPd alloy nanoparticles with different compositions were synthesized using same experimental setup and different metal precursor amounts. In Table 4.1, varying precursor amounts and resulting alloy nanoparticle compositions of Ag and Pd can be seen. Additionally, loading ratios of mCN/BP/AgPd and mCN/BP/AgPd/AT ternary nanocomposites were investigated. It was found that the total metal content of mCN/BP/AgPd (before acetic acid treatment) was 21.9% with a contribution from 10.4% Pd and 11.5% Ag (weight percent). For mCN/BP/AgPd/AT ternary nanocomposite (acetic acid treated), metal content was determined as 11% Pd and 13%. Total loading ratio was increased to 24.0% after acetic acid treatment. This can be explained by primarily the removal of organic surfactants and loss of some of the support material after washing.

Table 4.1: Resulting AgPd nanoparticle compositions with varying precursor amount.

	$Pd(acac)_2$ (mmol)	Ag(ac) (mmol)
$Ag_{80}Pd_{20}$	0.2	0.8
$Ag_{60}Pd_{40}$	0.25	0.75
Ag_1Pd_1	0.5	0.5
$Ag_{25}Pd_{75}$	0.75	0.25

In order to make valid assumptions about the photoinduced charge carrier movements within the photocatalyst, Valence-band X-ray photoelectron spectroscopy (VXPS) of bare mCN and BP were investigated. The results can be seen in Appendix A.9. Valance band energies of BP and mCN was determined as 0.75 eV and 1.75 eV, respectively. These results are in well agreements with the literature reports [107], [141], [142] . Based on the characterization data discussed above which are band gap and valance band energies of semiconductors obtained from conducted studies, a mechanism for the photocatalytic solvolysis of AB via mCN/BP/AgPd ternary nanocomposite under light irradiation is proposed schematically in Figure 4.7. In the synthesis, BP mostly in the form of few layer was decorated on mCN. Knowing layer dependent band gap nature of BP and characterization results along with clear literature data, this resulted with a type I heterojunction system. However, it should be noted that along few layers BP, also BP in bulk form and monolayer form are presented in the structure. But, since these structures also form a type I heterojunctions with mCN, they are ignored. In this type of heterojunctions, the semiconductor with more positive valance band and less negative conduction band positions collect photoinduced electrons and holes from the other semiconductor. It should be mentioned that synthesized AgPd alloy nanoparticles were anchored on mCN/BP unselectively, thus they are assembled on both mCN and BP. With the light irradiation, both mCN and BP get excited. Created photoinduced electrons at the conduction band of mCN flows through conduction band positions of BP and AgPd alloy nanoparticles. This new coming electrons and already excited electrons from BP species are then being transferred to d-band of AgPd alloy nanoparticles on BP surface which are considered to have lower energy than CB band of BP [24], thus making them electron rich for the reaction. Since AgPd alloy nanoparticles are decorated through the whole structure, migration of mCN conduction band electrons also happens to AgPd alloy nanoparticles. The Schottky Barrier which was formed between AgPd nanoparticles – BP and AgPd nanoparticles –mCN restricts the backflow of electrons which gives rise to an increased photocatalytic activity. In this mechanism, methanol plays an important role. While electrons are collected on AgPd alloy nanoparticles, holes migrate to lower potential valance band of BP species. In order to make reduction reaction at the conduction band possible, one needs to use holes at the valance band via an oxidation reaction as well. This is also crucial for inhibiting the charge recombination and increasing the charge separation. Methanol gets oxidized at the valance band position of

BP leads to formation of undefined methoxy species. When solvolysis reaction of AB was carried out at water instead of methanol, which is a hydrolysis reaction, via mCN/BP/AgPd, the resulting photocatalytic activity was drastically lower (TOF value of 5.3 mol H_2 mol $AgPd^{-1}$ min^{-1}) than methanol which indicates the importance of methanol in this reaction clearly. Hydrogen generation plot of hydrolysis data can be seen in Figure A.10.

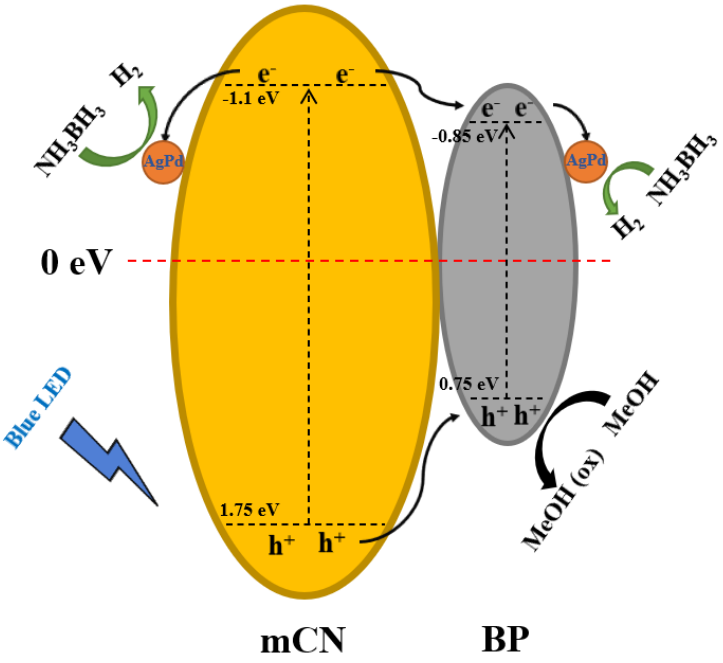

Figure 4.7: Schematic representation of the photocatalytic mechanism of mCN/BP/AgPd ternary nanocomposites with blue light irradiation.

4.2 Photocatalytic studies

Following detailed structural and compositional characterization, prepared ternary nanocomposites mCN/BP/AgPd were tested the in the solvolysis of AB (room temperature). Before continuing with extensive kinetic studies of mCN/BP/AgPd, primary optimization studies were conducted to reveal effect of reaction conditions. Optimization study results can be seen in Figure 4.8. From Figure 4.8, it can be concluded that, under ambient conditions and white light illumination, mCN/BP/AgPd ternary nanocomposite showed the highest catalytic activity with 3 moles of hydrogen evolution in 8 minutes with an initial TOF value of 23.1 mol H_2 mol $AgPd^{-1}$ min^{-1} among other catalysts which were mCN/BP/Ag ternary nanocomposite formed with only silver nanoparticles, mCN/BP/Pd ternary nanocomposite formed with only palladium

nanoparticles, and different mCN/BP/AgPd ternary nanocomposites with varying AgPd alloy nanoparticle compositions. It can be also seen that the photocatalytic activity of mCN/BP/AgPd ternary nanocomposites in general, were higher than their monometallic counterparts mCN/BP/Ag and mCN/BP/Pd, which clearly results from the synergistic effect of alloying Pd and Ag in the structure.

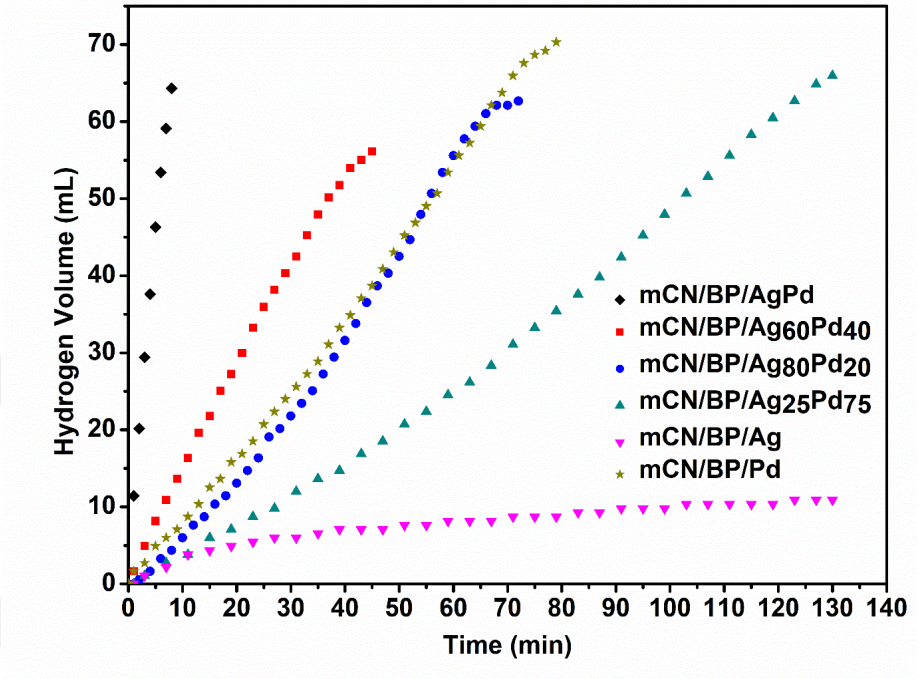

Figure 4.8: Generated hydrogen gas volume versus time during the photocatalytic methanolysis of AB with different AgPd alloy compositions and monometallic Ag and Pd nanoparticles decorated on mCN/BP.

Next, the effect of the organic surfactant stripping procedure and support material to the photocatalytic activity of ternary nanocomposites were investigated. Figure 4.9 (a) shows the results of photocatalytic activity of optimized AgPd alloy nanoparticles on different photoactive support materials of bare mCN, bare-BP, and finally binary nanocomposite mCN/BP. It can be seen that binary nanocomposite mCN/BP support showed highest photocatalytic activity when it is decorated with AgPd alloy nanoparticles. This can be explained by the formation of a beneficial heterojunction between semiconductors mCN and BP that resulted with the enhancement of the photocatalytic activity. This increased photocatalytic activity also gives the information of a successful Schottky Barrier formation at the AgPd – mCN and AgPd – BP interfaces. Moreover, it was seen that the photocatalytic activity could be further increased by

surfactant stripping. Increased activities from surface stripping can be seen in Figure 4.9 (b). Among tested treatments (annealing and acid treatment), acetic acid washing showed highest activity with a TOF value of 40.5 H_2 mol $AgPd^{-1}$ min^{-1}. As a result, mCN/BP/AgPd/AT ternary nanocomposites were selected as the optimized photocatalyst and the kinetic studies were performed this composition.

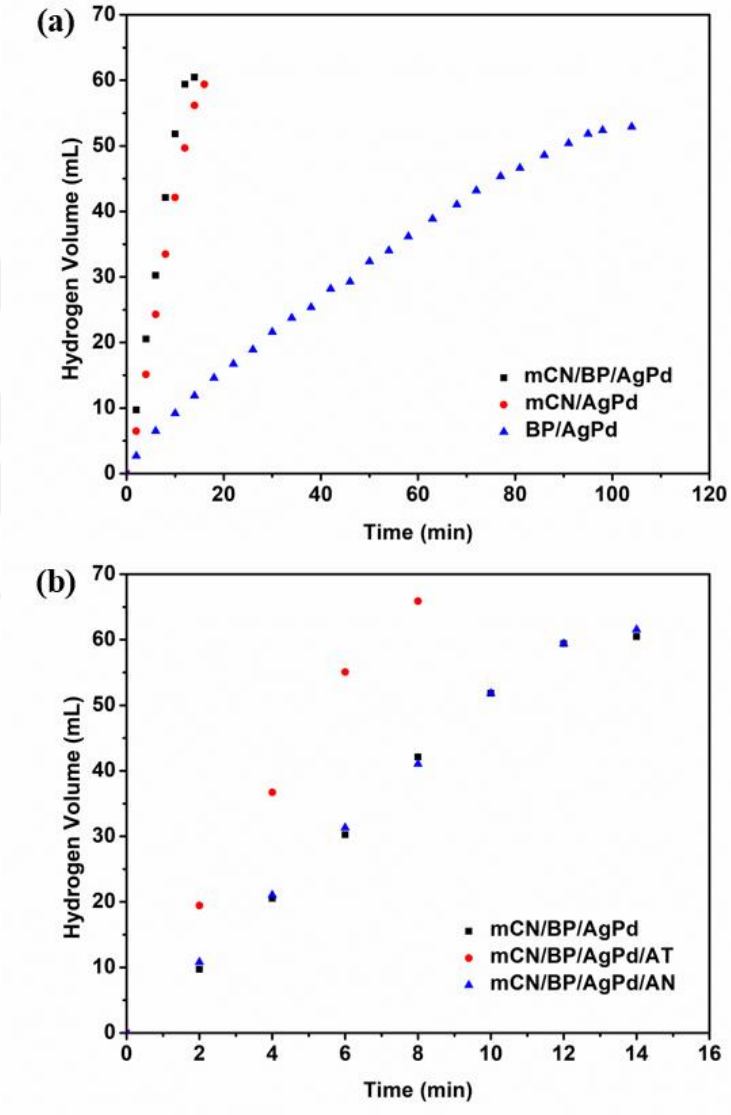

Figure 4.9: Generated hydrogen gas volume versus time during the photocatalytic methanolysis of AB with (a) AgPd alloy nanoparticles supported on three distinct supports and (b) two different cleaning treatments applied on mCN/BP/AgPd ternary nanocomposites.

Then, effect of the light source on the photocatalytic activity of mCN/BP/AgPd/AT ternary nanocomposites were investigated. The reaction was conducted with the

illumination from white light-emitting diode (LED) and blue LED and in dark conditions. The results are depicted in the Figure 4.10 (a). It can be concluded that mCN/BP/AgPd/AT ternary nanocomposites achieved highest photocatalytic activity with an initial TOF value of 43.7 H_2 mol $AgPd^{-1}$ min^{-1} with the blue LED irradiation. It should be noted that, the ternary nanocomposite also showed considerable catalytic activity without any light illumination (28.3 H_2 mol $AgPd^{-1}$ min^{-1}). This can be explained by the high independent catalytic activity of the active sites, AgPd alloy nanoparticles, in the ternary nanocomposite mCN/BP/AgPd/AT. In literature, the high catalytic activity of AgPd alloy nanoparticles in the solvolysis of AB was reported before [70], [85]. However, with blue LED irradiation, a photocatalytic activity of 1.5 times enhancement was achieved. In addition to that, the difference in the photocatalytic activity between under dark conditions and blue LED irradiation became more prominent at low temperatures (Fig. 4.10 (b)). This result might arise from photothermal effect which is thought to be occurring at the same time with photocatalytic effect. Taking these results into consideration, kinetic studies have been continued with blue LED illumination.

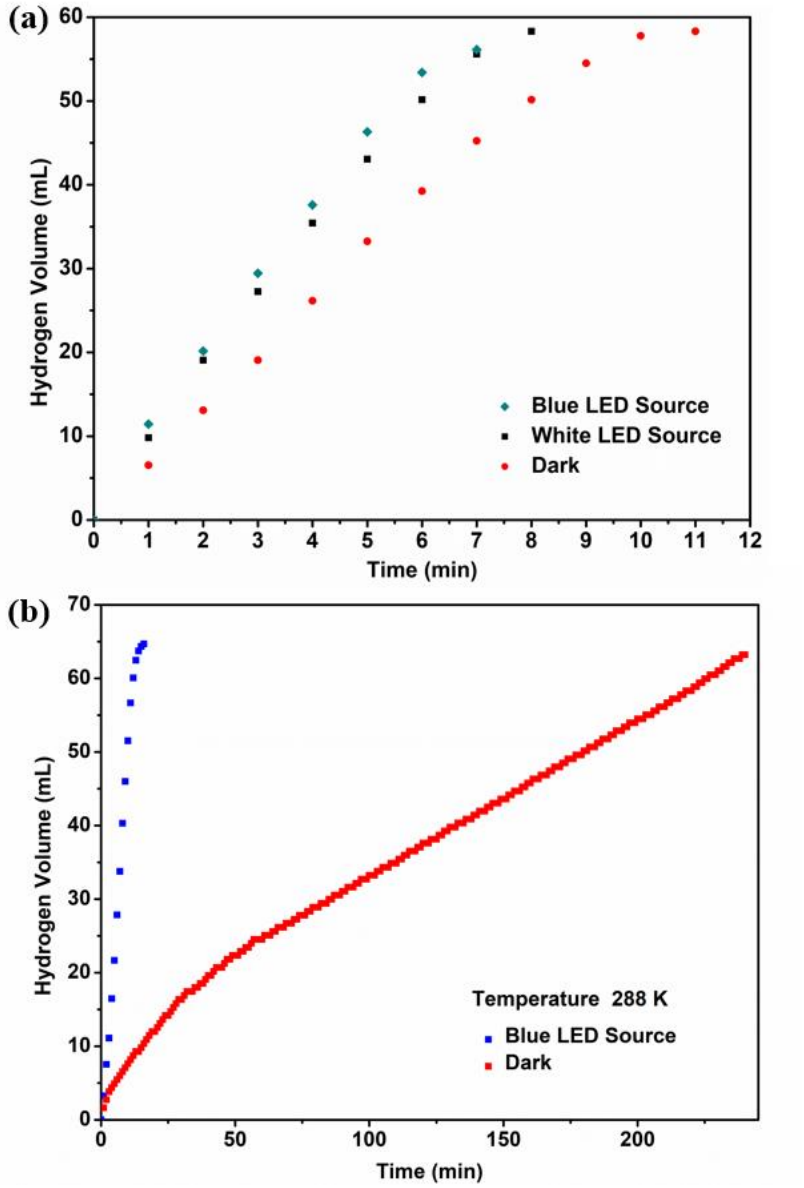

Figure 4.10: Generated hydrogen gas volume versus time during the AB methanolysis performed in the dark and under white and blue LED light illuminations at (a) 298 K and (b) 288 K.

In order to obtain activation parameters and rate law of the methanolysis reaction of AB by mCN/BP/AgPd/AT photocatalyst, the kinetics of the reaction was investigated using different concentration of catalyst and substrate and varying temperature. First, different amounts of photocatalyst (5 – 20 mg) mCN/BP/AgPd/AT was used for the methanolysis without changing AB concentration (100 mM) and temperature (298 K). Generated hydrogen volume versus time plot can be seen in Figure 4.11 (a). As it was expected, hydrogen evolution rate enhanced with increasing photocatalyst amount. For

each data, slopes of the initial portion (linear region) was selected to calculate initial rates. After taking natural logarithm of these initial rates and corresponding photocatalyst amount, Figure 4.11 (b) was created. The slope of this crated plot was calculated as 0.82, which indicated that this reaction is in fact behaves as a first order reaction with respect to photocatalyst amount. In Figure 4.11 (c), the amount of hydrogen gas against time in the methanolysis of AB, keeping photocatalyst amount and reaction temperature constant, with varying AB concentrations (50−300 mM) can be seen. Just as varying the amount of photocatalyst, slopes of the initial linear portion was selected to calculate initial rates. Figure 4.11 (d) shows the rate of hydrogen generation versus the AB concentration, both of them being in natural logarithm. Calculated slope of this plot (0.058) suggests that this reaction proceeds independently from concentration of AB.

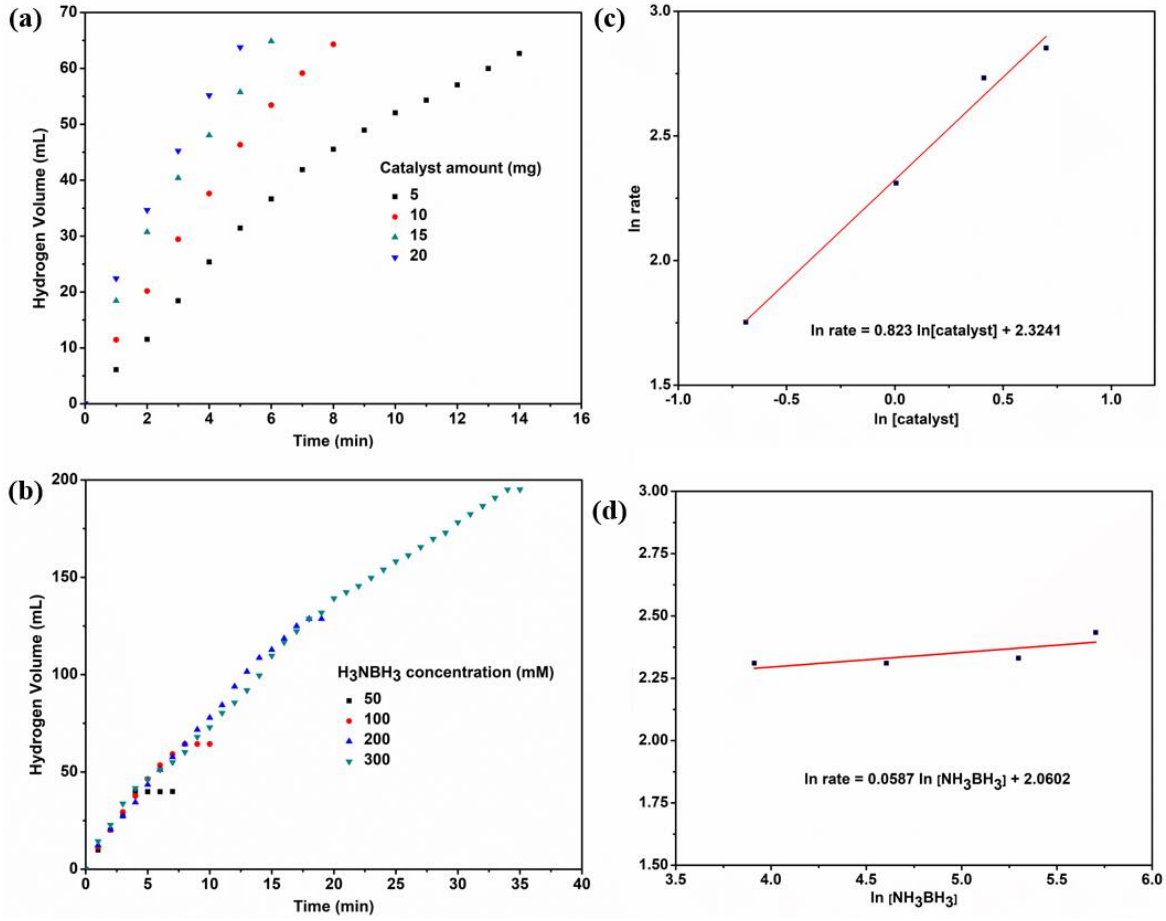

Figure 4.11: Generated hydrogen gas volume versus time during the mCN/BP/AgPd/AT catalyzed methanolysis of AB at (a) varying catalyst amounts (5−20 mg) and (b) different AB molarities (50−300 mM). Plotted ln rate versus (c) ln catalyst amount and (d) ln AB concentration graphs.

Based on performed kinetic studies, the reaction was identified zeroth order with respect to AB amount and first order with respect to photocatalyst amount. As a result, the rate law of the photocatalytic methanolysis of AB which was catalysed by mCN/BP/AgPd/AT ternary nanocomposite was conveyed as:

$$\text{Rate of the reaction} = k_{obs}[\text{catalyst}]$$

Final kinetic studies of the photocatalytic methanolysis of AB via mCN/BP/AgPd/AT ternary nanocomposite was done with varying temperatures (288 – 308 K). The results of this kinetic studies can be seen in Figure 4.12 (a). Increasing reaction temperature was resulted with increased rate of generation of hydrogen, as expected. Apparent rate constant (k^{app}) values were calculated with placing the initial rates of each experiment at different temperatures into the conveyed rate law and depicted in Figure 4.12 (b). After obtaining k^{app} for every experiment at different temperatures, the Arrhenius plot was formed with natural logarithms of k^{app} ($\ln k^{app}$) values and inverted temperature (1/T) values. Formed Arrhenius plot can be seen in Figure 4.12 (b). The apparent activation energy ($E_a{}^{app}$) of photocatalytic methanolysis of AB via mCN/BP/AgPd/AT ternary nanocomposites was calculated as 55 kJ mol^{-1} from slope of the Arrhenius plot.

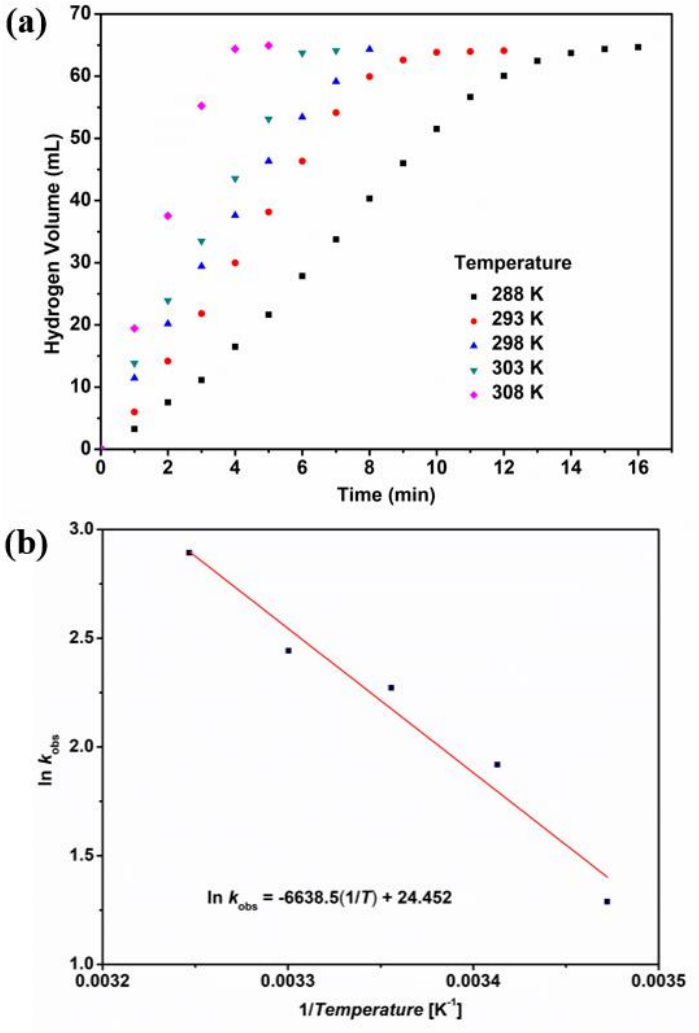

Figure 4.12: (a) Generated hydrogen gas volume versus time during the mCN/BP/AgPd/AT catalyzed methanolysis of AB at varying temperatures and (b) drawn Arrhenius plot from these results.

In order to utilize heterogeneous photocatalysts in practical applications efficiently, reusability is an important factor to consider. In this regard, the durability and reusability of the mCN/BP/AgPd/AT ternary nanocomposites were investigated by employing the catalyst in five consecutive cycles in the methanolysis of AB at room temperature. Figure 4.13 (a) shows the generated hydrogen volume against time in the methanolysis of AB via mCN/BP/AgPd/AT ternary nanocomposite in a five-run test. It can be seen from the Figure 4.13 (a) that mCN/BP/AgPd/AT ternary nanocomposites kept their initial activity up to 70% in the fifth run. TEM image of mCN/BP/AgPd/AT ternary nanocomposites after the fifth reusability test can be seen in Figure 4.13 (b). TEM image indicates that there was no agglomeration of AgPd alloy nanoparticles on the binary composite

mCN/BP. However, formation of larger nanoparticles was detected as the average particle size has increased to 4.7 nm. Particle size histogram can be seen in the Figure 4.13 (c). These enlargements most probably resulted from Ostwald ripening. On the other hand, AgPd alloy nanoparticles retained their initial shapes and morphologies. Keeping in mind that, the drop in the photocatalytic activity of mCN/BP/AgPd/AT in the reusability test did not caused by agglomeration of nanoparticles but most probably resulted from the decrease in the available surface area of the AgPd which is the catalytically active phase together with the loss of catalyst during cleaning phases.

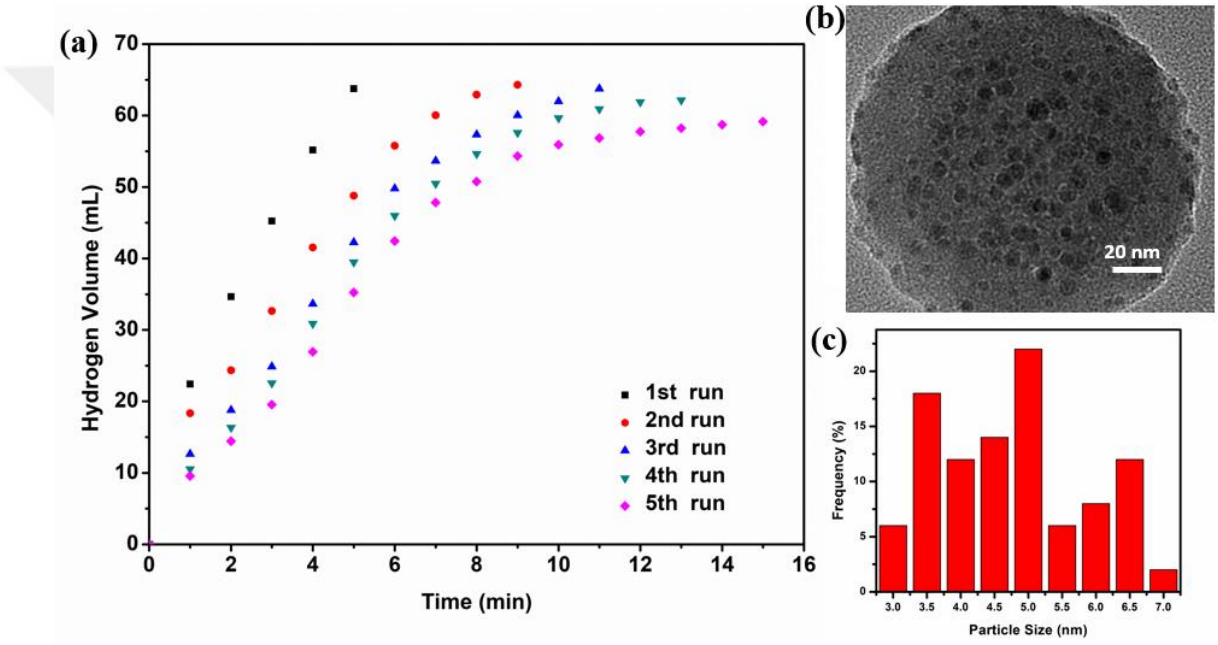

Figure 4.13: (a) Generated hydrogen gas volume versus time during the mCN/BP/AgPd/AT catalyzed methanolysis of AB throughout the five cycle reusability experiment. (b) Representative TEM image of the photocatalyst after the last cycle and (c) corresponding particle size histogram of the photocatalyst after the last run.

Chapter 5:
CONCLUSION AND FUTURE PERSPECTIVES

As a summary, semiconductor 2D materials of BP and mCN and catalytically active phase AgPd alloy nanoparticles synthesized to be utilized in the methanolysis of AB. After synthesizing the bare components, mCN/BP/AgPd ternary nanocomposites which were shown to be highly visible light active material was constructed. Detailed characterization studies revealed that addition of BP into mCN in order to create binary nanocomposites increased the lifetime of charge carriers and improved the charge kinetics. A Type I heterojunction between semiconductors and A Schottky barrier between metallic AgPd alloy nanoparticles and used semiconductor support materials were effectively formed. These resulting properties contributed to notable photocatalytic activity of mCN/BP/AgPd ternary nanocomposite in the methanolysis of AB. In order to further increase photocatalytic activity, surface organic groups were stripped with an acetic acid treatment. Moreover, photocatalytic performance of mCN/BP/AgPd ternary nanocomposite was found to be highly dependent on composition of AgPd alloy nanoparticles, ratio of BP in mCN/BP, surface cleaning method and light source. The optimized catalyst, mCN/BP/AgPd/AT showed a TOF value of 43.7 mol H_2 mol $AgPd^{-1}$ min^{-1}. According to kinetic studies, photocatalytic AB methanolysis is zeroth order in terms of concentration of AB and first order in terms of photocatalyst concentration. Moreover, using Arrhenius plot, apparent activation energy was calculated as 55 kJ mol^{-1}. Reusability of mCN/BP/AgPd/AT was tested through a five-cycle catalytic test and showed highly promising results with retaining 70% of its initial activity at the last cycle.

Taking everything into consideration, this work showed the high potential of BP in the photocatalysis applications. When BP is hybridized with appropriate semiconductors, its activity and applicability can be further increased. Formation of a semiconductor – semiconductor heterojunction and Schottky barrier contributes to increased photocatalytic activity and usage of metal nanoparticles in photocatalytic applications is a highly promising pathway. Overall, we believe that BP will be employed widely in photocatalytic applications in very near future and new areas other than energy applications such as environmental remediation and organic synthesis will be visited by BP with stability increment gained through different strategies.

BIBLIOGRAPHY

[1] N. S. Lewis and D. G. Nocera, “Powering the planet: Chemical challenges in solar energy utilization,” *Proc. Natl. Acad. Sci. U. S. A.*, vol. 103, no. 43, pp. 15729–15735, 2006.

[2] T. Nejat Veziroglu, “Conversion to hydrogen economy,” in *Energy Procedia*, 2012.

[3] L. Schlapbach and A. Züttel, “Hydrogen-storage materials for mobile applications,” 2001.

[4] A. Züttel, “Materials for hydrogen storage,” *Mater. Today*, vol. 6, no. 9, pp. 24–33, Sep. 2003.

[5] Y. Kar, N. Şen, and A. Demirbaş, “Boron minerals in turkey, their application areas and importance for the country’s economy,” *Miner. Energy - Raw Mater. Rep.*, vol. 20, no. 3–4, pp. 2–10, Mar. 2006.

[6] M. Chandra and Q. Xu, “A high-performance hydrogen generation system: Transition metal-catalyzed dissociation and hydrolysis of ammonia-borane,” *J. Power Sources*, 2006.

[7] S. D. Rassat, C. L. Aardahl, T. Autrey, and R. S. Smith, “Thermal stability of ammonia borane: A case study for exothermic hydrogen storage materials,” in *Energy and Fuels*, 2010, vol. 24, no. 4, pp. 2596–2606.

[8] U. B. Demirci, “Ammonia Borane: An Extensively Studied, Though Not Yet Implemented, Hydrogen Carrier,” *Energies*, vol. 13, no. 12, p. 3071, Jun. 2020.

[9] P. V. Ramachandran and P. D. Gagare, “Preparation of ammonia borane in high yield and purity, methanolysis, and regeneration,” *Inorg. Chem.*, vol. 46, no. 19, pp. 7810–7817, Sep. 2007.

[10] C. T. F. Lo, K. Karan, and B. R. Davis, “Kinetic studies of reaction between sodium borohydride and methanol, water, and their mixtures,” *Ind. Eng. Chem. Res.*, vol. 46, no. 17, pp. 5478–5484, Aug. 2007.

[11] Y. M. Hunge, “Basics and advanced developments in photocatalysis – a review (Mini review),” *Int. J. Hydrol.*, vol. 2, no. 4, pp. 539–540, 2018.

[12] A. Fujishima and K. Honda, “Electrochemical photolysis of water at a semiconductor electrode,” *Nature*, vol. 238, no. 5358, pp. 37–38, 1972.

[13] T. Sakthivel, X. Huang, Y. Wu, and S. Rtimi, “Recent progress in black

phosphorus nanostructures as environmental photocatalysts," *Chem. Eng. J.*, vol. 379, no. April 2019, p. 122297, 2020.

[14] Y. Chen *et al.*, "Visible-light responsive organic nano-heterostructured photocatalysts for environmental remediation and H2 generation," *J. Mater. Sci. Technol.*, vol. 38, pp. 93–106, 2020.

[15] G. Guan, E. Ye, M. You, and Z. Li, "Hybridized 2D Nanomaterials Toward Highly Efficient Photocatalysis for Degrading Pollutants: Current Status and Future Perspectives," *Small*, p. 1907087, Apr. 2020.

[16] A. Di Paola, E. García-López, G. Marcì, and L. Palmisano, "A survey of photocatalytic materials for environmental remediation," *J. Hazard. Mater.*, vol. 211–212, pp. 3–29, 2012.

[17] M. M. Khin, A. S. Nair, V. J. Babu, R. Murugan, and S. Ramakrishna, "A review on nanomaterials for environmental remediation," *Energy Environ. Sci.*, vol. 5, no. 8, pp. 8075–8109, 2012.

[18] R. Ahmad, Z. Ahmad, A. U. Khan, N. R. Mastoi, M. Aslam, and J. Kim, "Photocatalytic systems as an advanced environmental remediation: Recent developments, limitations and new avenues for applications," *J. Environ. Chem. Eng.*, vol. 4, no. 4, pp. 4143–4164, 2016.

[19] K. S. Novoselov *et al.*, "Electric field in atomically thin carbon films," *Science (80-.).*, vol. 306, no. 5696, pp. 666–669, Oct. 2004.

[20] D. D. L. Chung, "Review: Graphite," *J. Mater. Sci.*, vol. 37, no. 8, pp. 1475–1489, 2002.

[21] A. H. Castro Neto, F. Guinea, N. M. R. Peres, K. S. Novoselov, and A. K. Geim, "The electronic properties of graphene," *Rev. Mod. Phys.*, vol. 81, no. 1, pp. 109–162, Jan. 2009.

[22] H. Jin *et al.*, "Emerging Two-Dimensional Nanomaterials for Electrocatalysis," *Chem. Rev.*, vol. 118, no. 13, pp. 6337–6408, 2018.

[23] J. Low, J. Yu, M. Jaroniec, S. Wageh, and A. A. Al-Ghamdi, "Heterojunction Photocatalysts," *Adv. Mater.*, vol. 29, no. 20, 2017.

[24] X. Zhang, Y. L. Chen, R. S. Liu, and D. P. Tsai, "Plasmonic photocatalysis," *Reports Prog. Phys.*, vol. 76, no. 4, 2013.

[25] S. P. Sun, S. Gu, J. H. Sun, F. F. Xia, and G. H. Chen, "First principles investigation of the electronic properties of graphitic carbon nitride with different building block

and sheet staggered arrangement," *J. Alloys Compd.*, 2018.

[26] A. Sudhaik, P. Raizada, P. Shandilya, D. Y. Jeong, J. H. Lim, and P. Singh, "Review on fabrication of graphitic carbon nitride based efficient nanocomposites for photodegradation of aqueous phase organic pollutants," *Journal of Industrial and Engineering Chemistry*. 2018.

[27] P. Qiu, C. Xu, N. Zhou, H. Chen, and F. Jiang, "Metal-free black phosphorus nanosheets-decorated graphitic carbon nitride nanosheets with C[sbnd]P bonds for excellent photocatalytic nitrogen fixation," *Appl. Catal. B Environ.*, 2018.

[28] Y. Zheng, Z. Yu, H. Ou, A. M. Asiri, Y. Chen, and X. Wang, "Black Phosphorus and Polymeric Carbon Nitride Heterostructure for Photoinduced Molecular Oxygen Activation," *Adv. Funct. Mater.*, vol. 28, no. 10, Mar. 2018.

[29] Y. Luo, Y. Yan, S. Zheng, H. Xue, and H. Pang, "Graphitic carbon nitride based materials for electrochemical energy storage," *J. Mater. Chem. A*, vol. 7, no. 3, pp. 901–924, 2019.

[30] X. Ling, H. Wang, S. Huang, F. Xia, and M. S. Dresselhaus, "The renaissance of black phosphorus," *Proceedings of the National Academy of Sciences of the United States of America*, vol. 112, no. 15. National Academy of Sciences, pp. 4523–4530, 14-Apr-2015.

[31] B. Li *et al.*, "Black Phosphorus, a Rising Star 2D Nanomaterial in the Post-Graphene Era: Synthesis, Properties, Modifications, and Photocatalysis Applications," *Small*, vol. 15, no. 8. Wiley-VCH Verlag, 22-Feb-2019.

[32] L. Li *et al.*, "Black phosphorus field-effect transistors," *Nat. Nanotechnol.*, vol. 9, no. 5, pp. 372–377, 2014.

[33] P. W. Bridgman, "Two new modifications of phosphorus," *J. Am. Chem. Soc.*, vol. 36, no. 7, pp. 1344–1363, Jul. 1914.

[34] A. J. Mannix, B. Kiraly, M. C. Hersam, and N. P. Guisinger, "Synthesis and chemistry of elemental 2D materials," *Nat. Rev. Chem.*, vol. 1, pp. 1–15, 2017.

[35] H. Du, X. Lin, Z. Xu, and D. Chu, "Recent developments in black phosphorus transistors," *J. Mater. Chem. C*, vol. 3, no. 34, pp. 8760–8775, 2015.

[36] S. Lange, P. Schmidt, and T. Nilges, "Au3SnP7@Black Phosphorus: An easy access to black phosphorus," *Inorg. Chem.*, vol. 46, no. 10, pp. 4028–4035, May 2007.

[37] L. Bai *et al.*, "Black Phosphorus/Platinum Heterostructure: A Highly Efficient

Photocatalyst for Solar-Driven Chemical Reactions," *Adv. Mater.*, vol. 30, no. 40, Oct. 2018.

[38] A. Favron *et al.*, "Photooxidation and quantum confinement effects in exfoliated black phosphorus," *Nat. Mater.*, vol. 14, no. 8, pp. 826–832, Aug. 2015.

[39] A. Castellanos-Gomez *et al.*, "Isolation and characterization of few-layer black phosphorus," *2D Mater.*, vol. 1, no. 2, Sep. 2014.

[40] M. Zhu, C. Zhai, M. Fujitsuka, and T. Majima, "Noble metal-free near-infrared-driven photocatalyst for hydrogen production based on 2D hybrid of black Phosphorus/WS2," *Appl. Catal. B Environ.*, vol. 221, pp. 645–651, 2018.

[41] M. Li, N. Muralidharan, K. Moyer, and C. L. Pint, "Solvent mediated hybrid 2D materials: Black phosphorus-graphene heterostructured building blocks assembled for sodium ion batteries," *Nanoscale*, vol. 10, no. 22, pp. 10443–10449, Jun. 2018.

[42] F. Liu, R. Shi, Z. Wang, Y. Weng, C. Che, and Y. Chen, "Direct Z-Scheme Hetero-phase Junction of Black/Red Phosphorus for Photocatalytic Water Splitting," *Angew. Chemie*, p. ange.201906416, Jul. 2019.

[43] M. Zhu *et al.*, "Metal-Free Photocatalyst for H2Evolution in Visible to Near-Infrared Region: Black Phosphorus/Graphitic Carbon Nitride," *J. Am. Chem. Soc.*, vol. 139, no. 37, pp. 13234–13242, 2017.

[44] B. Schmidt and D. Geißler, "Ru- and Pd-catalysed synthesis of 2-arylfurans by one-flask heck arylation/oxidation," *European J. Org. Chem.*, no. 25, pp. 4814–4822, Sep. 2011.

[45] K. J. Klabunde *et al.*, "Nanocrystals as stoichiometric reagents with unique surface chemistry," *J. Phys. Chem.*, vol. 100, no. 30, pp. 12142–12153, 1996.

[46] V. Selvamani, "Stability Studies on Nanomaterials Used in Drugs," in *Characterization and Biology of Nanomaterials for Drug Delivery: Nanoscience and Nanotechnology in Drug Delivery*, Elsevier, 2018, pp. 425–444.

[47] A. Rudin and P. Choi, "Dispersion and Emulsion Polymerizations," in *The Elements of Polymer Science & Engineering*, Elsevier, 2013, pp. 427–447.

[48] T. Dang-Bao, D. Pla, I. Favier, and M. Gómez, "Bimetallic nanoparticles in alternative solvents for catalytic purposes," *Catalysts*, vol. 7, no. 7, 2017.

[49] K. D. Gilroy, A. Ruditskiy, H. C. Peng, D. Qin, and Y. Xia, "Bimetallic nanocrystals: Syntheses, properties, and applications," *Chem. Rev.*, vol. 116, no. 18, pp. 10414–10472, 2016.

[50] T. Balkan, H. Küçükkeçeci, H. Zarenezhad, S. Kaya, and Ö. Metin, "One-pot synthesis of monodisperse copper–silver alloy nanoparticles and their composition-dependent electrocatalytic activity for oxygen reduction reaction," *J. Alloys Compd.*, vol. 831, 2020.

[51] M. Ahlers, "The Hume-Rothery rules and phase stabilities in noble metal alloys," *Zeitschrift für Phys. B Condens. Matter*, vol. 99, no. 1, pp. 491–499, 1995.

[52] R. Evans, P. Lloyd, and Rahman Mujibur, "On the origin of the Hume-Rothery rules for phase stability in α and β brasses," *J. Phys. F Met. Phys.*, vol. 9, no. 10, pp. 1939–1960, 1979.

[53] D. Wu, K. Kusada, and H. Kitagawa, "Recent progress in the structure control of Pd–Ru bimetallic nanomaterials," *Sci. Technol. Adv. Mater.*, vol. 17, no. 1, pp. 583–596, 2016.

[54] Q. Lai *et al.*, "Hydrogen Storage Materials for Mobile and Stationary Applications: Current State of the Art," *ChemSusChem*, vol. 8, no. 17. Wiley-VCH Verlag, pp. 2789–2825, 01-Sep-2015.

[55] A. J. Huckaba *et al.*, " Low-Cost TiS 2 as Hole-Transport Material for Perovskite Solar Cells ," *Small Methods*, vol. 1, no. 10, p. 1700250, 2017.

[56] Y. Liu and H. Pan, "Hydrogen Storage Materials," in *New and Future Developments in Catalysis: Batteries, Hydrogen Storage and Fuel Cells*, Elsevier B.V., 2013, pp. 377–405.

[57] M. Chandra and Q. Xu, "A high-performance hydrogen generation system: Transition metal-catalyzed dissociation and hydrolysis of ammonia-borane," *J. Power Sources*, vol. 156, no. 2, pp. 190–194, Jun. 2006.

[58] Ö. Metin, V. Mazumder, S. Özkar, and S. Sun, "Monodisperse nickel nanoparticles and their catalysis in hydrolytic dehydrogenation of ammonia borane," *J. Am. Chem. Soc.*, vol. 132, no. 5, pp. 1468–1469, Feb. 2010.

[59] S. Akbayrak and S. Özkar, "Ammonia borane as hydrogen storage materials," *Int. J. Hydrogen Energy*, vol. 43, no. 40, pp. 18592–18606, Oct. 2018.

[60] P. V. Ramachandran and P. D. Gagare, "Preparation of ammonia borane in high yield and purity, methanolysis, and regeneration," *Inorg. Chem.*, vol. 46, no. 19, pp. 7810–7817, Sep. 2007.

[61] S. B. Kalidindi, U. Sanyal, and B. R. Jagirdar, "Nanostructured Cu and Cu@Cu2O core shell catalysts for hydrogen generation from ammonia-borane," *Phys. Chem.*

Chem. Phys., vol. 10, no. 38, pp. 5870–5874, Sep. 2008.

[62] H. Erdoğan, Ö. Metin, and S. Özkar, "In situ-generated PVP-stabilized palladium(0) nanocluster catalyst in hydrogen generation from the methanolysis of ammonia-borane," *Phys. Chem. Chem. Phys.*, vol. 11, no. 44, pp. 10519–10525, Nov. 2009.

[63] S. Çalişkan, M. Zahmakiran, and S. Özkar, "Zeolite confined rhodium(0) nanoclusters as highly active, reusable, and long-lived catalyst in the methanolysis of ammonia-borane," *Appl. Catal. B Environ.*, vol. 93, no. 3–4, pp. 387–394, Jan. 2010.

[64] H. Erdoan, Ö. Metin, and S. Özkar, "Hydrogen generation from the methanolysis of ammonia borane catalyzed by in situ generated, polymer stabilized ruthenium(0) nanoclusters," *Catal. Today*, vol. 170, no. 1, pp. 93–98, Jul. 2011.

[65] D. Sun, V. Mazumder, Ö. Metin, and S. Sun, "Methanolysis of ammonia borane by Copd nanoparticles," *ACS Catal.*, vol. 2, no. 6, pp. 1290–1295, Jun. 2012.

[66] D. Sun, P. Li, B. Yang, Y. Xu, J. Huang, and Q. Li, "Monodisperse AgPd alloy nanoparticles as a highly active catalyst towards the methanolysis of ammonia borane for hydrogen generation," *RSC Adv.*, vol. 6, no. 107, pp. 105940–105947, Nov. 2016.

[67] Z. Lou, Q. Gu, L. Xu, Y. Liao, and C. Xue, "Surfactant-Free Synthesis of Plasmonic Tungsten Oxide Nanowires with Visible-Light-Enhanced Hydrogen Generation from Ammonia Borane," *Chem. - An Asian J.*, vol. 10, no. 6, pp. 1291–1294, Jun. 2015.

[68] L. T. Guo *et al.*, "Multifunctional Au-Co@CN Nanocatalyst for Highly Efficient Hydrolysis of Ammonia Borane," *ACS Catal.*, vol. 5, no. 1, pp. 388–392, Jan. 2015.

[69] P. Verma, Y. Kuwahara, K. Mori, and H. Yamashita, "Enhancement of Ag-Based Plasmonic Photocatalysis in Hydrogen Production from Ammonia Borane by the Assistance of Single-Site Ti-Oxide Moieties within a Silica Framework," *Chem. - A Eur. J.*, vol. 23, no. 15, pp. 3616–3622, Mar. 2017.

[70] D. Sun, P. Li, B. Yang, Y. Xu, J. Huang, and Q. Li, "Monodisperse AgPd alloy nanoparticles as a highly active catalyst towards the methanolysis of ammonia borane for hydrogen generation," *RSC Adv.*, vol. 6, no. 107, pp. 105940–105947, Nov. 2016.

[71] X. Zhou, Y. Huang, W. Xing, C. Liu, J. Liao, and T. Lu, “High-quality hydrogen from the catalyzed decomposition of formic acid by Pd-Au/C and Pd-Ag/C,” *Chem. Commun.*, no. 30, pp. 3540–3542, 2008.

[72] S. Zhang, Ö. Metin, D. Su, and S. Sun, “Monodisperse AgPd alloy nanoparticles and their superior catalysis for the dehydrogenation of formic acid,” *Angew. Chemie - Int. Ed.*, vol. 52, no. 13, pp. 3681–3684, Mar. 2013.

[73] J. Liebig, “Uber einige Stickstoff - Verbindungen,” *Ann. der Pharm.*, vol. 10, no. 1, pp. 1–47, Jan. 1834.

[74] A. Y. Liu and M. L. Cohen, “Prediction of new low compressibility solids,” *Science (80-.).*, vol. 245, no. 4920, pp. 841–842, 1989.

[75] J. Ortega and O. F. Sankey, “Relative stability of hexagonal and planar structures of hypothetical C3N4 solids,” *Phys. Rev. B*, vol. 51, no. 4, pp. 2624–2627, Jan. 1995.

[76] Y. Kofuji *et al.*, “Carbon Nitride-Aromatic Diimide-Graphene Nanohybrids: Metal-Free Photocatalysts for Solar-to-Hydrogen Peroxide Energy Conversion with 0.2% Efficiency.,” *J. Am. Chem. Soc.*, vol. 138, no. 31, pp. 10019–25, 2016.

[77] A. Thomas *et al.*, “Graphitic carbon nitride materials: Variation of structure and morphology and their use as metal-free catalysts,” *J. Mater. Chem.*, vol. 18, no. 41, pp. 4893–4908, 2008.

[78] A. Thomas *et al.*, “Graphitic carbon nitride materials: Variation of structure and morphology and their use as metal-free catalysts,” *J. Mater. Chem.*, vol. 18, no. 41, pp. 4893–4908, 2008.

[79] X. Wang *et al.*, “A metal-free polymeric photocatalyst for hydrogen production from water under visible light,” *Nat. Mater.*, vol. 8, no. 1, pp. 76–80, 2009.

[80] J. Zhu, Y. Wei, W. Chen, Z. Zhao, and A. Thomas, “Graphitic carbon nitride as a metal-free catalyst for NO decomposition,” *Chem. Commun.*, vol. 46, no. 37, pp. 6965–6967, Oct. 2010.

[81] A. S. Review, “Graphitic Carbon Nitride Materials for Photocatalytic Hydrogen Production via Water Splitting : A Short Review,” 2019.

[82] W. J. Ong, L. L. Tan, Y. H. Ng, S. T. Yong, and S. P. Chai, “Graphitic Carbon Nitride (g-C3N4)-Based Photocatalysts for Artificial Photosynthesis and Environmental Remediation: Are We a Step Closer to Achieving Sustainability?,” *Chem. Rev.*, vol. 116, no. 12, pp. 7159–7329, 2016.

[83] M. Shen *et al.*, “Carbon-vacancy modified graphitic carbon nitride: Enhanced CO 2 photocatalytic reduction performance and mechanism probing,” *J. Mater. Chem. A*, vol. 7, no. 4, pp. 1556–1563, Jan. 2019.

[84] X. H. Li, X. Wang, and M. Antonietti, “Mesoporous g-C 3N 4 nanorods as multifunctional supports of ultrafine metal nanoparticles: Hydrogen generation from water and reduction of nitrophenol with tandem catalysis in one step,” *Chem. Sci.*, vol. 3, no. 6, pp. 2170–2174, Jun. 2012.

[85] H. Kahri, M. Sevim, and Ö. Metin, “Enhanced catalytic activity of monodispersed AgPd alloy nanoparticles assembled on mesoporous graphitic carbon nitride for the hydrolytic dehydrogenation of ammonia borane under sunlight,” *Nano Res.*, vol. 10, no. 5, pp. 1627–1640, May 2017.

[86] R. B. Jacobs, “Phosphorus at High Temperatures and Pressures,” *J. Chem. Phys.*, vol. 5, no. 12, pp. 945–953, 1937.

[87] R. W. Keyes, “The electrical properties of black phosphorus,” *Phys. Rev.*, vol. 92, no. 3, pp. 580–584, 1953.

[88] P. W. Bridgman, “Shearing Phenomena at High Pressures, Particularly in Inorganic Compounds,” *Proc. Am. Acad. Arts Sci.*, vol. 71, no. 9, p. 387, 1937.

[89] H. Krebs, H. Weitz, and K. H. Worms, “Über die Struktur und Eigenschaften der Halbmetalle. VIII. Die katalytische Darstellung des schwarzen Phosphors,” *Zeitschrift für Anorg. und Allg. Chemie*, vol. 280, no. 1–3, pp. 119–133, Aug. 1955.

[90] A. Brown and S. Rundqvist, “Refinement of the crystal structure of black phosphorus,” *Acta Crystallogr.*, vol. 19, no. 4, pp. 684–685, Oct. 1965.

[91] Y. Maruyama, S. Suzuki, K. Kobayashi, and S. Tanuma, “Synthesis and some properties of black phosphorus single crystals,” *Phys. B+C*, vol. 105, no. 1–3, pp. 99–102, 1981.

[92] M. Köpf *et al.*, “Access and in situ growth of phosphorene-precursor black phosphorus,” *J. Cryst. Growth*, vol. 405, pp. 6–10, 2014.

[93] D. Wang *et al.*, “Revisiting the growth of black phosphorus in Sn-I assisted reactions,” *Front. Chem.*, vol. 7, no. JAN, p. 21, Jan. 2019.

[94] G. Zhao, T. Wang, Y. Shao, Y. Wu, B. Huang, and X. Hao, “A Novel Mild Phase-Transition to Prepare Black Phosphorus Nanosheets with Excellent Energy Applications,” *Small*, vol. 13, no. 7, pp. 1–7, 2017.

[95] B. Tian *et al.*, “Facile bottom-up synthesis of partially oxidized black phosphorus

nanosheets as metal-free photocatalyst for hydrogen evolution," *Proc. Natl. Acad. Sci. U. S. A.*, vol. 115, no. 17, pp. 4345–4350, 2018.

[96] S. Zhu, Q. Liang, Y. Xu, H. Fu, and X. Xiao, "Facile Solvothermal Synthesis of Black Phosphorus Nanosheets from Red Phosphorus for Efficient Photocatalytic Hydrogen Evolution," *Eur. J. Inorg. Chem.*, vol. 2020, no. 9, pp. 773–779, 2020.

[97] A. Ozawa, M. Yamamoto, T. Tanabe, S. Hosokawa, and T. Yoshida, "Black phosphorus synthesized by solvothermal reaction from red phosphorus and its catalytic activity for water splitting," *J. Mater. Chem. A*, 2020.

[98] Y. Wang *et al.*, "Low-Temperature Solution Synthesis of Black Phosphorus from Red Phosphorus: Crystallization Mechanism and Lithium Ion Battery Applications," *J. Phys. Chem. Lett.*, pp. 2708–2716, Mar. 2020.

[99] H. Wang, X. Zhang, and Y. Xie, "Photocatalysis in Two-Dimensional Black Phosphorus: The Roles of Many-Body Effects," *ACS Nano*, vol. 12, pp. 9648–9653, 2018.

[100] H. Liu *et al.*, "Phosphorene: An unexplored 2D semiconductor with a high hole mobility," *ACS Nano*, vol. 8, no. 4, pp. 4033–4041, 2014.

[101] D. Hanlon *et al.*, "Liquid exfoliation of solvent-stabilized few-layer black phosphorus for applications beyond electronics," *Nat. Commun.*, vol. 6, 2015.

[102] J. Kang *et al.*, "Solvent exfoliation of electronic-grade, two-dimensional black phosphorus," *ACS Nano*, vol. 9, no. 4, pp. 3596–3604, Apr. 2015.

[103] S. Wu, K. S. Hui, and K. N. Hui, "2D Black Phosphorus: from Preparation to Applications for Electrochemical Energy Storage," *Adv. Sci.*, vol. 5, no. 5, p. 1700491, May 2018.

[104] J. B. Smith, D. Hagaman, and H. F. Ji, "Growth of 2D black phosphorus film from chemical vapor deposition," *Nanotechnology*, vol. 27, no. 21, pp. 1–8, 2016.

[105] S. K. Muduli *et al.*, "Evolution of hydrogen by few-layered black phosphorus under visible illumination," *J. Mater. Chem. A*, vol. 5, no. 47, pp. 24874–24879, Dec. 2017.

[106] X. Zhu *et al.*, "Black Phosphorus Revisited: A Missing Metal-Free Elemental Photocatalyst for Visible Light Hydrogen Evolution," *Adv. Mater.*, vol. 29, no. 17, May 2017.

[107] M. Zhu, C. Zhai, M. Fujitsuka, and T. Majima, "Noble metal-free near-infrared-driven photocatalyst for hydrogen production based on 2D hybrid of black

Phosphorus/WS2," *Appl. Catal. B Environ.*, vol. 221, pp. 645–651, Feb. 2018.

[108] H. Uk Lee *et al.*, "Stable semiconductor black phosphorus (BP)@titanium dioxide (TiO2) hybrid photocatalysts," *Sci. Rep.*, vol. 5, no. 1, pp. 1–6, Mar. 2015.

[109] X. Zhu *et al.*, "In-situ hydroxyl modification of monolayer black phosphorus for stable photocatalytic carbon dioxide conversion," *Appl. Catal. B Environ.*, vol. 269, p. 118760, Jul. 2020.

[110] E. Kalay, H. Küçükkeçeci, H. Kilic, and O. Metin, "Black Phosphorous as a Metal-Free, Visible-Light-Active Heterogeneous Photoredox Catalyst for the Direct C-H Arylation of Heteroarenes," *Chem. Commun.*, 2020.

[111] R. He *et al.*, "Molybdenum Disulfide-Black Phosphorus Hybrid Nanosheets as a Superior Catalyst for Electrochemical Hydrogen Evolution," *Nano Lett.*, vol. 17, no. 7, pp. 4311–4316, Jul. 2017.

[112] Y. Chang *et al.*, "Liquid-exfoliation of S-doped black phosphorus nanosheets for enhanced oxygen evolution catalysis," *Nanotechnology*, vol. 30, no. 3, p. 035701, Nov. 2019.

[113] T. Wu, J. Fan, Q. Li, P. Shi, Q. Xu, and Y. Min, "Palladium Nanoparticles Anchored on Anatase Titanium Dioxide-Black Phosphorus Hybrids with Heterointerfaces: Highly Electroactive and Durable Catalysts for Ethanol Electrooxidation," *Adv. Energy Mater.*, vol. 8, no. 1, Jan. 2018.

[114] Q. Li *et al.*, "Zinc oxide-black phosphorus composites for ultrasensitive nitrogen dioxide sensing," *Nanoscale Horizons*, vol. 3, no. 5, pp. 525–531, Sep. 2018.

[115] M. Li, N. Muralidharan, K. Moyer, and C. L. Pint, "Solvent mediated hybrid 2D materials: Black phosphorus-graphene heterostructured building blocks assembled for sodium ion batteries," *Nanoscale*, vol. 10, no. 22, pp. 10443–10449, Jun. 2018.

[116] Y. Zheng, Z. Yu, H. Ou, A. M. Asiri, Y. Chen, and X. Wang, "Black Phosphorus and Polymeric Carbon Nitride Heterostructure for Photoinduced Molecular Oxygen Activation," *Adv. Funct. Mater.*, vol. 28, no. 10, Mar. 2018.

[117] J. Ran, W. Guo, H. Wang, B. Zhu, J. Yu, and S. Z. Qiao, "Metal-Free 2D/2D Phosphorene/g-C3N4 Van der Waals Heterojunction for Highly Enhanced Visible-Light Photocatalytic H2 Production," *Adv. Mater.*, vol. 30, no. 25, Jun. 2018.

[118] M. Wen *et al.*, "A Low-Cost Metal-Free Photocatalyst Based on Black Phosphorus," *Adv. Sci.*, vol. 6, no. 1, p. 1801321, Jan. 2019.

[119] L. Kong *et al.*, "g-C_3N_4 Loading Black Phosphorus Quantum Dot for Efficient

and Stable Photocatalytic H $_2$ Generation under Visible Light," *Adv. Funct. Mater.*, vol. 28, no. 22, p. 1800668, May 2018.

[120] T. Song *et al.*, "3D reticulated carbon nitride materials high-uniformly capture 0D black phosphorus as 3D/0D composites for stable and efficient photocatalytic hydrogen evolution," *J. Mater. Chem. A*, vol. 7, no. 2, pp. 503–512, Jan. 2019.

[121] X. Chen *et al.*, "Ordered mesoporous SBA-15 type graphitic carbon nitride: A semiconductor host structure for photocatalytic hydrogen evolution-with visible light," *Chem. Mater.*, vol. 21, no. 18, pp. 4093–4095, Sep. 2009.

[122] L. Wang, C. Wang, X. Hu, H. Xue, and H. Pang, "Metal/Graphitic Carbon Nitride Composites: Synthesis, Structures, and Applications," *Chem. - An Asian J.*, vol. 11, no. 23, pp. 3305–3328, Dec. 2016.

[123] Y. Yang *et al.*, "Preparation and enhanced visible-light photocatalytic activity of silver deposited graphitic carbon nitride plasmonic photocatalyst," *Appl. Catal. B Environ.*, vol. 142–143, pp. 828–837, Oct. 2013.

[124] F. Dong, Z. Zhao, Y. Sun, Y. Zhang, S. Yan, and Z. Wu, "An Advanced Semimetal-Organic Bi Spheres-g-C3N4 Nanohybrid with SPR-Enhanced Visible-Light Photocatalytic Performance for NO Purification," *Environ. Sci. Technol.*, vol. 49, no. 20, pp. 12432–12440, Oct. 2015.

[125] S. Samanta, S. Martha, and K. Parida, "Facile Synthesis of Au/g-C $_3$ N $_4$ Nanocomposites: An Inorganic/Organic Hybrid Plasmonic Photocatalyst with Enhanced Hydrogen Gas Evolution Under Visible-Light Irradiation," *ChemCatChem*, vol. 6, no. 5, p. n/a-n/a, Mar. 2014.

[126] M. Aksoy and Ö. Metin, "Pt Nanoparticles Supported on Mesoporous Graphitic Carbon Nitride as Catalysts for Hydrolytic Dehydrogenation of Ammonia Borane," *ACS Appl. Nano Mater.*, Jun. 2020.

[127] L. Bi, D. Xu, L. Zhang, Y. Lin, D. Wang, and T. Xie, "Metal Ni-loaded g-C3N4 for enhanced photocatalytic H2 evolution activity: The change in surface band bending," *Phys. Chem. Chem. Phys.*, vol. 17, no. 44, pp. 29899–29905, Nov. 2015.

[128] H. Kahri, M. Sevim, and Ö. Metin, "Enhanced catalytic activity of monodispersed AgPd alloy nanoparticles assembled on mesoporous graphitic carbon nitride for the hydrolytic dehydrogenation of ammonia borane under sunlight," *Nano Res.*, vol. 10, no. 5, pp. 1627–1640, May 2017.

[129] H. Huang *et al.*, "Black phosphorus: a two-dimensional reductant for in situ

nanofabrication," *npj 2D Mater. Appl.*, vol. 1, no. 1, p. 20, Dec. 2017.

[130] Y. Peng *et al.*, "Oxygen Reduction Reaction Catalyzed by Black-Phosphorus-Supported Metal Nanoparticles: Impacts of Interfacial Charge Transfer," *ACS Appl. Mater. Interfaces*, vol. 11, no. 27, pp. 24707–24714, Jul. 2019.

[131] W. Lei, T. Zhang, P. Liu, J. A. Rodriguez, G. Liu, and M. Liu, "Bandgap- and Local Field-Dependent Photoactivity of Ag/Black Phosphorus Nanohybrids," *ACS Catal.*, vol. 6, no. 12, pp. 8009–8020, Dec. 2016.

[132] G. Tiouitchi *et al.*, "An easy route to synthesize high-quality black phosphorus from amorphous red phosphorus," *Mater. Lett.*, vol. 236, pp. 56–59, Feb. 2019.

[133] M. Zhao *et al.*, "Growth Mechanism and Enhanced Yield of Black Phosphorus Microribbons," *Cryst. Growth Des.*, vol. 16, no. 2, pp. 1096–1103, Feb. 2016.

[134] M. Zhao *et al.*, "Understanding the growth of black phosphorus crystals," *CrystEngComm*, vol. 18, no. 40, pp. 7737–7744, 2016.

[135] D. Wang *et al.*, "Revisiting the Growth of Black Phosphorus in Sn-I Assisted Reactions," *Front. Chem.*, vol. 7, Jan. 2019.

[136] H. B. Ribeiro, M. A. Pimenta, and C. J. S. de Matos, "Raman spectroscopy in black phosphorus," *Journal of Raman Spectroscopy*, vol. 49, no. 1. John Wiley and Sons Ltd, pp. 76–90, 01-Jan-2018.

[137] T. Schmid and P. Dariz, "Raman Microspectroscopic Imaging of Binder Remnants in Historical Mortars Reveals Processing Conditions," *Heritage*, vol. 2, no. 2, pp. 1662–1683, Jun. 2019.

[138] B. J. Inkson, "Scanning Electron Microscopy (SEM) and Transmission Electron Microscopy (TEM) for Materials Characterization," in *Materials Characterization Using Nondestructive Evaluation (NDE) Methods*, Elsevier Inc., 2016, pp. 17–43.

[139] R. Michalski, *Application of IC-MS and IC-ICP-MS in environmental research*. .

[140] M. Aceto, "The Use of ICP-MS in Food Traceability," in *Advances in Food Traceability Techniques and Technologies: Improving Quality Throughout the Food Chain*, Elsevier Inc., 2016, pp. 137–164.

[141] G. Zhang, Z. A. Lan, L. Lin, S. Lin, and X. Wang, "Overall water splitting by Pt/g-C3N4 photocatalysts without using sacrificial agents," *Chem. Sci.*, vol. 7, no. 5, pp. 3062–3066, 2016.

[142] J. Hu *et al.*, "Band Gap Engineering in a 2D Material for Solar-to-Chemical Energy Conversion.," *Nano Lett.*, vol. 16, no. 1, pp. 74–9, Jan. 2016.

Appendix A

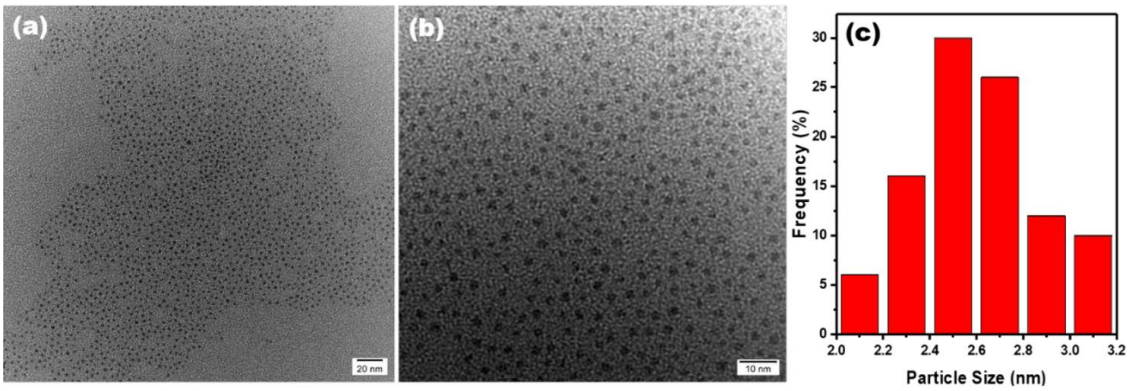

Figure A.1: TEM images at different magnifications and histogram of particle sizes of AgPd alloy nanoparticles (Ag_1Pd_1)

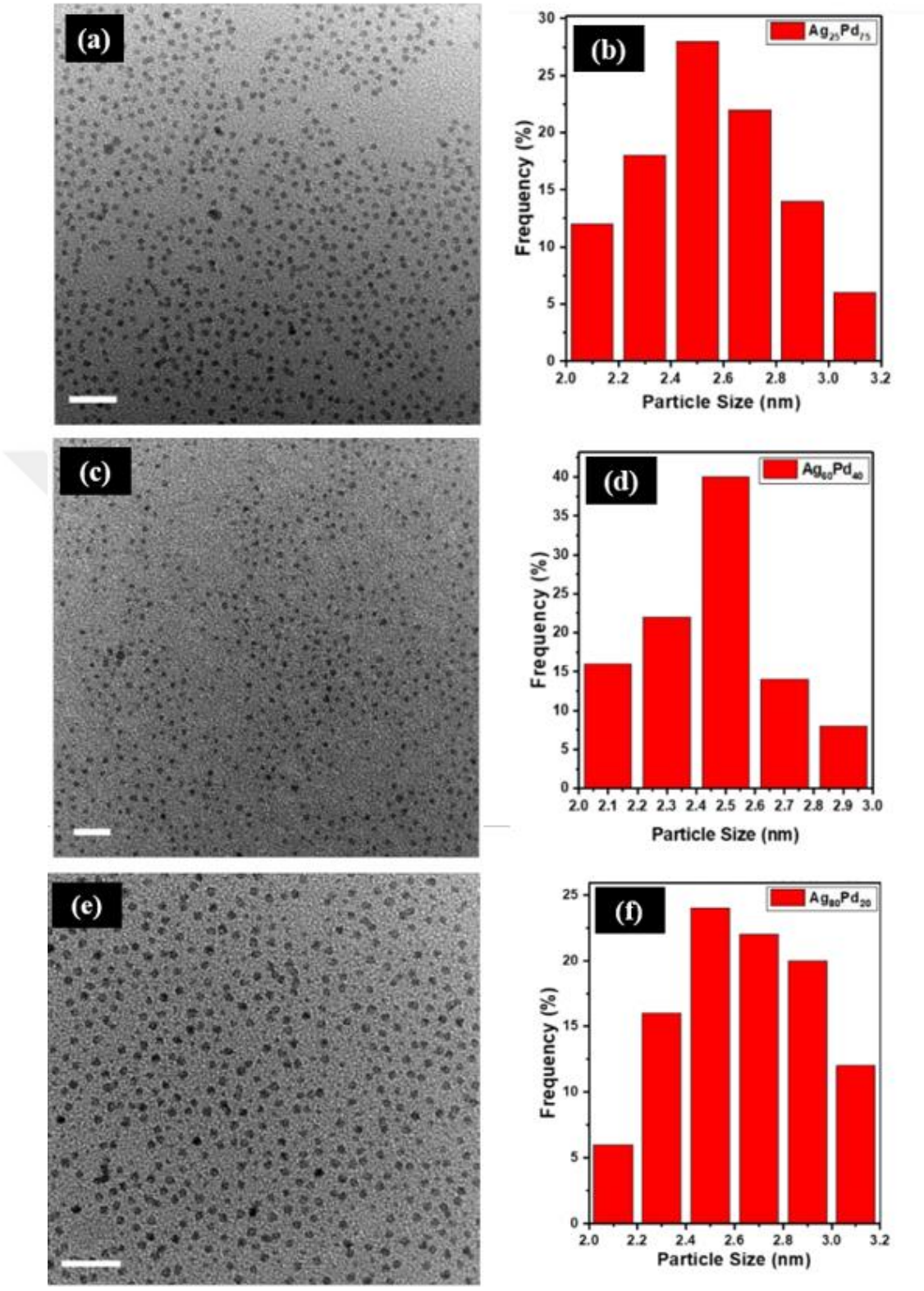

Figure A.2: TEM images and histograms of particle sizes of AgPd alloy nanoparticles (a) and (b) $Ag_{25}Pd_{75;}$ (c) and (d) $Ag_{60}Pd_{40}$; (e) and (f) $Ag_{80}Pd_{20}$ (scale bars represent 20 nm).

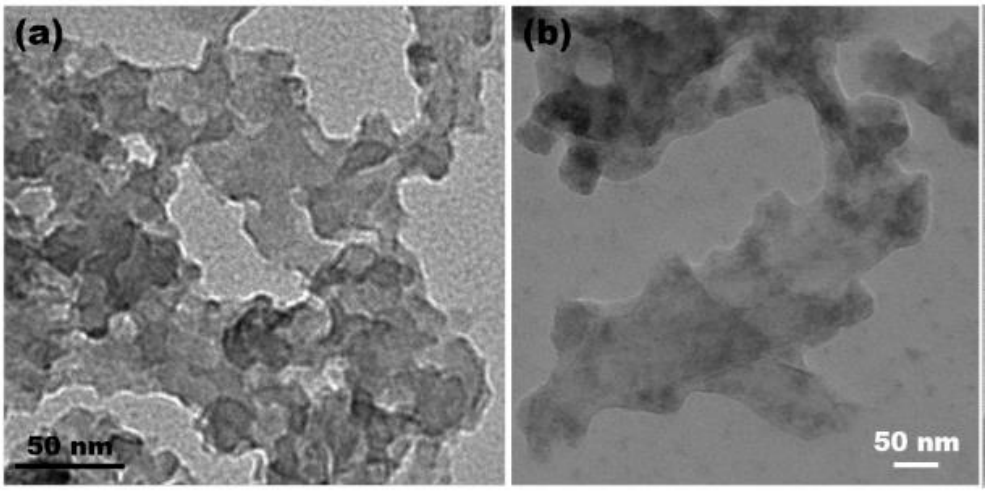

Figure A.3: TEM images of (a) bare mCN and (b) bare BP.

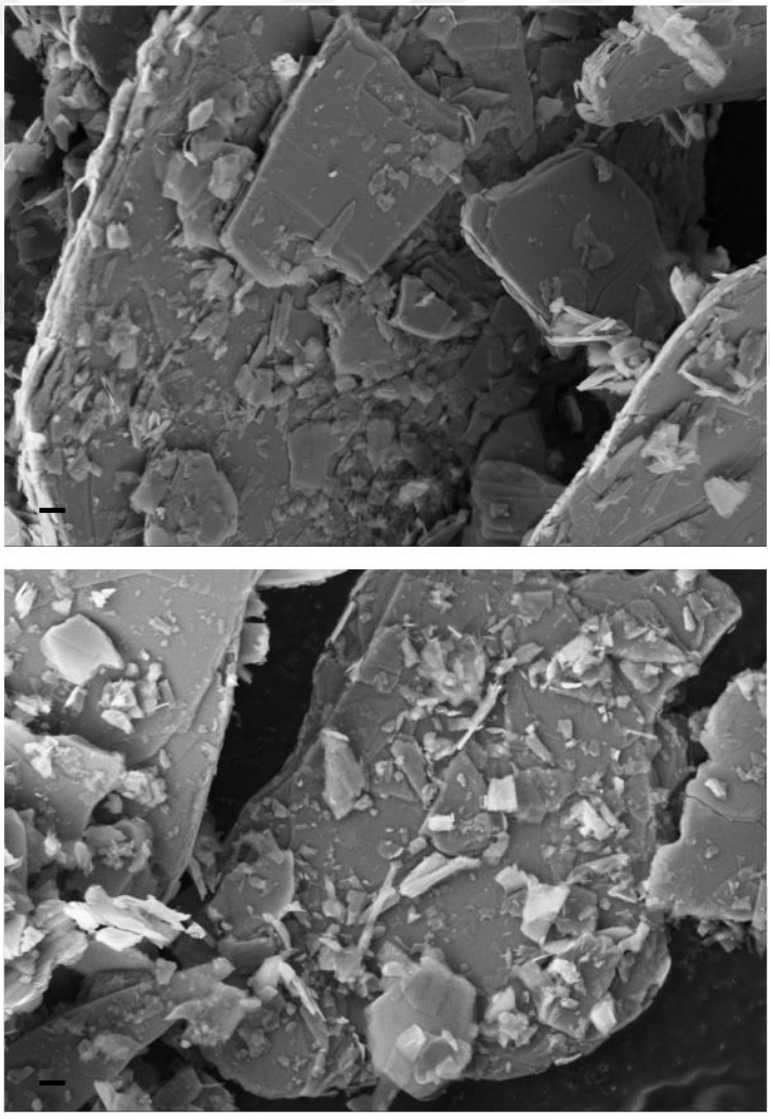

Figure A.4: SEM images of Bulk BP crystals, revealing 2D crystalline nature of the material (scale bars represent 1 μm).

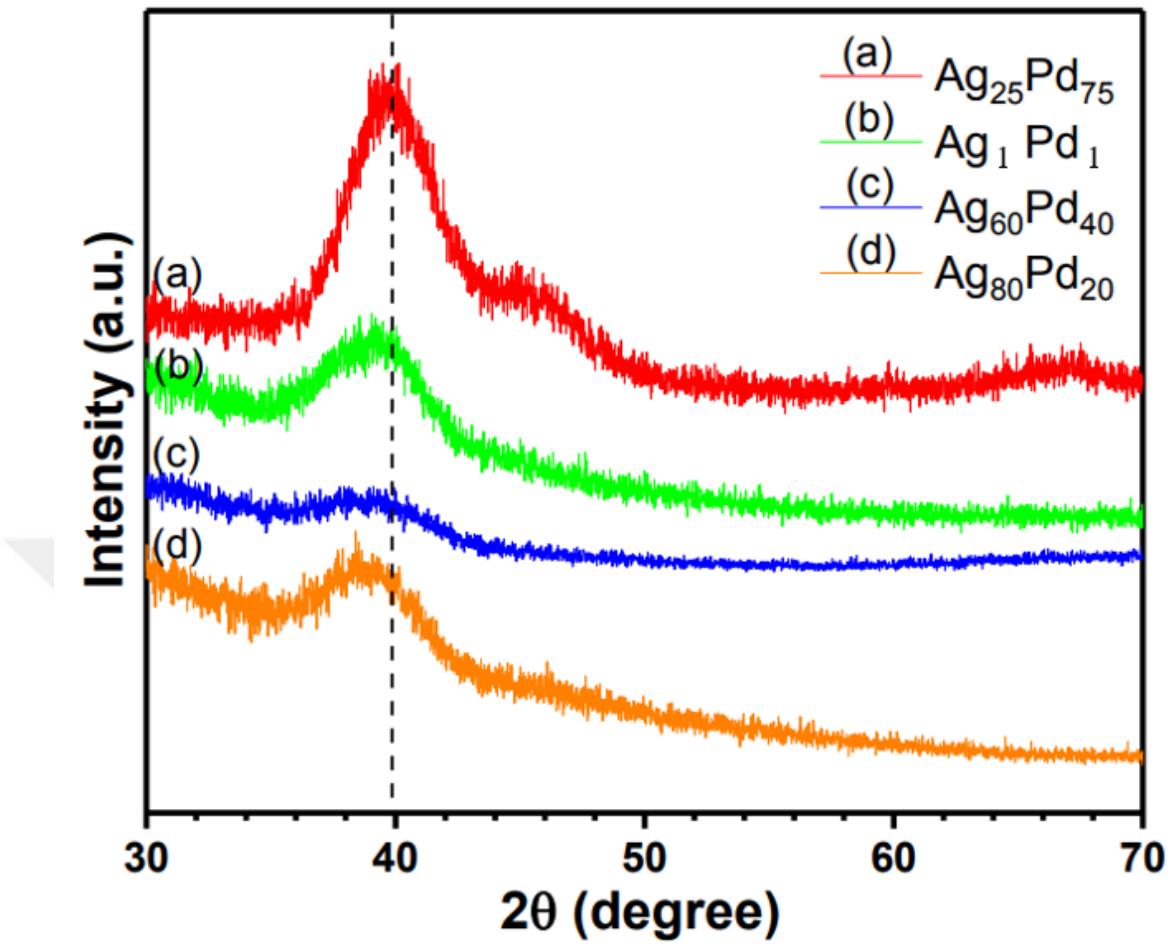

Figure A.5: XRD patterns of (a) $Ag_{25}Pd_{75}$ (b) Ag_1Pd_1 (c) $Ag_{60}Pd_{40}$ and (d) $Ag_{80}Pd_{20}$ alloy nanoparticles.

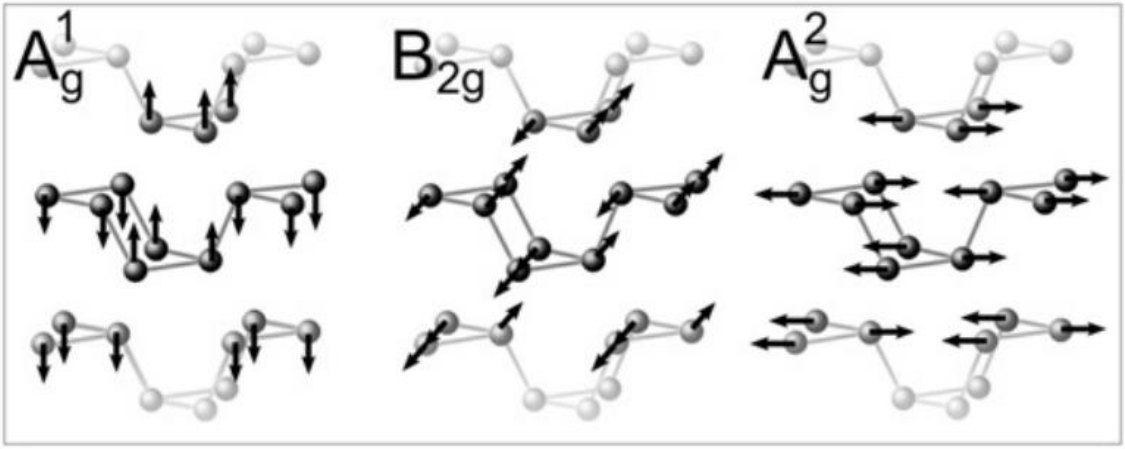

Figure A.6: Schematic representation of Raman-active modes of BP.

Table A.1: Lifetimes (τ_i) and Amplitudes (A_i) of the Lifetime Decays of bare mCN, bare BP, binary nanocomposite mCN/BP and ternary nanocomposite mCN/BP/AgPd/AT.

Sample	A_1	τ_1 (ns)	A_2	τ_2 (ns)
BP	28.3	1.28	71.7	6.67
mCN	40.2	2.5	59.8	10.2
mCN/BP	37.2	2.5	62.8	10.9
mCN/BP/AgPd/AT	25.4	1.9	74.6	9.6

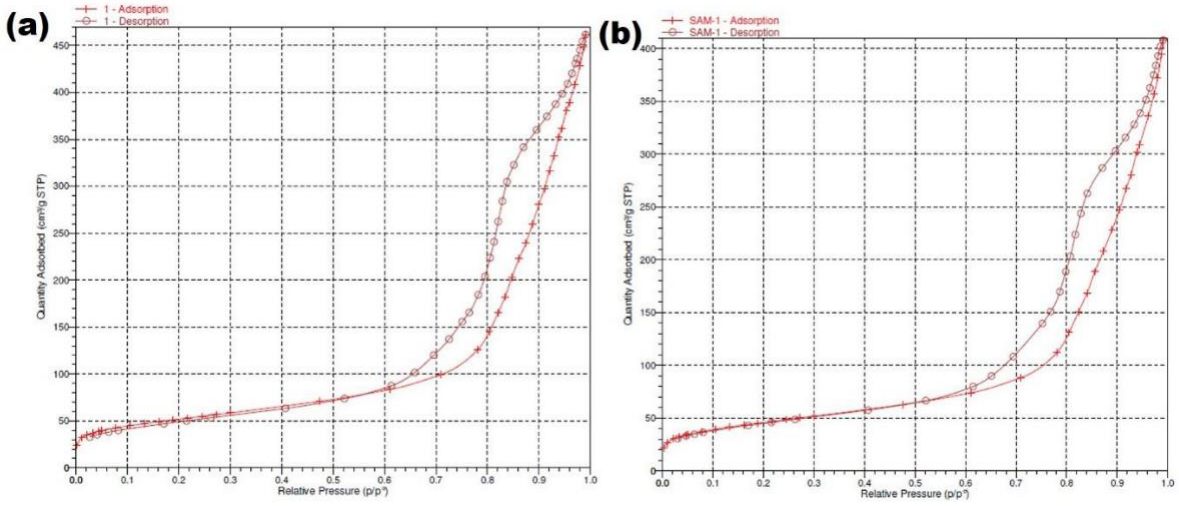

Figure A.7: N_2 adsorption/desorption isotherms of (a) pristine mCN and (b) mCN/BP binary composites.

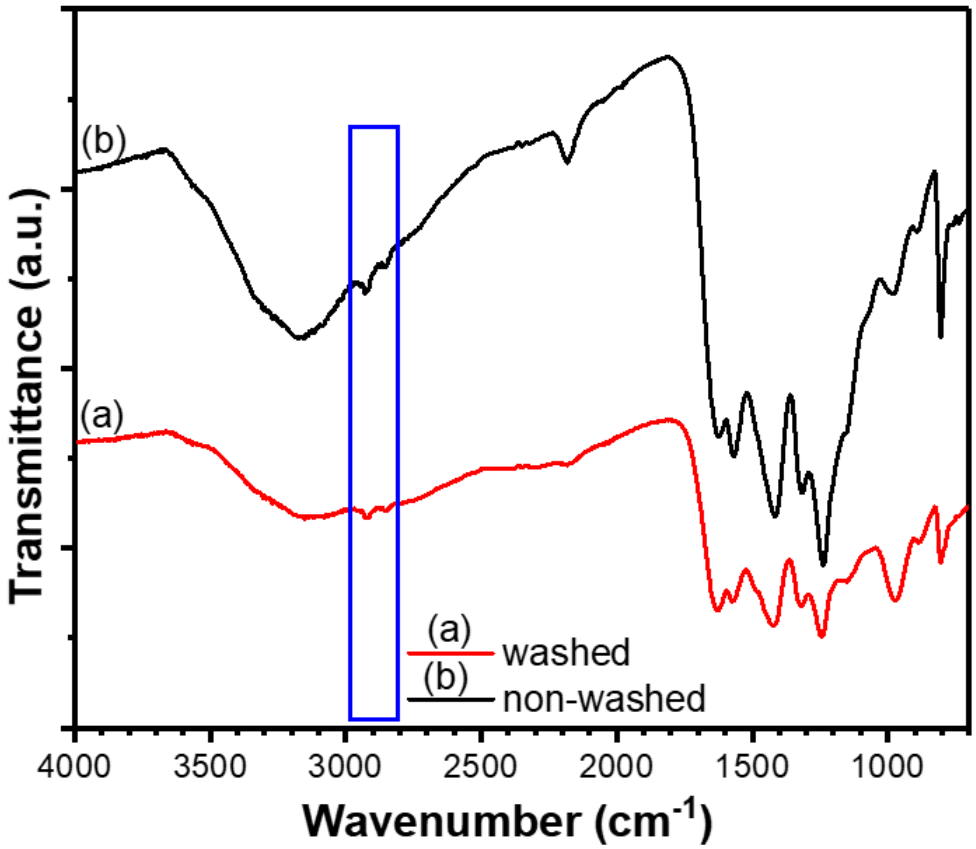

Figure A.8: FTIR spectra of mCN/BP/AgPd/AT (a) and mCN/BP/AgPd (b) ternary nanocomposites (acetic acid treated and non-treated, respectively).

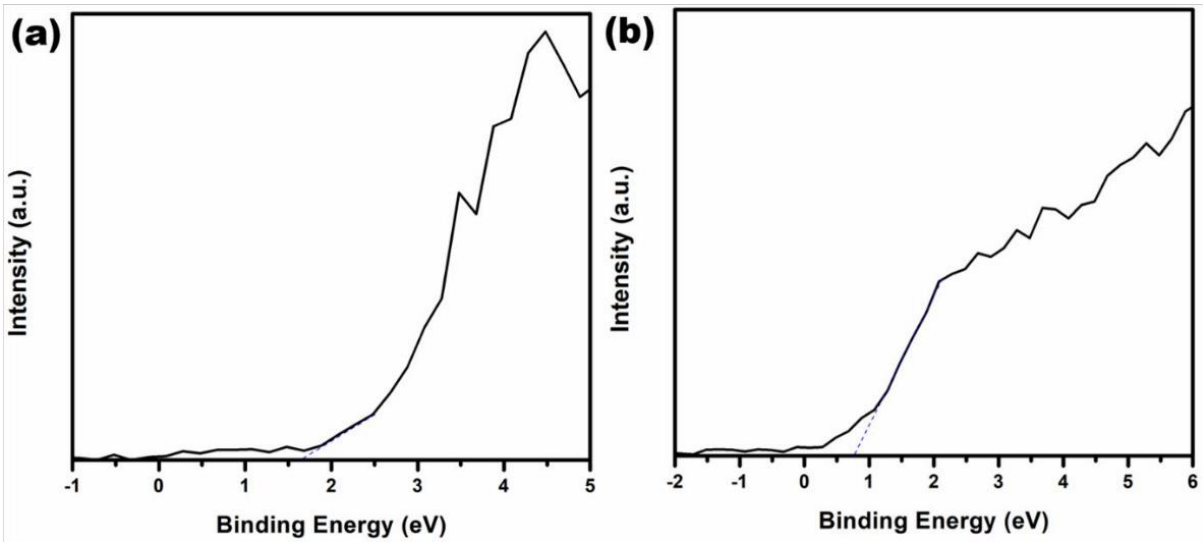

Figure A.9: XPS-VB spectrum of (a) bare mCN and (b) bare BP.

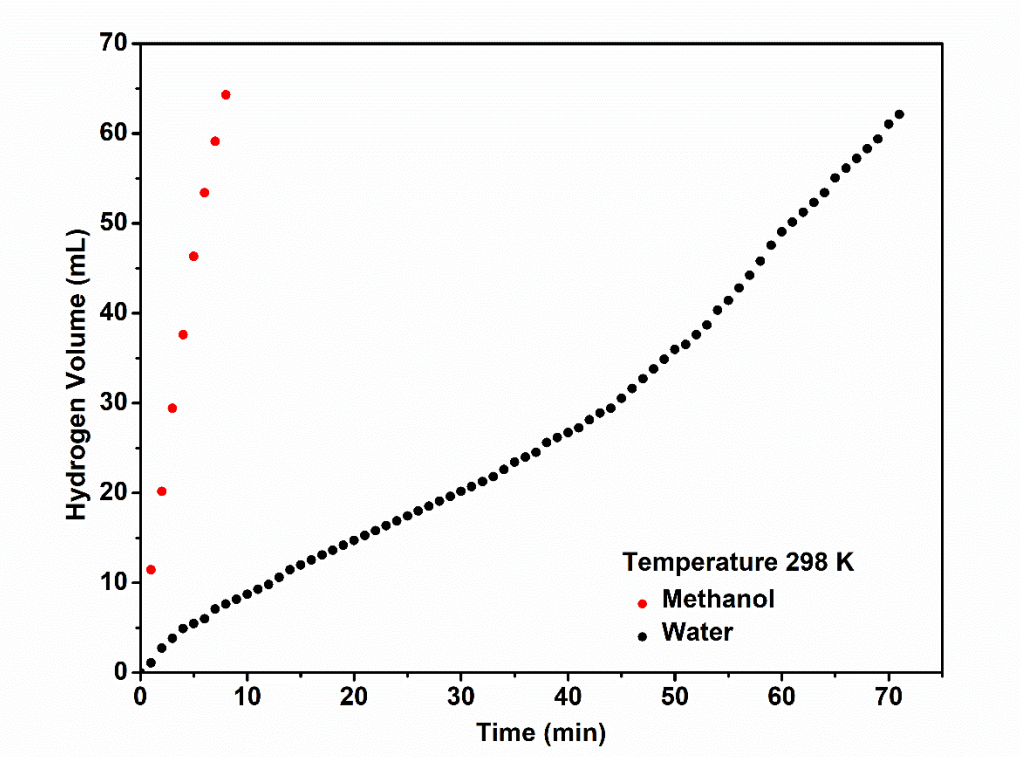

Figure A.10: Volume of hydrogen generation versus time during the mCN/BP/AgPd/AT catalysed methanolysis and hydrolysis of AB.